Thermal stability of retained austenite in Quenching & Partitioning steels

Master of Science Thesis

For the degree of Master of Science in Mechanical Engineering at Delft University of Technology

T.T.W. Koopmans

July 06, 2015

Faculty of Mechanical, Maritime and Materials Engineering (3mE) / Delft University of Technology

This page intentionally left blank

Table of contents

Glossary

List of symbols

A	Area (m^2)
V	Volume (m^3)
E	Modulus of elasticity (GPa)
ΔL	Length change (m)
L_0	Original length (m)
Tc	Curie Temperature
Bs	Bainite start temperature (°C)
Mf	Martensite finish temperature (°C)
Ms	Martensite start temperature (°C)
$A1$	Lower critical temperature for austenite (°C)
$A3$	Upper critical temperature for austenite (°C)
QT	Quenching temperature (°C)
PT	Partitioning temperature (°C)
t_p	Partitioning time (s)
Ms	Saturation Magnetization (A m^2 kg^{-1})
M	Magnetization (A m^2 kg^{-1})
G	Gibbs Free Energy (J mol^{-1})
ΔG	Gibbs Free Energy difference or Driving force (J mol^{-1})
f	Phase fraction

Greek symbols

α	Phase: ferrite
α’	Phase: martensite
γ	Phase: austenite
ε	Phase: epsilon carbide
η	Phase: eta carbide
θ	Phase: cementite
α	Thermal expansion coefficient (K^{-1})
Φ	Heating rate (°C min^{-1})

List of acronyms

Nital	Nitric acid in Alcohol
VSM	Vibrating Sample Magnetometer
XRD	X-Ray Diffraction
SEM	Scanning Electron Microscope
(L)OM	(Light) Optical Microscope
DSC	Differential Scanning Calorimeter
DTA	Differential Thermal Analysis
EBSD	Electron Backscatter Diffraction
EDS	Energy Dispersive X-ray Spectroscopy
M1	Martensite from the first quench
M2	Martensite from the second quench
RA	Retained Austenite
Q&P	Quenching & Partitioning
FCC	Face Centered Cubic
BCC	Body Centered Cubic
BCT	Body Centered Tetragonal
TTT	Time-Temperature-Transformation
CCT	Continuous Cooling Transformation
TRIP	Transformation Induced Plasticity

Acknowledgements

I would like to thank Maria Santofimia Navarro for being my daily supervisor. Thank you for all the interesting discussions we had, your patience and for showing me new points of view whenever I was stuck. I would like to express my gratitude to my professor Jilt Sietsma for always being available for interesting discussions and for sharing an impressive amount of knowledge on how to approach the study of steels. Nico Geerlofs played an integral part in making this thesis possible. Nico, thanks for all the help with the dilatometer and the discussions on how to do lab work in general.

I would also like to thank Lie Zhao and Ron van Tol for pointing me to the master materials science, and for getting me started.

In no particular order, I would also like to express my gratitude to Peter van Liempt, Kees Kwakernaak, Sander van Asperen, Richard Huizinga, Pina Mecozzi, Hans Brouwer and Farideh Haji Akbari for help with experiments and valuable discussions.

I would like to express my gratitude to Stefan van Bohemen for agreeing to be a committee member and valuable discussions, and Marcel Sluiter for agreeing to be a committee member as well.

Finishing my master thesis would have been impossible were it not for the Ph. D.'s and postdocs in the department. Thanks Ashwath, Ankit, Alfonso, Bij-Na, Constantinos, Javier and Zaloa for the good times.

Furthermore, I would like to thank Frans Bosman for the good training in the departmental gym, and Lourdes Gallastegui Pujana for valuable personal feedback.

Last but not least, I would like to thank my friends and family for just being there, and especially to Pieter and Julia for proofreading my thesis and just being good friends in general.

This page intentionally left blank

Chapter 1 Introduction

The drive for ever more safety and fuel efficiency in the automotive industry led the industry to search for steels with enhanced strength and ductility. Promising candidates to satisfy these demands are steels with a microstructure consisting of martensite and significant fractions of retained austenite. One class of steels with such a microstructure are Quenching & Partitioning (Q&P) steels.

The enhanced strength and ductility of Quenching & Partitioning steels is largely due to the presence of retained austenite. At elevated temperatures encountered during processes such as welding, hot dip galvanizing and paint baking, the possibility of retained austenite decomposition into thermodynamically more stable ferrite and carbides exists. Decomposition of retained austenite would have detrimental effects on the mechanical properties of Quenching & Partitioning steels. A requirement for practically applicable Quenching & Partitioning steels is therefore knowledge of the thermal stability of retained austenite against decomposition.

In this work, multiple microstructures have been created in one particular steel alloy using Quenching & Partitioning processing. These microstructures have been characterized using X-Ray Diffraction, Scanning Electron Microscopy, Optical Microscopy and Electron Backscatter Diffraction. Special attention was paid to the morphology and carbon content of retained austenite. The response of retained austenite to isothermal and isochronal annealing has been investigated using dilatometry and thermomagnetic methods.

The main finding of this work is that retained austenite in essence behaves as austenite which is higher in carbon content compared to the base alloy. Furthermore, the decomposition mechanisms of retained austenite have been successfully related to existing theory about austenite decomposition and mapped to a TTT-like diagram. Low-carbon retained austenite decomposes significantly quicker than high-carbon retained austenite.

A general background on Q&P steel and its microstructural components is presented in Chapter 2, followed by a literature review regarding the thermal stability of retained austenite in chemically comparable steels. Chapter 3 describes the methods, equipment and procedures used in this work. Chapter 4 presents results of the characterization of the created Q&P microstructures. In addition, the response of retained austenite to isothermal and isochronal annealing is discussed. Chapter 5 presents the conclusions of this work and Chapter 6 contains some recommendations for future work.

Chapter 2 Background

New global standards for vehicle safety and fuel-efficiency are becoming more demanding every year [1]. The automotive industry keeps searching for new low-cost steels, which should achieve significant increases in strength whilst offering a reduction in vehicle mass. Collectively, these steels are known as Advanced High-Strength Steels (AHSS).

These AHSS grades are defined by having both high strength and relatively high formability capabilities. Figure 2.1 shows the formability capabilities of different steels, expressed as elongation, plotted against the tensile strength. Conventional steels achieve relatively high ductility, but have low tensile strength, while AHSS grades generally have high tensile strength and lower ductility. The diagram shows that when strength is increased for conventional and AHSS grades, formability generally decreases.

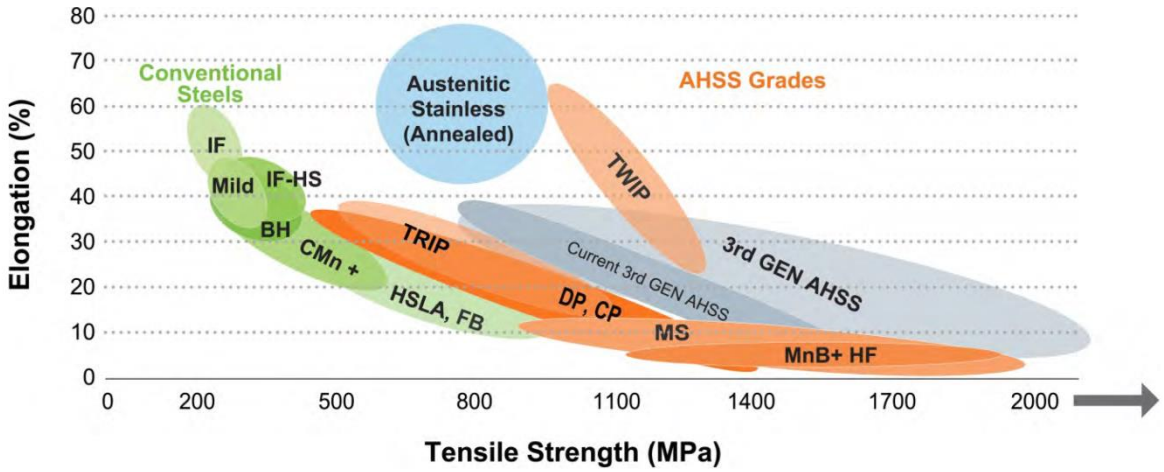

Figure 2.1: Formability diagram of different steels showing the general trade-off between elongation and strength. Reproduced from [1].

The 3rd generation of AHSS grades however, seeks to achieve both formability and high strength. As can be seen in the diagram, the current 3rd generation AHSS achieves ductility well above previous AHSS grades at the same strength level.

One class of steels from the current 3rd generation of AHSS grades are Quenching & Partitioning steels. These steels can achieve high both high formability and high strength levels due to their microstructure consisting of martensite and retained austenite. Martensite and retained austenite will be introduced in §2.1, followed by an introduction on Q&P steels in §2.2.

2.1 Key concepts in this thesis

2.1.1 Martensite

In steels, martensite is a Body Centered Cubic (BCC) / Body Centered Tetragonal (BCT) phase formed by a diffusionless shear transformation directly from Face Centered Cubic (FCC) austenite. This is schematically illustrated in Figure 2.2. The martensitic transformation will only happen if the material is cooled fast enough from the austenitic temperature region. The necessary cooling rate is called the critical cooling rate. Due to the high cooling rate, carbon interstitials in FCC have little time available to diffuse. Upon transformation from FCC to BCC the carbon atoms are essentially frozen into place.

Since there is less interstitial space available in BCC structure, the frozen carbon atoms stretch the lattice. This stretching effect results in a BCT structure.

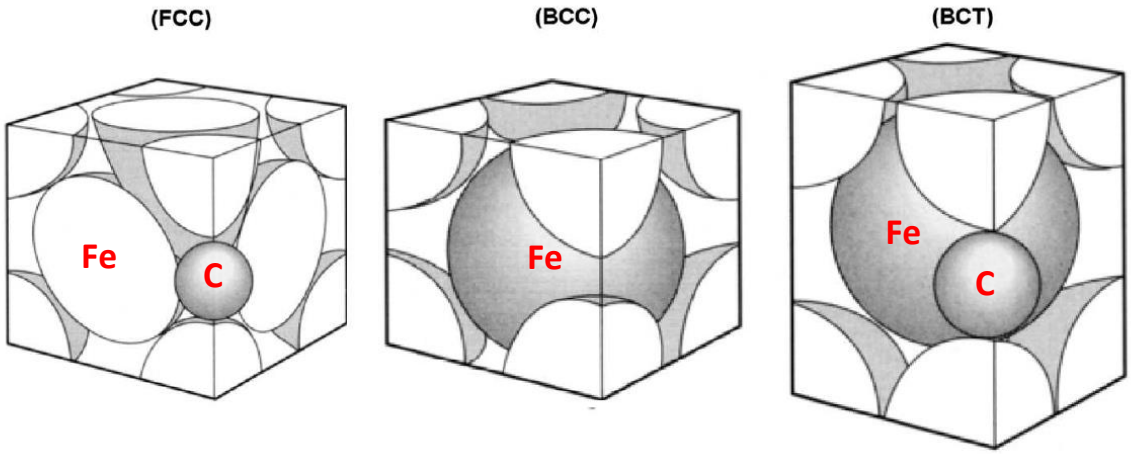

Figure 2.2: The FCC, BCC and BCT unit cells. Adapted from [2]. *Iron and carbon atoms are marked Fe and C respectively.*

The temperature at which the martensite starts to form upon quenching is called the Martensite start temperature, or Ms. This temperature is dependent on the chemical composition of the alloy.

The Koistinen-Marburger (K-M) equation [3] allows the estimation of the fraction martensite f_m during a quench to a given temperature T:

$$f_m = 1 - \exp[-\propto (T_{km} - T)] \qquad \textit{Equation 2.1}$$

where $\propto$ is a rate parameter and T_{km} the theoretical martensite start temperature.

In low carbon steels martensite has a lath morphology as shown in Figure 2.3a and Figure 2.3b. The martensite laths have orientation differences of angles of about 10 degrees [4]. The laths are confined within well parallel developed blocks, and packets contain a number of these blocks.

Martensite has excellent tensile strength and hardness, but is very brittle having low ductility and toughness. This is due to carbon supersaturation of the martensite, large strains resulting from the quench and the lath morphology of the martensite.

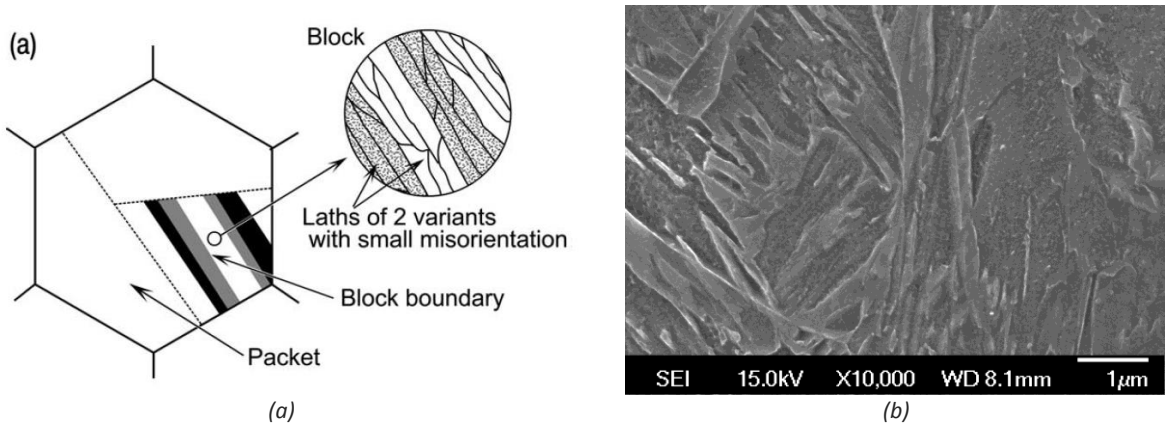

(a) *(b)*

Figure 2.3: (a) Morphology of martensite in low carbon steel. Adapted from [4] *(b) Martensitic microstructure as seen in the SEM.*

Tempering of martensite will improve the ductility and toughness of the material, at the expense of tensile strength and hardness. During tempering, the excess carbon from the BCT structure will form carbides, leaving a microstructure of ferrite and fine carbides. This microstructure is called tempered martensite.

2.1.2 Retained austenite

Austenite that does not transform to martensite during the quench to room temperature is called retained austenite. Retained austenite is metastable at room temperature. The stability of the retained austenite against the martensitic transformation depends on its grain size, local chemical composition of the retained austenite grain, its carbon content, dislocation density, its surrounding environment, etc. [5]. It is important to know that higher carbon content increases retained austenite stability.

In martensitic steels, retained austenite can enhance the ductility, toughness, fatigue life and strain hardening rate of the steel. Retained austenite will progressively transform to martensite with increasing strain, thereby enhancing the work hardening rate. This is called the Transformation Induced Plasticity (TRIP) effect.

Retained austenite can have two morphologies: blocky and film-like. The blocky type originates from geometrical partitioning of the original austenite grain [6]. The film-like type is retained between laths of martensite. In Q&P steels, film-like retained austenite is known to have lower carbon content compared to larger retained austenite grains [7], [8].

2.2 Background on Quenching & Partitioning steels

Quenching & Partitioning (Q&P) steels were first conceived by Speer *et al*. [9], [10]. The key concept in these steels is that carbon partitioning from martensite to austenite is possible if alloying elements are added that suppress carbide formation, such as silicon. The partitioning of carbon into austenite can stabilize the austenite against martensitic transformation, leaving retained austenite at room temperature. These steels are created via the Quenching & Partitioning process, as schematically illustrated in Figure 2.4.

The Q&P process starts with partial formation of martensite from a fully austenitized condition by quenching to a selected temperature (called Quenching Temperature, QT) between Ms and room temperature. This is followed by an annealing treatment at a higher temperature (called Partitioning Temperature, PT) in which the carbon from the supersaturated martensite can partition to the remaining austenite. This creates carbon-depleted tempered martensite and carbon-enriched austenite, promoting the stability of austenite against the martensitic transformation in a further quench. After giving sufficient time for carbon partitioning to occur, the material is quenched to room temperature. Austenite that was not sufficiently carbon-enriched transforms to martensite during this quench. The final microstructure consists of carbon-depleted tempered martensite from the first quench, fresh martensite from the second quench which has a (slightly) higher carbon content, and carbon-enriched retained austenite. In this work, the carbon-depleted tempered martensite will be called M1, the fresh martensite from the second quench will be called M2 and the carbon-enriched retained austenite will be called RA.

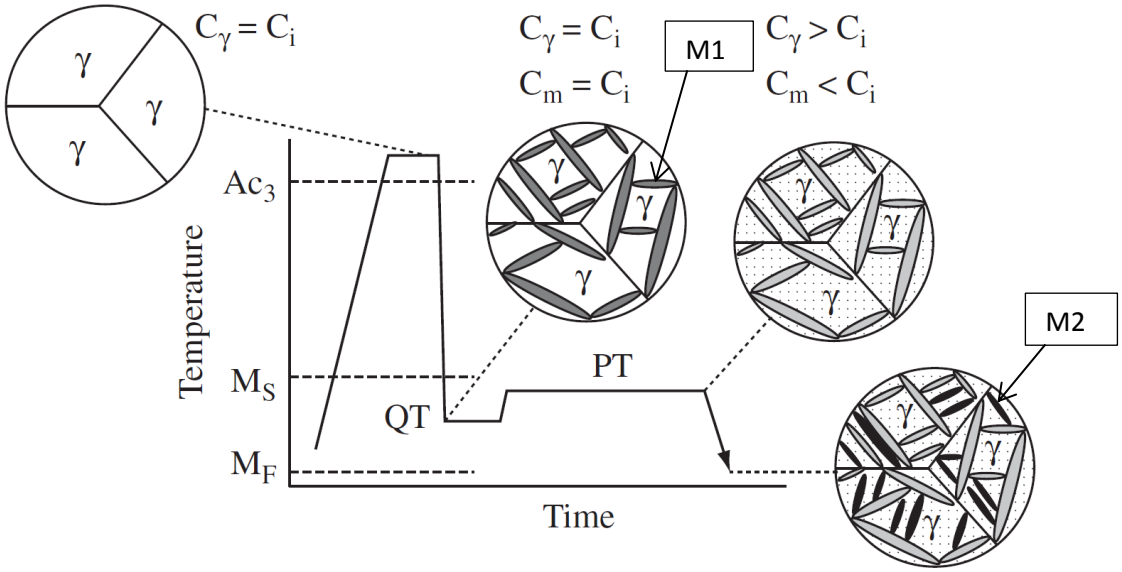

Figure 2.4: Schematic illustration of Q&P heat treatment, and the microstructure at each step of the treatment. QT and PT are the quenching temperature and partitioning temperature respectively, while C_i, C_γ and Cm represent the carbon concentrations in the initial alloy, austenite and martensite respectively. [9]

The microstructures resulting from the Q&P process are complex and vary depending on processing parameters. The composition of the alloy and the selection of the quenching temperature, partitioning temperature and partitioning time all have an effect on the resulting microstructure.

2.3 Thermal stability of retained austenite

At elevated temperatures, metastable retained austenite can decompose into thermodynamically more stable ferrite and carbides. These elevated are encountered during processes such as welding, paint baking or galvanizing. In Quenching & Partitioning steels, the decomposition of retained austenite would lead to a loss of its enhanced formability properties. It is therefore necessary to understand the factors influencing the thermal stability of retained austenite for usable Q&P steels.

In this work, the thermal stability of retained austenite is defined as: Resistance of the retained austenite against decomposition into more stable phases such as ferrite and cementite at elevated temperatures. In literature, a few studies have been found mentioning the decomposition of retained austenite in Q&P steel. None however, were devoted to it. These studies will be summarized, followed by an overview of literature which studied the decomposition of retained austenite in Transformation Induced Plasticity (TRIP) and Bainitic steels. TRIP and Bainitic steels contain significant fractions of retained austenite. They are useful for a general idea of the mechanisms that cause retained austenite decomposition.

2.3.1 Retained austenite decomposition in Q&P steels

In a conference paper by De Moor *et al.* [11], the effect of Si (0.24C-1.61Mn-1.45Si) and Al (0.18C-1.56Mn-1.73Al) additions on tempering in Q&P steels by means of dilatometry and Differential Scanning Calorimetry (DSC) was studied. These grades were reheated after Q&P processing to 600 °C with heating rates of 10 °C min^{-1}, 20 °C min^{-1} and 30 °C min^{-1}. Activation energies for retained austenite decomposition of 125 kJ mol^{-1} for the CMnAl grade and 202 kJ mol^{-1} for the CMnSi grade were measured. With a heating rate of 20 °C min^{-1}, retained austenite decomposition was thought to happen between 350 °C and 420 °C for the CMnAl grade.

Bigg *et al*. [12] have studied the dynamics of a Q&P steel (0.64C-4.57Mn-1.30Si) which has a Ms - Mf range spanning room temperature. The partitioning step at 500 °C was then studied by reheating in a powder diffractometer. The austenite lattice parameter reached a maximum at 480 °C, and starts declining thereafter. After the specimens reached 500 °C, the retained austenite fraction began to decline with increasing partitioning time. From these two observations it was concluded that carbide formation was occurring in order to consume the carbon released from decomposing austenite. Carbide precipitation was confirmed by the presence of carbide peaks at room temperature. Not mentioned was the type of carbide formed. Another observation was that silicon alloying additions delay, rather than prevent, equilibrium carbide formation at 500 °C.

Another paper by Bigg *et al*. [13] on the same alloy (0.64C-4.57Mn-1.30Si) shows no decomposition of retained austenite during a 90 minutes isothermal holding at a lower partitioning temperature of 300 °C. This was in contrast to other papers (not mentioned which ones), which measured a decrease in retained austenite fraction during partitioning. An increase in carbon content of the retained austenite during partitioning was measured.

A conference paper by Fawad [14] on a Q&P alloy (0.37C-0.85Mn-1.25Si-1.18Cr) investigated the tempering of this Q&P steel during reheating and isothermal holding. Blocky and film type retained austenite was detected, a total of 6 volume %. After 2 hour isothermal tempering at 250 °C, the blocky type retained austenite was not detected in SEM micrographs. The thin film type retained austenite was thermally more stable and transformed after 2 hours isothermal tempering at 300 °C. Still, 4% of retained austenite was observed with XRD after tempering. Observed was that "The stability of RA depends on its carbon content, size and location within the structure". The concentration of carbon in the retained austenite was determined to be about 1 wt. %. After isothermal tempering for 2 hours at 500 °C, no retained austenite was detected. Upon reheating to 600 °C with a heating rate of 10 °C min^{-1} in a dilatometer, decomposition of retained austenite was detected between 250 °C and 360 °C.

2.3.2 Retained austenite decomposition in TRIP steels

Jun *et al*. [15] studied the decomposition behavior of residual austenite in a TRIP (0.2C-1.51Mn-1.96Si) steel during a coiling simulation. After a hot rolling simulation, isothermal holding was performed using a salt bath. The isothermal holding temperatures were 350 °C, 400 °C and 450 °C, and the holding times were 5, 20, 60, 120 and 480 minutes. Furthermore, after 20 min holding at 400 °C and quenching to room temperature, a sample was reheated from RT to 500 °C in a diffractometer.

Table 2.1: Summary of phases transformed from retained austenite during isothermal holding [15].

Isothermal holding temperature	20 min	60 min	480 min
350 °C	Stable	Stable	Stable
400 °C	Stable	Cementite	Cementite
450 °C	Cementite	Cementite/pearlite	Cementite/pearlite

In-situ XRD heating revealed that retained austenite is thermally stable up to 350 °C. At temperatures higher than 370 °C the retained austenite can decompose into cementite, ferrite and pearlite. A

summary of phases formed from retained austenite during isothermal holding is given in [15], which is reproduced here as Table 2.1.

The different decomposition behavior of retained austenite at the different temperatures was thought to be correlated with the diffusivity of carbon. Because of low diffusion of carbon at 350 °C, the retained austenite was stable, while a much higher diffusion rate at 450°C made the austenite very unstable. At 400 °C, initial carbon enrichment of retained austenite occurred, but after 1 hour the retained austenite began to decompose into ferrite and cementite due to solute carbon redistribution.

In a paper by Shi *et al.* [16], decomposition of retained austenite in a TRIP steel (0.12C-1.5Mn-0.7Si) was investigated by means of differential scanning calorimetry (DSC). It was concluded that the thermal decomposition temperature of retained austenite occurs in the range of 300 °C to 550 °C, with an activation energy of 212 kJ mol^{-1}.

Amirthalingam *et al*. [17] studied the decomposition behavior of austenite in a TRIP alloy (0.19C-1.63Mn-0.35Si) by thermomagnetic methods. A welded fusion zone and the base metal were both examined. The samples were reheated in a VSM to 600 °C with a reheating rate of 0.03 °C s^{-1}. In the base metal, once the temperature reached 295 °C, formation of ε ($Fe_{2,4}C$) carbide from retained austenite occurred. Between 390 °C and 400 °C, possibly some η (Fe_2C) carbide formation occurred. Above 400 °C, formation of cementite occurred. The temperature range of retained austenite decomposition was 290 °C to 440 °C.

In the welded sample, a lower fraction of retained austenite was detected, but the carbon content in the retained austenite was higher. Precipitation of ε carbide was detected at 240 °C, and the temperature range of retained austenite decomposition was 240 °C to 460 °C. The decomposition kinetics of higher carbon retained austenite (welded sample) is therefore slower compared to the lower carbon retained austenite (base metal).

2.3.3 Retained austenite decomposition in Bainitic steels

Luzginova *et al*. [18] studied the thermal stability of retained austenite by thermomagnetic methods with a bainitic SAE 52100 steel (1.01C-1.36Cr-0.32Mn-0.25Si). Multiple samples with different bainitic holding times and temperatures, resulting in different volume fractions of retained austenite, were reheated to 800°C in a VSM with a heating rate of 5 °C min^{-1}. The temperature at which retained austenite started to decompose was between 180 °C and 240 °C. During reheating, formation of ε carbide during retained austenite decomposition around 280 °C was detected. The decomposition was finished at 300 °C.

Saha Podder *et al*. [19] investigated a (0.22C-3Mn-2.03Si) bainitic steel. After bainitic holding at 390 °C for 2 hours, the sample was cooled to room temperature. Tempering was carried out at 450 °C, and fresh martensite was detected after tempering. Tempering was found to destabilize the retained austenite due to local reduction in carbon concentration following the precipitation of minute quantities of cementite. This theory was proposed in 1956 by Cameron [20]. Only after one hour of tempering and further destabilization does ferrite formation occur from retained austenite. Tempering at 250 °C for 5 hours was found to have no significant effect on the retained austenite.

Saha Podder *et al*. [21] investigated a (0.39C-4.09Ni-2.05Si) bainitic steel. After bainitic holding at 380 °C for 2 hours, the sample was cooled to room temperature, and then tempered at 400 °C for varying duration. During the tempering in the synchrotron at the ESRF, diffraction spectra were collected. From these spectra the retained austenite fraction and carbon concentration were determined. It was observed that both blocky and film type retained austenite existed in the material. Film type retained austenite was observed to have higher carbon content, and also to decompose earlier. The reason for this was thought to be the greater driving force for cementite precipitation due to the higher carbon content.

2.3.4 Retained austenite decomposition in other steels

Special attention is called to a paper by Morra *et al*. [22], where the decomposition of retained austenite in multiple 1 wt. % C, low silicon alloys is studied. The temperature range in which retained austenite decomposed was 200 °C to 350 °C, with activation energies are in the range of 135-156 kJ mol^{-1}. This could suggest carbon diffusion in retained austenite as the rate controlling mechanism (≈140 kJ mol^{-1}), but alternatively, interface movement controlled growth (≈140 kJ mol^{-1}) for the γ → α transformation is suggested as the rate controlling mechanism.

Waterschoot *et al*. [23] studied the tempering kinetics of the martensitic phase in DP steel (0.72C-1.53Mn-0.11Si). Decomposition of retained austenite was found to occur in the temperature range 250 °C to 350 °C. The activation energy was found to be 154.7 kJ mol^{-1}. Furthermore, multiple carbides (Fe_2C, Fe_2C_5) were pointed out as capable of forming from retained austenite decomposition.

Primig *et al*. [24] studied the activation energy of decomposition of retained austenite in a DSC with quenched SAE1040 steel (0.67C-0.75Mn-0.22Si). This activation energy was determined to be 166-185 kJ mol^{-1}.

2.3.5 Discussion based on literature

Literature seems to focus on the decomposition of retained austenite in the temperature range between 200 and 400 °C. High (> 1 wt. %) Mn and/or high (> 1.5 wt. %) Si alloys show slow decomposition of retained austenite in this temperature range, especially after heat treatments which allow the enrichment of residual austenite with carbon such as TRIP or bainitic treatments. In literature it is established that silicon significantly slows the precipitation of cementite from austenite in this temperature range [25], indicating that Si and C play significant roles preventing the decomposition of retained austenite. At longer isothermal holding times in this temperature region in steels with high Si content, eventually carbide or cementite formation occurs [15], indicating that retained austenite is metastable at these temperatures.

Contradicting results in literature seem to suggest that both higher and lower carbon retained austenite decompose first. The decomposition mechanism of low-carbon retained austenite is not studied in the literature in this review. High carbon retained austenite in steels with Si forms cementite first, eventually followed by pearlite formation around 450 °C. This indicates that high carbon retained austenite is hypereutectoid austenite, which will decompose with cementite as the leading phase, followed by pearlite formation at temperatures above 400 °C.

The activation energy of decomposition is 120 kJ mol^{-1} to 220 kJ mol^{-1}, depending on composition. Typically, in literature the rate controlling event of retained austenite decomposition is attributed to be diffusion of carbon in austenite.

2.4 Approach

Literature offers a fragmented overview of retained austenite decomposition, and a complete approach seems to be missing with respect to studying retained austenite decomposition in all temperature regions between room temperature and below A1. Furthermore, no coherent theory of retained austenite decomposition was found in the studied literature. In Q&P steels, relatively little is known about retained austenite decomposition. This work therefore focuses on the following:

- Creation of Q&P microstructures and characterization of the created microstructures.
- Integral approach: study decomposition in a wide range of temperatures below A1.
- A study of the response of retained austenite to both isothermal and isochronal annealing
- If possible, formulation of a coherent theory of retained austenite decomposition.

A dilatometer will be used to create Q&P microstructures. To study the decomposition behavior of retained austenite during reheating, dilatometry and thermomagnetic methods will be used. However, in literature [24], [26], the decomposition of retained austenite between 250 and 350 °C and the transformation of transition carbides and clustered carbon into cementite often occurs simultaneously, complicating the study of retained austenite decomposition in a dilatometer. However, Q&P steels are ideal candidates for the study of retained austenite decomposition in a dilatometer, since a low fraction of carbon is available for clustering of carbon and formation of transition carbides.

Chapter 3 Methods, Equipment and Procedures

3.1 General overview

In this chapter, an overview of the experimental procedures is given. The alloy used is introduced, and selected theoretical properties of this alloy are calculated. An overview of the Quenching & Partitioning treatments used in this work and the post-processing of the resulting samples is presented. Furthermore, experimental details on the equipment used are given. Dilatometry, magnetic methods and Electron Backscatter Diffraction are extensively treated. The reader is assumed familiar with X-ray Diffraction, Scanning Electron Microscopy and Optical Microscropy, and these methods are not treated in extensive detail.

3.1.1 Materials

The material used was an alloy specially made for research in Q&P steel, and will be referred to as QP-G. The composition in weight percentage can be seen in Table 3.1. The steel was produced using a laboratory vacuum induction furnace. After casting, the steel was hot rolled to a final thickness of 4 mm and then air cooled. Cylindrical specimens of 3.5 mm in diameter and 10 mm length were then machined parallel to the rolling direction for dilatometry, comparable to the procedure in [27].

Table 3.1: Composition of QP-G (wt. %)

Steel	C	Mn	Si	Mo	Al	S	P	Fe
QP-G	0.20	3.51	1.525	0.509	0.03	0.0079	0.006	Balance

At Mn concentrations higher than 3 wt. %, the possibility of Mn segregation exists. QP-G is therefore susceptible to Mn segregation, and segregation was observed as microstructural banding in some specimens. A comparison can be made between regions where the Mn concentration is slightly higher than the base alloy, and regions where it is slightly lower than the base alloy. In regions where the Mn concentration is slightly higher, the A1 temperature will be slightly lower. The undercooling during quenching will therefore be smaller. Likewise, regions in which the Mn concentration is slightly lower will experience a higher undercooling. This difference in undercooling leads to a visibly different reaction to martensite formation during quenching or bainite formation during isothermal holding, and is seen as microstructural banding. Figure 3.1 shows typical microstructural banding encountered in specimens in this work.

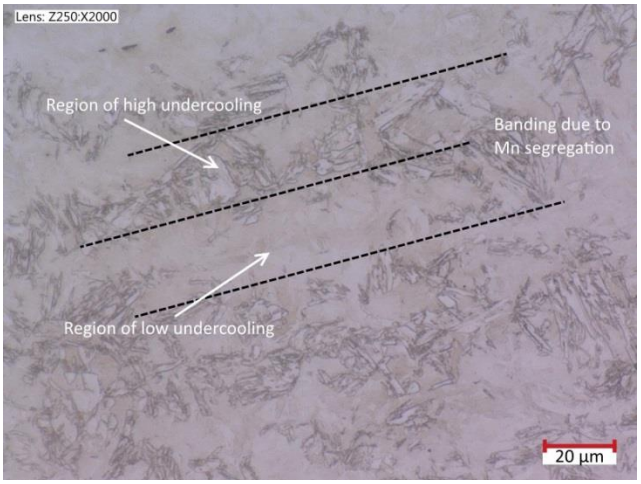

Figure 3.1: Optical Micrograph of a sample with visible microstructural banding.

The Martensite start and Bainite start temperatures of QP-G were determined using empirical equations by van Bohemen [28]. The determined Ms temperature was 325 °C, while the determined Bs temperature was 401 °C.

According to Kop [29], the Curie temperature is determined using Equation 3.1:

$$Tc = 1042\ K - x_{Mn} \times\ 1500K \qquad \textit{Equation 3.1}$$

where Tc is the Curie temperature and x_{Mn} is the atomic fraction of Mn in the material. For QP-G, this gives Tc = 989 K (716 °C). Another estimate is possible by interpolating data on the effect of Mn, Si and Mo by Arajs [30], which gives Tc = 993 K (720 °C). The experimentally determined Curie temperature was determined from dilatometry data as Tc = 988 ±3 K (715 ±3 °C).

3.1.2 Design of Quenching & Partitioning treatments

The Q&P treatments applied in this work consisted of full austenitization for 180s at 900 °C, followed by cooling with 50 °C s^{-1} to quench temperatures ranging from 340 °C to 140 °C. This was followed by isothermal holding for 3s at the quench temperature and heating with 10 °C s^{-1} to the partitioning temperature of 400 °C. An isothermal holding for 50 s at the partitioning temperature was followed by a quench to room temperature with 50 °C s^{-1}. All Q&P treatments were performed in a dilatometer (see § 3.2). The Q&P heat treatments are schematically shown in Figure 3.2a.

Selected samples were reheated directly following the Q&P treatments. The reheating treatments are schematically shown in Figure 3.2b, Figure 3.2c and Figure 3.2d. Details about which samples were reheated are found in the main text. A few samples were also directly quenched, and details about the quenching treatment are found in Figure 3.2e.

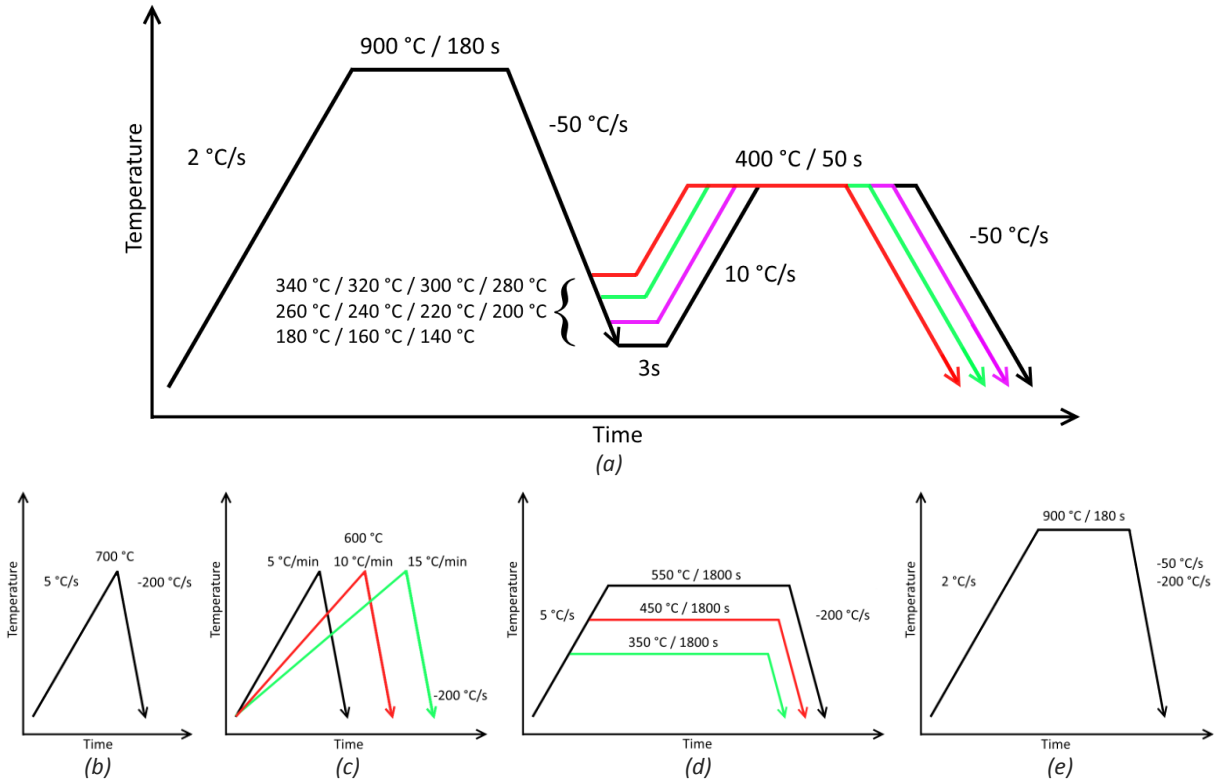

Figure 3.2: Schematic overview of the heat treatments applied in this work. (a) Q&P heat treatments. (b) (c) (d) Annealing treatments applied to selected specimens directly following the Q&P heat treatments. (e) Quenching heat treatments.

In this work, samples are referred to with a combination of 2 different identifiers:

1. Quenching temperature *xxx* (*e.g.* QT*xxx*)
2. If applicable, reheating temperature *yyy* and reheating rate *zz* (*e.g.* H*yyy_zz*Cmin)

Selected examples:

1. Quenched and partitioned sample with a quenching temperature of 260 °C : QT260
2. Quenched and partitioned sample with a quenching temperature of 320 °C, reheated to 600 °C with a heating rate of 10 °C min^{-1}: QT320H600_10Cmin

Some exceptions to this general rule exist in § 4.4, and will be clarified in the accompanying text.

3.1.3 Preparation of samples for microstructural investigation

After the Q&P treatment in the dilatometer, the specimens were cut using a Struers Minitom with a diamond grinding disc (Struers M1D10) into 3 parts as schematically shown in Figure 3.3. Due to water cooling during cutting, no retained austenite is assumed to have decomposed thermally during the cutting. The cut side of the 6mm long cylinder was used for X-Ray Diffraction, Optical Microscopy, Scanning Electron Microscopy and Electron Backscatter Diffraction after metallographic preparation, while the end disc was used for magnetic measurements.

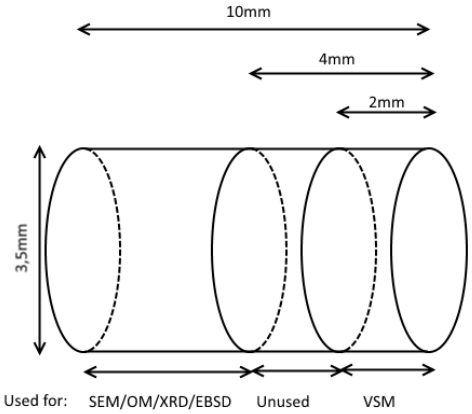

Figure 3.3: Schematic of cutting of sample and uses for the cut parts.

The metallographic preparation was conventional grinding using SiC papers up to 2000 grit, and polishing using 3 µ and 1 µ diamond suspension. The specimen was then etched with 2% nital for subsequent use in SEM and OM. The XRD measurements on the specimens were performed after grinding and polishing up to 3 µ diamond suspension. EBSD measurements on the specimens were performed after grinding and polishing with a finishing step of 0.020 µ alumina particles in a neutral solution, OP-AN (Struers).

3.2 Dilatometry

3.2.1 Equipment

A dilatometer is a device that measures length change of a specimen during the application of a heat treatment. In this work, a dilatometer is used to apply heat treatments to samples and record the resulting length changes due to thermal expansion or contraction and microstructural processes, such as the formation of martensite and austenite.

In Figure 3.4, a schematic representation of a push rod dilatometer is shown. The sample is clamped between two quartz push rods, and a Linear Variable Differential Transformer is used to record length changes in the sample and the push rods. A high-frequency induction coil is then used to heat the sample, and using small holes in the induction coil a cooling gas can be applied to evenly cool the sample. The thermocouple is used to record the temperature and for control of the temperature of the sample.

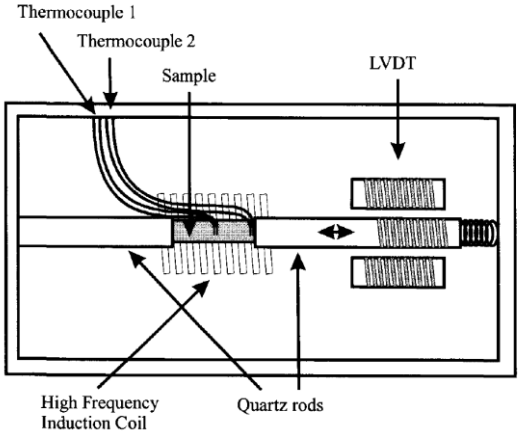

Figure 3.4: Schematic representation of a dilatometer [29].

The length change of the sample was measured in this work using a Bähr 805 DIL A/D dilatometer. The length resolution of this machine is 50 nm, and the temperature resolution is 0.05 °C. Heating rates of up to 4000 K s^{-1} and cooling speeds of 2500 K s^{-1} can be achieved.

Solid cylindrical samples with a length of 10 mm and a diameter of 3.5 mm were used, with a type S thermocouple spot-welded on the surface. A vacuum on the order of 10^{-4} mbar was used during heating or isothermal segments. Helium was used as the cooling gas. The original length of the sample L_0 was measured using a Mitutoyo digital caliper, model 500-181U, with a readout error of ±0.02 mm.

3.2.2 Processing of dilatometry data

In this work, the dilatometer was used to create microstructures and study phase transformations. Phase transformations are accompanied by a change in volume, but a dilatometer can only measure length change. The essential assumptions which relate volume change and length change and allow for the study of phase transformations with a dilatometer, are that the material behaves isotropically and that $|\frac{\Delta V}{V}| \ll 1$.

These assumptions give rise to the relationship between length change and volume change as given by Equation 3.2:

$$\frac{3\Delta l}{l} \cong \frac{\Delta V}{V}, \qquad \textit{Equation 3.2}$$

where $\frac{\Delta l}{l}$ is the length change of the sample, and $\frac{\Delta V}{V}$ the volume change of the sample.

3.2.3 Thermal expansion

To study phase transformations in a dilatometer, the thermal expansion behavior of the material needs to be modeled. The thermal expansion behavior of QP-G was found to best match the non-linear methods as proposed by Van Bohemen [31]. The calculated thermal expansion of austenite, ferrite and cementite are plotted in Figure 3.5a, while the calculated coefficients of thermal expansion of austenite, ferrite and cementite are plotted in Figure 3.5b.

The non-linear lattice expansion of austenite was described by

$$\frac{\Delta L^{\gamma}}{L_0^{\gamma}} = B_{\gamma}T + B_{\gamma}\Theta_D^{\gamma}\left[\exp\left(-\frac{T}{\Theta_D^{\gamma}}\right) - 1\right] \qquad \textit{Equation 3.3}$$

where $\frac{\Delta L^{\gamma}}{L_0^{\gamma}}$ is the relative length change of an austenite lattice, B_{γ} is the thermal expansion coefficient of austenite, T the temperature and Θ_D^{γ} the Debye temperature of austenite. The thermal expansion coefficient of austenite is calculated by deriving Equation 3.3 as

$$\alpha_{\gamma} = \frac{d}{dT}\left(\frac{\Delta L^{\gamma}}{L_0^{\gamma}}\right) = B_{\gamma}\left[1 + \exp\left(-\frac{T}{\Theta_D^{\gamma}}\right)\right] \qquad \textit{Equation 3.4}$$

Similarly, the non-linear lattice expansion of ferrite was described as

$$\frac{\Delta L^{\alpha}}{L_0^{\gamma}} = \frac{L_0^{\alpha} - L_0^{\gamma}}{L_0^{\gamma}} + B_{\alpha}T + B_{\alpha}\Theta_D^{\alpha}\left[\exp\left(-\frac{T}{\Theta_D^{\alpha}}\right) - 1\right] \qquad \textit{Equation 3.5}$$

where $\frac{\Delta L^{\alpha}}{L_0^{\gamma}}$ is the relative length change of a ferrite lattice, $\frac{L_0^{\alpha} - L_0^{\gamma}}{L_0^{\gamma}}$ is the relative length change between the BCC and FCC lattices at 0 K, B_{α} is the thermal expansion coefficient of ferrite, and Θ_D^{α} the Debye temperature of ferrite. The thermal expansion coefficient of ferrite is derived as

$$\alpha_{\alpha} = \frac{d}{dT}\left(\frac{\Delta L^{\alpha}}{L_0^{\gamma}}\right) = B_{\alpha}\left[1 + \exp\left(-\frac{T}{\Theta_D^{\alpha}}\right)\right] \qquad \textit{Equation 3.6}$$

The thermal expansion behavior of martensite does not differ significantly from ferrite [32], so the thermal expansion behavior of ferrite has been assumed for martensite.

The values are taken as B_{γ}= 24.8 x 10^{-6} K^{-1} and Θ_D^{γ}= 280 K, B_{α}=18.3 x 10^{-6} K^{-1}, Θ_D^{α}= 320 K and $\frac{L_0^{\alpha} - L_0^{\gamma}}{L_0^{\gamma}}$= 103.9 x 10^{-4}, all as determined in [31].

Analogous to the thermal expansion behavior of ferrite and austenite, the thermal expansion behavior of cementite has been modeled as described in [32] with

$$\frac{\Delta L^{Fe_3C}}{L^{Fe_3C}} = B_{Fe_3C}T + B_{Fe_3C}\Theta_D^{Fe_3C}\left[\exp\left(-\frac{T}{\Theta_D^{Fe_3C}}\right) - 1\right] + \delta\left[1 + \left(\frac{T - T_c}{T_w}\right)^2\right]^{-1} \qquad \textit{Equation 3.7}$$

where $\frac{\Delta L^{Fe_3C}}{L^{Fe_3C}}$ is the relative length change of a cementite lattice, B_{Fe_3C} the thermal expansion coefficient of cementite, and $\Theta_D^{Fe_3C}$ the Debye temperature of cementite. $\delta\left[1 + \left(\frac{T - T_c}{T_w}\right)^2\right]^{-1}$ is a

correction factor to account for the magnetic transition of cementite around the Curie temperature T_c, which has a significant effect on the thermal expansion coefficient of cementite. The thermal expansion coefficient of cementite is derived as

$$\alpha_{Fe_3C} = \frac{d}{dT}\left(\frac{\Delta L^{Fe_3C}}{L^{Fe_3C}}\right) = B_{Fe_3C}\left[1 + \exp\left(-\frac{T}{\Theta_D^{Fe_3C}}\right)\right] - \frac{2\delta(T - T_c)}{\left[\frac{(T-T_c)^2}{T_w^2} + 1\right]^2 * T_w^2} \qquad \textit{Equation 3.8}$$

The values are taken as B_{Fe_3C} =17.2 x 10^{-6} K^{-1}, $\Theta_D^{Fe_3C}$ = 440 K, δ = -15*10^{-4}, T_c = 512 K and T_w= 110 K, after a careful analysis of the data in [32] and a discussion with the author.

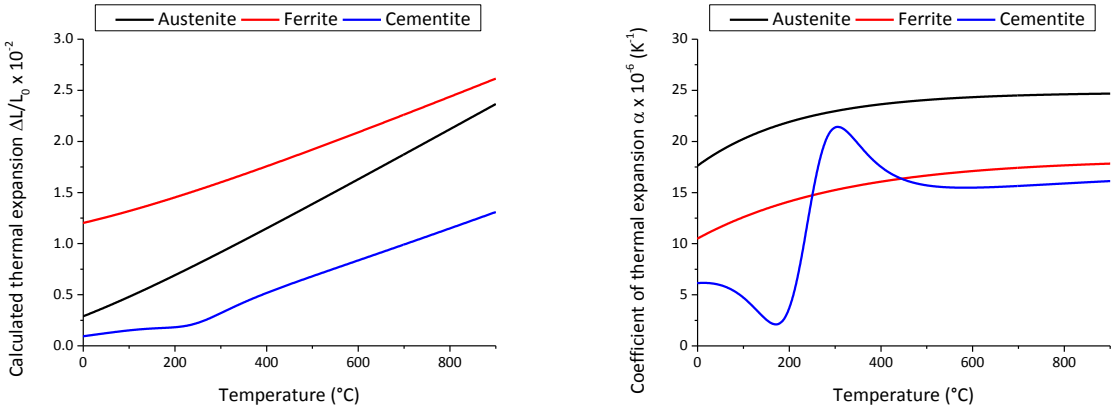

(a) *(b)*

Figure 3.5: (a) Relative length changes due to thermal expansion as used in this work. (b) Coefficients of thermal expansion as used in this work.

3.2.4 Quantification of phase fractions during quenching

3.2.4.1 Lever rule

For the determination of phase fractions, the lever rule can be used. The process is demonstrated using a martensitic transformation in QP-G steel, which is shown in Figure 3.6. Let phase A be FCC, and phase be BCC. Let x be $= \left|\left(\frac{\Delta L}{L_0}\right)_B - \left(\frac{\Delta L}{L_0}\right)_{exp}\right|$, with $\left(\frac{\Delta L}{L_0}\right)_B$ the theoretical length change of Phase B (BCC) at temperature T and $\left(\frac{\Delta L}{L_0}\right)_{exp}$ the experimentally measured length change of phase A + B. Let y be $= \left|\left(\frac{\Delta L}{L_0}\right)_A - \left(\frac{\Delta L}{L_0}\right)_{exp}\right|$, with $\left(\frac{\Delta L}{L_0}\right)_A$ the theoretical length change of Phase A (FCC) at temperature T. The fraction of Phase B (ferrite) at temperature T is then $\frac{y}{x+y}$, while the fraction of Phase A (austenite) at temperature T is then $\frac{x}{x+y}$. During isothermal transformations the lever rule can also be applied.

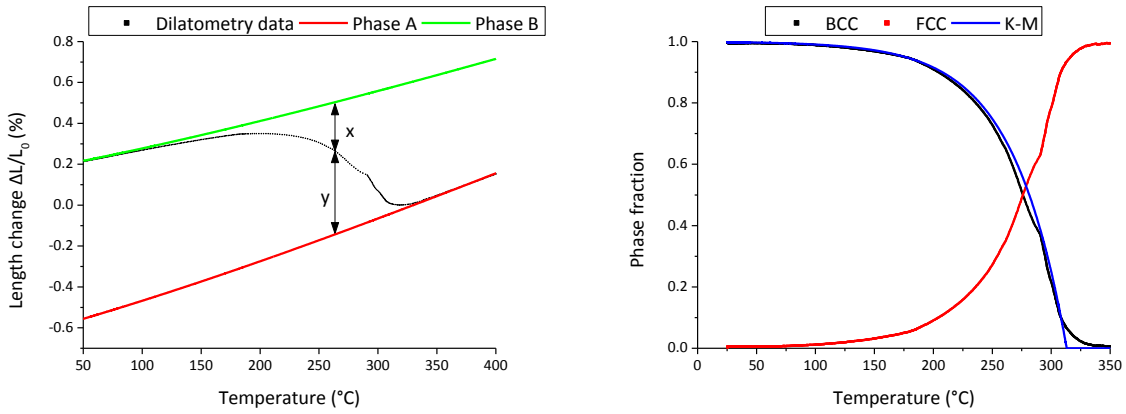

(a) *(b)*

Figure 3.6: (a) Schematic illustration of lever rule. (b) The phase fractions as calculated by the lever rule of Phase A (FCC) and Phase B (BCC). The fraction of phase B (BCC) is fitted with the Koistinen-Marburger Equation.

3.2.4.2 Koistinen-Marburger equation

The Koistinen-Marburger equation (Equation 2.1) was fitted to data generated during quenching with 50 °C s^{-1} to room temperature after the same austenization treatment used for Q&P samples, using the lever rule and the equations and methods proposed by van Bohemen [28], [31] and given in §3.2.3. The experimentally found fit parameters were T_{km} = 313 °C and α = 0.0218 K^{-1}, differing less than 5% and showing good agreement compared to the empirical equations proposed in [28], which give Ms = 325 °C and α = 0.0211 K^{-1}. When using the definition that Ms is the temperature where 1% of martensite has been formed, the experimentally found Ms was 331±3°C. As described by van Bohemen [28], the discrepancy between the experimentally found Ms and T_{km} found for the fit of the K-M equation can be explained by an initial gradual transformation during the start of martensite transformation. A better fit to the experimental data is found using the theoretical martensite start temperature T_{km}. Typically T_{km} is 5-20 C °C lower than Ms [28].

3.2.5 Detecting phase transformations

Using methodology adapted from [26], the volume effects of the decomposition of austenite and the precipitation of carbides from martensite can be determined. Apart from length change due to thermal expansion, a relative increase in length of the sample can be correlated to the decomposition of retained austenite, $\gamma \rightarrow \alpha + \theta$. A relative contraction in length, again apart from length change due to thermal expansion, can be correlated to the precipitation of carbides from martensite, $\alpha' \rightarrow \alpha + \theta$. The relative volume change $\frac{\Delta V}{V}$ of the precipitation of carbides from martensite $\alpha' \rightarrow \alpha + \theta$ can be predicted using

$$\frac{\Delta V}{V} = \frac{\frac{100-4X}{2}\,\nu_\alpha + \frac{3X}{12}\,\nu_\theta - \frac{100-X}{2}\,\nu_{\alpha'}}{\frac{100-X}{2}\,\nu_{\alpha'}} \qquad \textit{Equation 3.9}$$

where X is the atomic percentage of carbon in the original phase, ν_α the volume of the unit cell for ferrite, ν_θ the volume of the unit cell for cementite and $\nu_{\alpha'}$ the volume of the unit cell for martensite. The relative volume change $\frac{\Delta V}{V}$ of the decomposition of retained austenite $\gamma \rightarrow \alpha + \theta$ can be predicted using

$$\frac{\Delta V}{V} = \frac{\frac{100-4X}{2}\,\nu_\alpha + \frac{3X}{12}\,\nu_\theta - \frac{100-X}{4}\,\nu_\gamma}{\frac{100-X}{4}\,\nu_\gamma} \qquad \textit{Equation 3.10}$$

where ν_γ is the volume of the unit cell for austenite The respective volumes of the unit cells have been calculated using the data in Table 3.2. The length change can then be calculated by applying Equation 3.2.

Table 3.2: Crystallographic data as used in this work. Reproduced from [26]

Phase	Structure	Lattice Parameters (Å)	Number of Fe Atoms per Unit-Cell	Volume per Fe Atom (Å^3)
Martensite	BCT	a = 2.8664 – 0.013 wt. % C c = 2.8664 + 0.116 wt. % C	2	12.188 (1.1 wt. % C)
Ferrite	BCC	a = 2.8664	2	11.78
Austenite	FCC	a = 3.555 + 0.044 wt. % C	4	11.697 (1.1 wt. % C)
ε-carbide	Hex.	a = 2.752 c = 4.353	2	14.275
ε-carbide	Hex.	a = 2.753 c = 4.335	2	14.041
η-carbide	Ortho-rhombic	a = 4.704; b = 4.318 c = 2.830	4	14.371
Cementite (θ)	Ortho-rhombic	a = 4.5234; b = 5.0883 c = 6.7426	12	12.933

Since the volume of the unit cell and lattice parameters given in Table 3.2 are valid at room temperature, the volume of the unit cells has to be corrected to account for thermal expansion effects at higher temperatures. This has been done using

$$V_u(T) = \mathrm{V}_0[1 + \epsilon(T)]^3 \qquad \textit{Equation 3.11}$$

where $V_u(T)$ is the volume of a unit cell at temperature T, V_0 the volume of the unit cell at room temperature and $\epsilon(T)$ the strain for the unit cell calculated at temperature T using the non-linear thermal expansion coefficients as described in § 3.2.3. The corrected volumes of the unit cells are then used in Equation 3.9 and Equation 3.10.

In Figure 3.7a, the calculated relative length change of decomposition of a 1 wt. % C austenite into ferrite and cementite has been plotted at different temperatures, while in Figure 3.7b the calculated relative length change of austenite decomposition into ferrite and cementite has been plotted at room temperatures for varying carbon content in the austenite. This carbon concentration of the retained austenite was selected based on experimentally observed carbon concentrations in retained austenite after Q&P treatments in this work.

Figure 3.8a shows the calculated relative length change of a 0.06 wt. % C martensite precipitating carbides at different temperatures, while in Figure 3.8b the calculated relative length change of precipitation of carbides from martensite has been plotted at room temperature for varying carbon content in the martensite. This carbon concentration of the martensite was selected as the mass balance of carbon in a sample with the highest observed retained austenite fraction of 0.15 in this work. The determined carbon content in retained austenite is 1 wt. % C, and a mass balance of carbon gives a carbon content of 0.06 % wt. C in the martensite.

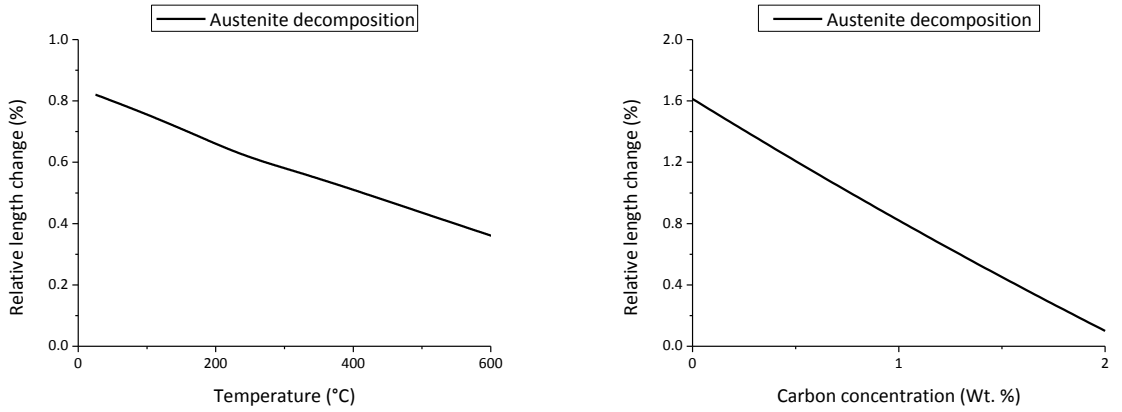

(a) *(b)*

Figure 3.7: (a) Length change of the decomposition of austenite with 1 wt. % C at different temperatures. (b) Length change of the decomposition of austenite with different carbon content at room temperature.

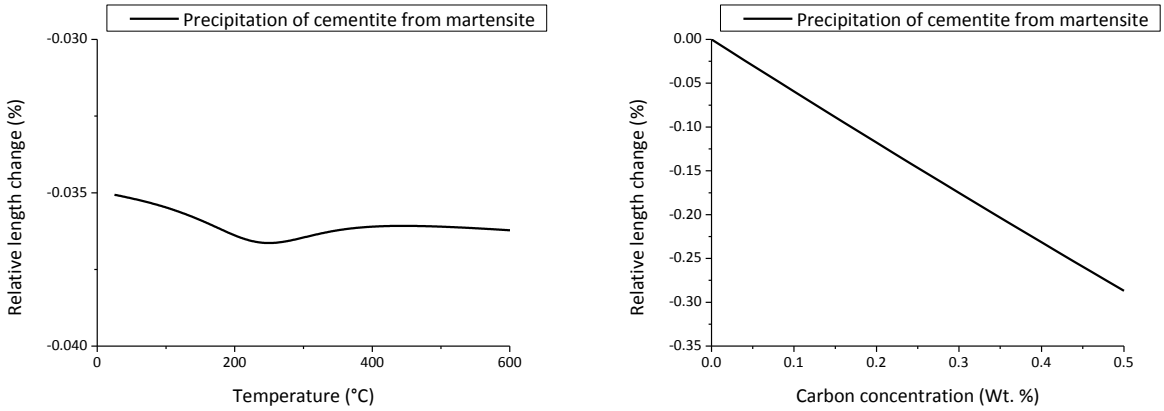

(a) *(b)*

Figure 3.8: (a) Length change of precipitation of carbides from martensite with 0.06 wt. % C at different temperatures. (b) Length change of precipitation of carbides from martensite with different carbon content at room temperature.

Having calculated the estimated effects of decomposition of retained austenite and precipitation of carbides from martensite in a dilatometer, a description of the quantification of these effects is given.

In earlier literature [26] these quantifications have been performed by an analysis of the length change $\frac{\Delta L}{L_0}$. However, an analysis of the derivative $\frac{d}{dT}\left(\frac{\Delta L}{L_0}\right)$ of the length change allows a clearer illustration of the processes occurring. To illustrate this, compare Figure 3.9a, where the length change $\frac{\Delta L}{L_0}$ of a sample during a reheating with 5 °C min^{-1} is plotted, to Figure 3.9b where the corresponding derivative $\frac{d}{dT}\left(\frac{\Delta L}{L_0}\right)$ is plotted. Any length changes, whether due to relative expansion or relative contraction, other than thermal expansion are clearly more readily identified and "magnified" to the human eye in Figure 3.9b. To quantify the decomposition of retained austenite and the precipitation of carbides from martensite, in this thesis an analysis of $\frac{d}{dT}\left(\frac{\Delta L}{L_0}\right)$ will therefore be used. This derivative is comparable to the thermal expansion coefficient of the sample.

In this work, the derivative was numerically derived from a 20 data point simple moving average of both length change and temperature. The number of data points recorded during the reheating was 2 K^{-1}.

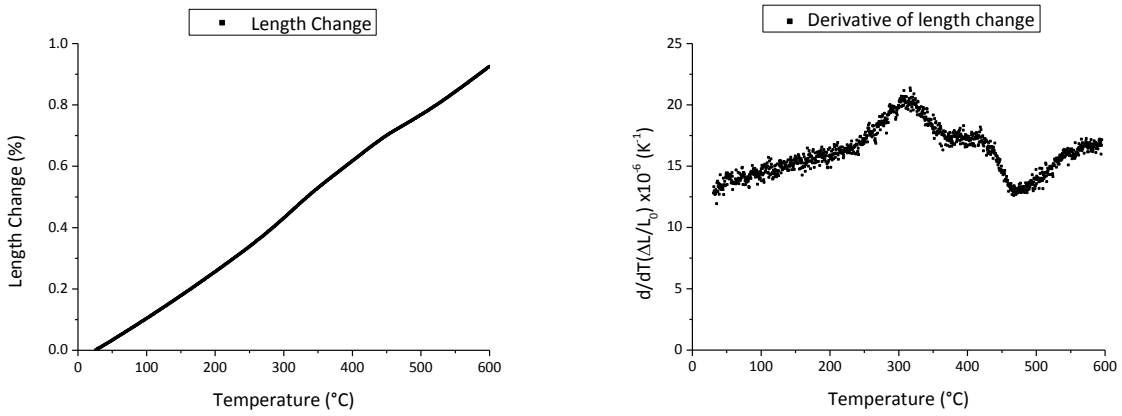

(a) *(b)*

Figure 3.9: (a) Experimentally measured length change $\frac{\Delta L}{L_0}$ of a sample during reheating.

(b) Corresponding derivative $\frac{d}{dT}\left(\frac{\Delta L}{L_0}\right)$ of (a).

As schematically illustrated in Figure 3.10, a relative increase in length, *e.g.* due to decomposition of retained austenite, will show in a graphical plot of the derivative as a peak. Likewise, a relative decrease in length, *e.g.* due to precipitation of carbides from martensite, will show up as a negative peak. The area of the peak in the derivative curve, measured relative to a baseline which is defined here as the derivative curve as if there was no length change, is the length change due to processes other than thermal expansion. This is expressed as

$$\left(\frac{\Delta L}{L_0}\right)_p = \int_{T_1}^{T_2} \alpha_{exp} dT - \int_{T_1}^{T_2} \alpha_b dT \qquad \text{Equation 3.12}$$

where $\left(\frac{\Delta L}{L_0}\right)_p$ is the length change due to decomposition of retained austenite or precipitation of carbides from martensite, T_1 the temperature at which these transformations start, T_2 the temperature at which these transformations end, α_{exp} the experimental derivative $\frac{d}{dT}\left(\frac{\Delta L}{L_0}\right)$ and α_b the derivative $\frac{d}{dT}\left(\frac{\Delta L}{L_0}\right)$ as if there was no decomposition or precipitation.

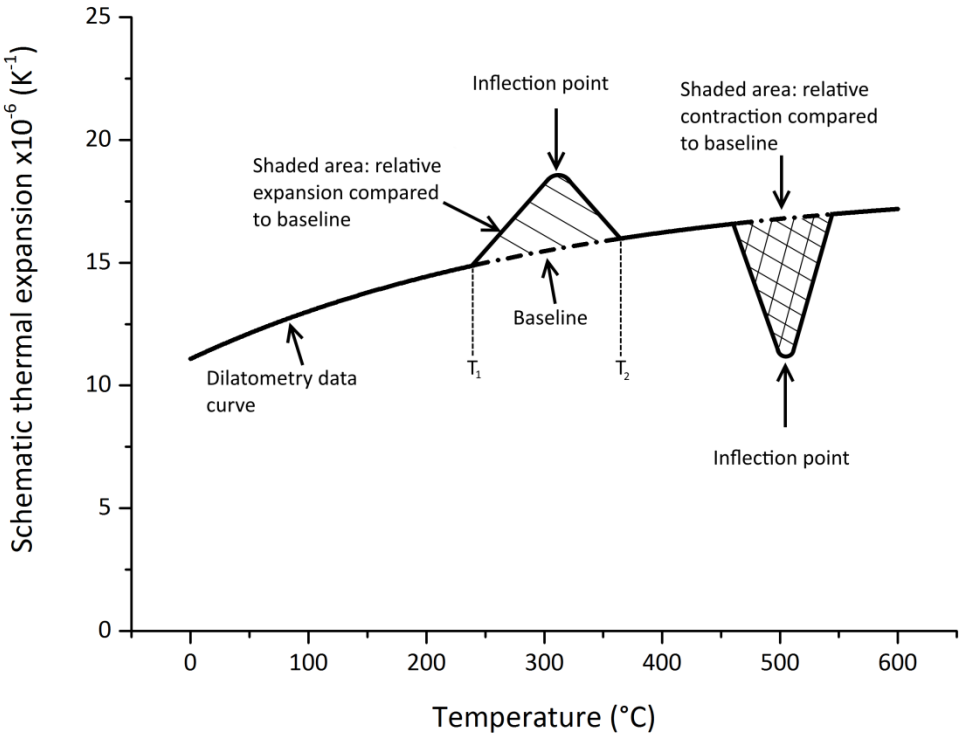

Figure 3.10: Schematic illustration of relative length increases and relative length decreases as they are seen in curves of derivatives of the length change in a dilatometer. Also shown is the schematic location of inflection points used to determine activation energies.

In general, the baseline in this work was taken as a straight line between α_{curve} at T_1 and α_{curve} at T_2. The error in calculating the area of the peak is estimated to be around 10%-15% of peak area. This error is due to inherent variability in (manually) determining T_1 and T_2, the resulting differences in the baseline, and the uncertainty in estimating the value of the baseline after the process.

3.2.6 Determination of activation energies

The activation energies of physical processes such as retained austenite decomposition and precipitation of carbides from martensite can be determined using a Kissinger type analysis [33]–[36] based on dilatometry data. This analysis enables the determination of activation energies based on a method of finding the temperature where an inflection points occurs in a dilatometry curve as a function of heating rate [36]. When neglecting residuals from the derivation leading to Equation 3.13 [36] the general analysis is based on

$$\ln\frac{T_i^2}{\Phi} = \frac{E}{RT_i} + \ln\left(\frac{E}{RK_0}\right) \qquad \textit{Equation 3.13}$$

where T_i is the temperature of an inflection point, Φ the heating rate in K/min, E the activation energy, R the gas constant and K_0 a pre-exponential factor[34]. The temperature T_i is taken as the temperature at which the derivative of the length change versus temperature shows a maximum or minimum, *c.f.* Figure 3.10. These maxima and minima occur at the temperature where the reaction rate is highest [37]. Plotting $\ln\frac{T_i^2}{\Phi}$ *vs.* $\frac{1}{T_i}$ in a Kissinger plot for multiple values of Φ allows applying a

linear fit. The slope of this fit is $\frac{E}{R}$, as can be seen in Figure 3.11. From this slope the activation energy can then be determined. In this work, the maxima and minima were determined using a Gaussian fit around the peak position. The position of the center of the fit was taken as the inflection point.

Due to a limited amount of data in this work (3 different heating rates, 1 experiment per heating rate) and inherent variability in the determination of the inflection points, the error of determining E is estimated to be about 25% of the value of E. In literature, lower errors are calculated due to more heating rates being applied [23].

Compared to other dilatometric studies with tempering or annealing on Q&P steel grades in literature ([11]: figure 3, [14]: figure 7), fewer inflection points are found in QP-G after the treatments specific to this thesis than in literature. Other inflection points not found in this work are related in these studies to carbon clustering and segregation, precipitation of transition carbides ε and η [26][11], and possibly precipitation of alloy carbides [14]. The absence of these inflections points is possibly related to the averaging used to calculate the derivative. Another possibility is that the 200 °C higher partitioning temperatures and longer partitioning times used in this work compared to [14] prevent these processes from occurring.

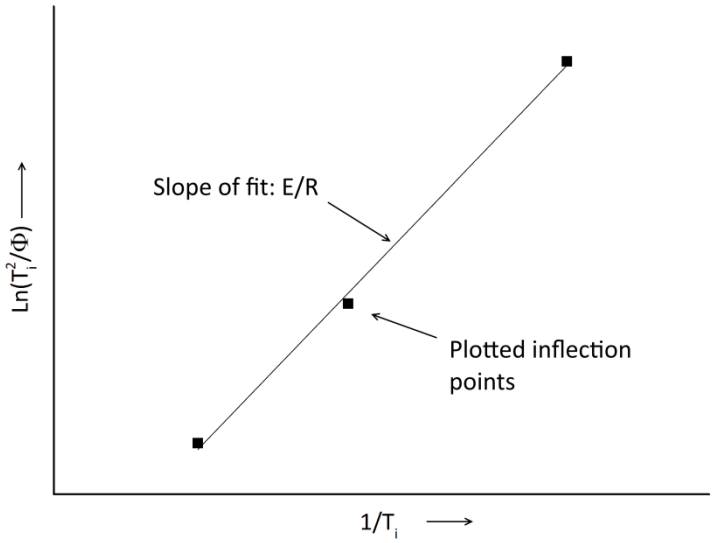

Figure 3.11: Schematic Kissinger-type plot. The slope of the linear fit to the plotted inflection points is E/R.

3.3 Magnetic measurements

3.3.1 Vibrating Sample Magnetometer (VSM)

A Vibrating Sample Magnetometer [38], [39] or VSM is a device that can measure the magnetic properties of a sample. In this work a VSM is used to determine the retained austenite fraction from the magnetic properties. The VSM works by moving a sample inside a uniform applied magnetic field. The voltage induced by this movement can be detected by pickup coils and is proportional to the magnetization (see § 3.3.2) of the sample. A schematic overview of a VSM is presented in Figure 3.12a, while Figure 3.12b shows the VSM setup used in this work.

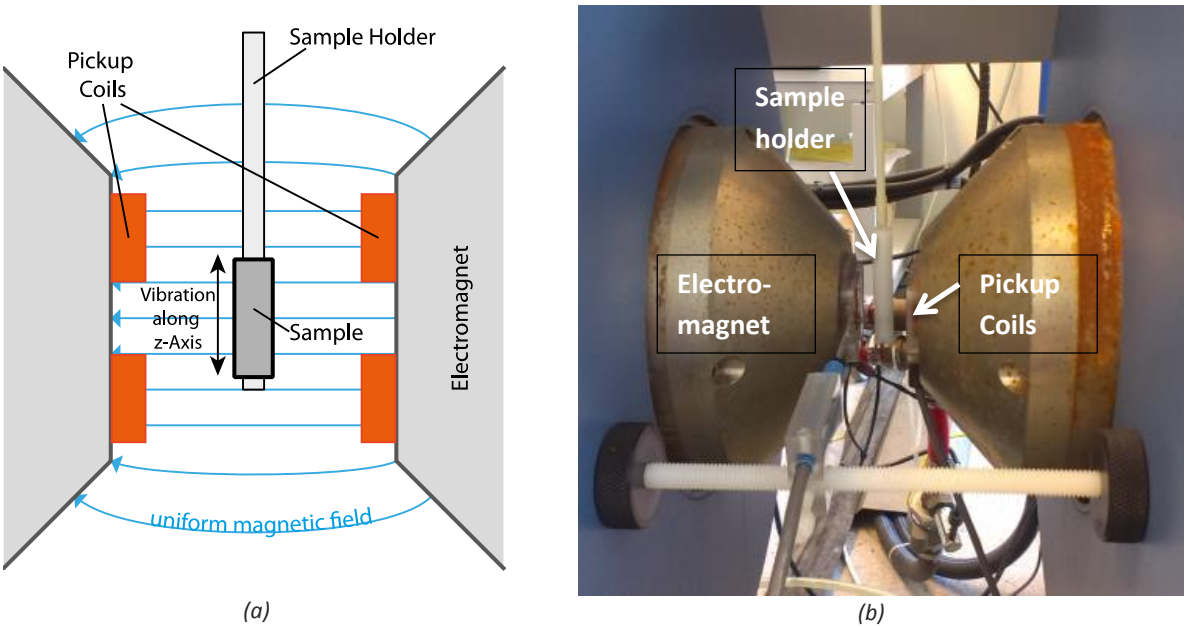

(a) *(b)*

Figure 3.12: (a) Schematic overview of a VSM [40]*. (b) LakeShore 7307 series VSM as used in this work. As a reference for scale, the white sample holder is about 6 cm long.*

A LakeShore 7307 series VSM was used to measure the saturation magnetization (see § 3.3.2). The magnetization during annealing of the sample was measured with the same VSM with a LakeShore oven type 73034 installed. The software controlling the VSM was LakeShore IDEAS-VSM 3.4.0 software. The samples were disk-shaped with a diameter of 3.5 mm and a height of approximately 2 mm, and measured in plane with respect to the magnetic field. A VSM is sensitive to the positioning of the sample within the applied magnetic field [41]–[43]. To ensure repeatable positioning within the applied magnetic field, a specially made sample holder for disc specimens was therefore used.

3.3.2 Background on magnetization

For a detailed background on magnetization, the reader is referred to books by Jiles [44] or Callister [45].

Moving electric charges result in magnetism. The magnetic moment of an atom $\boldsymbol{m}$ is the sum of the magnetic moments of the electrons, which at the atomic level are the moving charges. The magnetization of a material $\vec{\boldsymbol{M}}$ is the vector sum of all atom magnetic moments, or the total magnetic moment divided by its volume:

$$\vec{\boldsymbol{M}} = \sum_{i} \frac{\boldsymbol{m}_i}{V} \qquad \textit{Equation 3.14}$$

The saturation magnetization M_s is the value of maximum magnetization in a material, which occurs when a “large enough” field is applied. The material only has one domain remaining in which all magnetic moments are aligned parallel to the magnetic field.

Any difference in saturation magnetization between a sample containing some retained austenite and a sample containing no retained austenite is directly related to the volume fraction of retained austenite, when neglecting small volume fractions of cementite. This is because ferrite and martensite are ferromagnetic, while austenite is paramagnetic [46]. The saturation magnetization for

pure ferromagnetic iron in this work is taken as 218 Am^2 kg^{-1} at room temperature [47], while for pure paramagnetic iron at room temperature the magnetization is taken as <0.5 Am^2 kg^{-1} ([47] by graphical extrapolation of figure 1, field of 1.5 T). The difference in saturation magnetization between ferromagnetic and paramagnetic phases is large enough that the influence of the saturation magnetization of austenite on the saturation magnetization of the sample can be neglected.

3.3.3 Influence of temperature on saturation magnetization

The Curie temperature T_c is defined here as the temperature below which a material is ferromagnetic, while above T_c the material is paramagnetic. This is caused by thermal precession of the individual atomic moments about the field direction. When the temperature increases, the thermal precession also increases, which causes the measured (spontaneous) magnetization to be smaller than the saturation magnetization. When T_c is reached, this thermal precession is strong enough to overcome the magnetic moment coupling associated with ferromagnetic phases, and the material loses the coupling and the magnetic moments become randomly ordered, *i.e.* paramagnetic.

The dependence on temperature of the magnetization of iron for ferromagnetic phases can be described by an equation proposed by Arrott and Heinrich [48], and given in a modified form used by Bojack [49]:

$$M_s(s) = M_0 \frac{(1-s)^{\beta}}{(1 - \beta s + A s^{\frac{3}{2}} - C s^{\frac{7}{2}})} \qquad \textit{Equation 3.15}$$

where $M_s(s)$ is the saturation magnetization at a dimensionless temperature $s = \frac{T}{T_c}$, M_0 is the saturation magnetization at 0 K, and β, A and C are material dependent constants.

3.3.4 Experimental procedures

The procedure to determine the retained austenite content in steels with magnetic measurements was derived from the method described in [46]. A standard NIST nickel specimen was used to calibrate the VSM. Magnetization curves were made with a stepwise applied magnetic field from 1.7 T to -1.7 T as can be seen in Figure 3.13. The step size was 0.1 T. The value of interest, saturation magnetization M_s, was taken as the average of the absolute magnetization values at the maximum and minimum (*i.e.* 1.7 T and -1.7 T) applied magnetic field. The unit of M_s in this work is Am^2 kg^{-1}, which is the total magnetic moment as measured by the VSM, divided by the mass of the sample. Compare this to Equation 3.14, where the magnetization $\vec{M}$ is defined as the total magnetic moment divided by the volume. With the practical facilities available, accurate measurement of mass is more easily achieved than accurate measurement of volume, and since volume and mass are directly related by density, the use of Am^2 kg^{-1} is allowed as unit for magnetization.

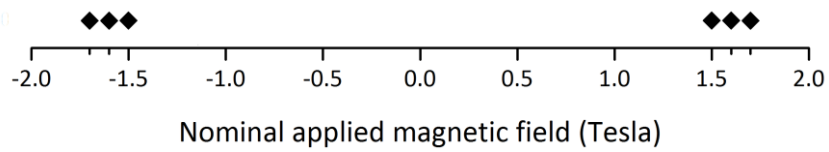

Figure 3.13: VSM program used for determining the saturation magnetization. The values for ±1.7 T are nominal, in practice ±1.62 T was the maximum reachable applied magnetic field.

The volume fraction retained austenite of each sample f_γ was then determined by a comparison of the average M_s value of at least 3 measurements in the austenite containing sample to a directly quenched specimen which was confirmed by XRD to have almost no (<1%) retained austenite:

$$f_\gamma = 1 - \frac{M_s(c)}{M_s(r)} \qquad \textit{Equation 3.16}$$

where $M_s(c)$ is the saturation magnetization of the austenite containing sample and $M_s(r)$ is the saturation magnetization of the austenite free quenched sample. The standard deviation in determining the fraction of retained austenite by this method is <1% retained austenite. The standard deviation of the fraction of retained austenite was determined by

$$\sigma = \sqrt{\left(\frac{1}{M_s(r)}\right)^2 \sigma_{M_s(c)}^2 + \left(\frac{M_s(c)}{M_s(r)^2}\right)^2 \sigma_{M_s(r)}^2} \qquad \textit{Equation 3.17}$$

where $\sigma_{M_s(c)}$ is the standard deviation of measurements of $M_s(c)$, and $\sigma_{M_s(r)}$ the standard deviation of measurements of $M_s(r)$.

3.3.4.1 Measuring volume fractions of retained austenite during isochronal annealing

To measure the amount of retained austenite during a heating, the following procedure as schematically shown in Figure 3.14 was performed in the VSM:

1) First heating with 5 °C min^{-1} to 600 °C under constant applied magnetic field of 1.5 T
2) Isothermal holding at 600 °C for 20 minutes
3) A cool down to room temperature by natural cooling of the VSM oven (see [49] for a description of the cooling rate)
4) Second heating with 5 °C min^{-1} to 600 °C under constant applied magnetic field of 1.5 T

This procedure is partly modelled after [17]. Some fraction of retained austenite decomposes during the first heating to 600 °C. More retained austenite decomposes during the isothermal holding and the cooling down to room temperature. If the microstructure is assumed to be fully ferritic after the cooling (*i.e.* fully ferromagnetic) the second heating occurs without any phase transformations. This allows the calculation of the dependence of the M_s of ferrite on temperature in this material using Equation 3.15.

The fit of the second heating with Equation 3.15 allows the establishment of a multiplication factor to calculate the equivalent room temperature magnetization of the sample from the magnetization values recorded during the reheating. This is done by calculating the saturation magnetization at room temperature according the fit to Equation 3.15, and dividing the fitted saturation magnetization at each recorded temperature by this number:

$$MF(T) = \frac{M_{fs}(T_r)}{M_{fs}(T)} \qquad \textit{Equation 3.18}$$

where MF is the multiplication factor at each measured temperature T, $M_{fs}(T_r)$ is the saturation magnetization at room temperature according to the fit and $M_{fs}(T)$ is the saturation magnetization at each measured temperature according to the fit.

Multiplying the recorded magnetization values during the first heating by the corresponding multiplication factor then gives the equivalent room temperature magnetization at each temperature. This allows a direct calculation of the retained austenite fraction using Equation 3.16.

In Figure 3.14a, a plot of the magnetization curves of such an experiment is shown, and a fit to the second heating using Equation 3.15 fits well (R^2 = 0,9999). This indicates that no further phase transformations are occurring. The decomposition of retained austenite can be deduced from the changes in slope of the first heating, very clearly seen in the temperature range 300 °C to 400 °C.

In Figure 3.14b, the resulting corrected equivalent room temperature magnetization of the same experiment is shown. The increase in magnetization clearly shows retained austenite decomposition.

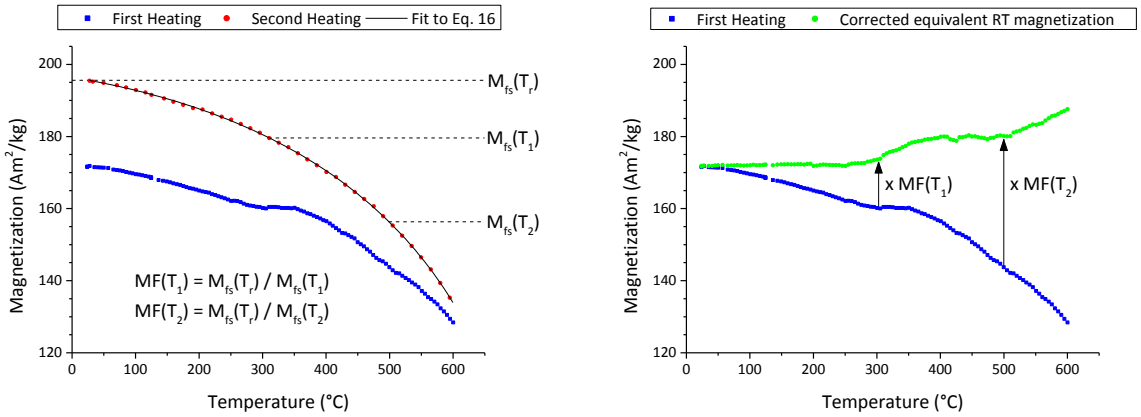

(a) *(b)*

Figure 3.14: (a) Results of a typical annealing experiment in the VSM. For the second heating, only 1 out of every 4 data points is shown for better visibility of the fit. (b) Corrected equivalent RT magnetization.

3.4 X-ray Diffraction

X-Ray Diffraction experiments were used to determine the volume fraction of retained austenite and determine the lattice parameter of retained austenite at room temperature. A Bruker D8 Advance Diffractometer equipped with a Vantec position sensitive detector was used, using Co Kα1 radiation (λ = 1.78897 Å), an acceleration voltage of 45 kV and current of 35 mA, while the sample was spinning at 30 rpm. The measurements were performed in the 2θ range of 40°-130°, using a step size of 0,035° 2θ, with a counting time per step of 4 s. The volume fraction of retained austenite and the errors in determing the retained austenite fraction were calculated using the Jatczak model [50] as described in [51], [52].

The lattice parameter of retained austenite was determined by stripping the Co Kα2 intensity, fitting the peaks with a pseudo Voigt function, correcting the peak position for sample displacement and goniometer errors which were determined with LaB_6 calibration measurements, and from the peak position of the {111}, {200}, {220} and {300} peaks the lattice parameter a was calculated using

$$a = d\sqrt{h^2 + k^2 + l^2} \qquad \textit{Equation 3.19}$$

$$d = \frac{\lambda}{2sin\theta} \qquad \textit{Equation 3.20}$$

where d is the lattice spacing of the diffracting $\{hkl\}$ plane, λ the wavelength used and θ the measured 2θ peak position divided by two. The lattice parameter used in this work is the average of the 4 lattice parameters found, and the error the standard deviation of those 4 lattice parameters.

Using the lattice parameter, the amount of carbon in retained austenite was calculated by Equation 3.21:

$$a = 0.355\,nm + 0.044\frac{nm}{wt.\,\%} \times X_c^{\gamma} \qquad \textit{Equation 3.21}$$

where a is the lattice parameter in nm and X_c^{γ} the weight percentage of carbon in retained austenite. The error in determining the carbon percentage is estimated as 0.05 wt. % C

3.5 Microscopy

3.5.1 Light Optical microscopy

Due to its limited resolution, Light Optical Microscopy (LOM) is not the best technique to analyse the fine martensitic microstructures. Larger microstructural features however, are best seen with LOM. In this work, microstructural banding was analysed with the LOM (*e.g.* Figure 3.1).

Light Optical Microscopy was performed using a Keyence VHX-5000 series digital microscope. The lenses used were the VH-Z100R (100x-1000x) and the VH-Z250R (250x-2500x).

3.5.2 Scanning Electron Microscopy

Scanning Electron Microscopy (SEM) was used to resolve and image the fine martensitic microstructures. Furthermore, EBSD measurements (see §3.5.3) were performed in a SEM.

Scanning Electron Microscopy was performed using a JEOL JSM-6500F series field emission gun SEM, using a Secondary Electron Imaging detector. The acceleration voltage was 15 kV and the nominal working distance was 10 mm.

3.5.3 Electron Backscatter Diffraction

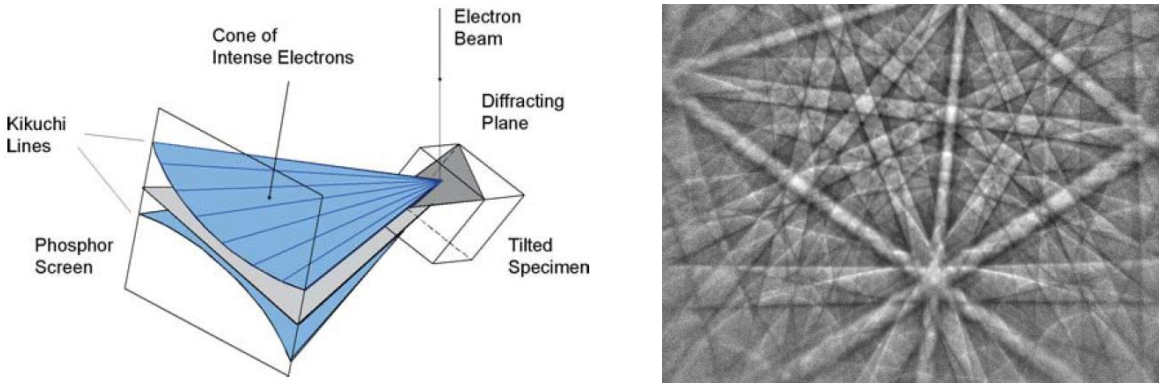

(a) *(b)*

Figure 3.15: (a) Working principles of EBSD [53]. *(b) Example of an EBSP made in austenitic steel* [54].

In this work, EBSD is used to determine the morphology of austenite and ferrite grains and their positions. Figure 3.15a shows a schematic of the working principles of EBSD. In the SEM, the incident electron beam is held stationary at a certain position. Primary electrons which satisfy Bragg's law given in Equation 3.20 can backscatter. These electrons are then recorded on a phosphor screen. The resulting image is called an Electron Back-Scattered Pattern (EBSP) or Kikuchi pattern, and an example is shown in Figure 3.15b. The visible lines are called Kikuchi bands. In steel, FCC and BCC phases can be distinguished because of their differing characteristic Kikuchi patterns. Identification of

the phases and determination of their crystallographic orientation is performed by comparing the recorded Kikuchi patterns to reference patterns. For a detailed background on Electron Backscatter Diffraction (EBSD) and the underlying principles, the reader is referred to [53].

EBSD measurements were performed in a JEOL 6500F series SEM, using an Oxford Instruments Nordlys II detector. The acceleration voltage was 20 kV, the beam current 1.2 nA, the working distance 25 mm and the tilt angle 70°. 4x4 binning of the detector was used. A square grid of 300x300 pixels was scanned with a step size of 50 nm, resulting in a scanned area of 15x15 μm^2. Acquisition and post processing of Kikuchi patterns was performed with Oxford Instruments Channel 5 software.

A different setting was used for a single experiment, sample QT260H425. The acceleration voltage was 15 kV. A square grid of 360x360 pixels was scanned with a step size of 30 nm, resulting in a scanned area of 10.8x10.8 μm^2.

The post-processing involved the phase identification of the created EBSPs. Based on previously performed calibration measurements in this setup, no misidentification is expected using 9 Kikuchi bands. Phase identification was therefore carried out using 9 Kikuchi bands. After the phase identification, cleaning of the resulting maps was performed. Pixels that were unable to be identified due to insufficient band contrast in the EBSP were identified by automated iterative nearest identified neighbor filling.

3.5.3.1 Limitations of EBSD

In this work, three problems were encountered which influenced the analysis of EBSD maps. First, retained austenite films in Q&P steels are expected to be 20 to 100 nm in size [55]. The employed step sizes of 30 and 50 nm are on the same order of magnitude. This means that film like retained austenite will be in regions of low band contrast close to grain boundaries, and therefore not easily identified. An example of a region with low band contrast is indicated in Figure 3.16c. The lack of indexing will lead to an underestimation of the retained austenite fraction as determined by EBSD. In some specimens in this work, <0.1 % retained austenite was detected by EBSD while 9 % retained austenite was determined with magnetic methods.

Second, automated iterative nearest identified neighbor filling can possibly lead to an incorrect determination of the size and morphology of retained austenite. Figure 3.16a shows a cleaned EBSD map containing seemingly large retained austenite grains. Figure 3.16b shows the same EBSD map, but before cleaning. Two RA grains are marked, showing the effect of the cleanup process. The RA grains are clearly larger after filling, and filling might therefore influence the characterization of RA.

Third, Figure 3.16c and Figure 3.16d show a region of low band contrast filled in as retained austenite in the marked grain. Regions of low band contrast are likely to be M2 [56]. This region is therefore incorrectly identified as retained austenite due to the filling procedure.

The combination of these effects means that significant care has to be taken in analyzing automatically cleaned EBSD maps. In this work, cleaned EBSD maps will therefore be accompanied by the corresponding uncleaned versions. While the problem of non-indexed pixels is an experimental limitation and will remain, the effect of the cleaning procedure can be determined by analyzing both cleaned and uncleaned EBSD maps.

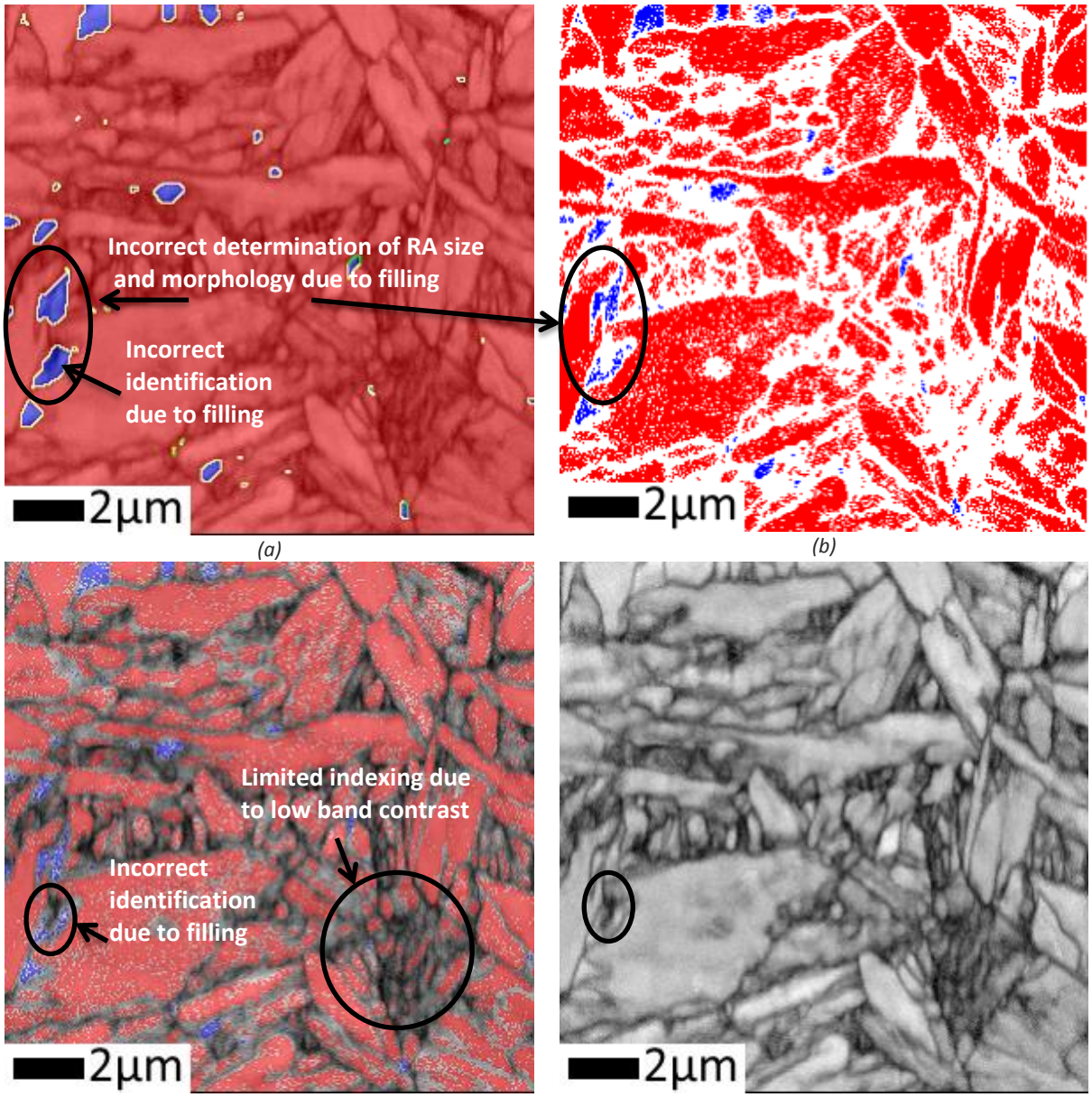

Figure 3.16: Example of EBSD maps. (a) Combined phase and band contrast map. Blue is identified as FCC, red identified as BCC. This map has been cleaned. (b) Phase map. Blue is identified as FCC, red identified as BCC. This map has not been cleaned. White regions are non-indexed regions. (c) Combined phase and band contrast map. Blue is identified as FCC, red identified as BCC. This map has not been cleaned. (d) Band contrast map.

Of further note is that in some experiments, drift of the electron beam was observed. While the EBSD maps are shown square, in reality they could be distorted. An example of drift distortion is shown in Figure 3.17. The approximate boundary of the actual scanned region is marked with solid lines, while the region supposed to be scanned is marked with dotted lines.

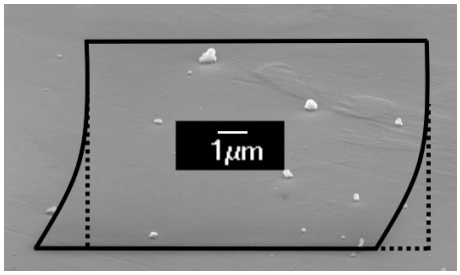

Figure 3.17: Drift of the electron beam.

Chapter 4 Results and Discussion

4.1 Microstructures after Quenching & Partitioning

As mentioned in § 3.1.2, Q&P treatments with quenching temperatures varying from 140°C to 340 °C were performed on QP-G. The resulting microstructures are quantified in § 4.1.1 and § 4.1.2. The microstructure of a representative selection of samples is characterized in § 4.1.3.

4.1.1 Quantification of phases

Since the aim of this work is to investigate the thermal stability of retained austenite, knowledge of the fraction of retained austenite f_γ in the sample is essential. Using a combination of magnetic methods and XRD[1], the volume fraction of retained austenite was determined and is shown in Figure 4.1a. The maximum fraction of retained austenite was 0.15 and was found in the sample with a Quenching Temperature of 260 °C, QT260. The fraction of retained austenite as a function of quenching temperature follows the general prediction made by Speer *et al.* [9].

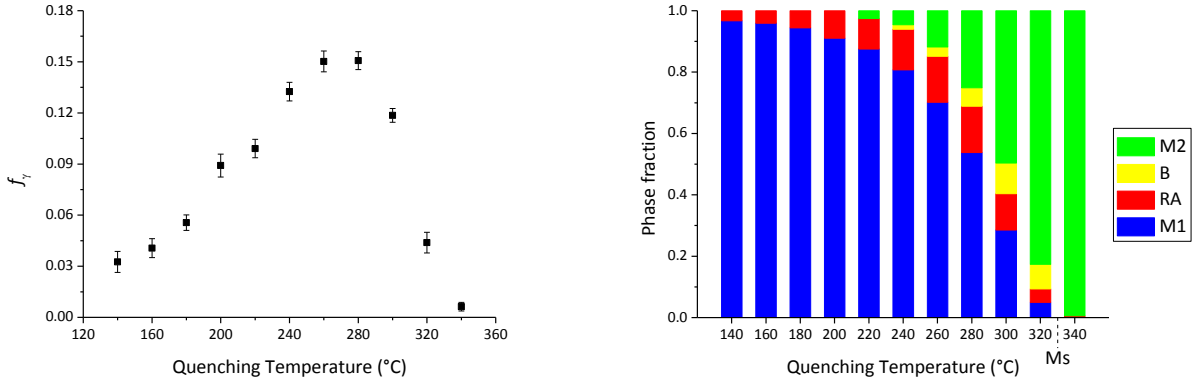

Figure 4.1: (a) f_γ in Q&P specimens as determined by magnetic methods and XRD. (b) Measured phase fractions of retained austenite and bainite, fractions of M1 as determined with the K-M equation and fractions of M2 as determined by a microstructural balance using $f_{M1} + f_{RA} + f_B + f_{M2} = 1$.

The volume fractions of M1 (Martensite from first quench) were determined using the Koistinen-Marburger equation with the parameters as given in §3.2.4.2. The phase fractions are shown in Figure 4.1b. These estimations were compared with phase fractions determined from dilatometry data. The agreement was found to be within 3%, except for sample QT320. A QT of 320 °C is above the theoretical martensite start temperature T_{km} of 313.1 °C used in the K-M equation. The fraction of M1 in a sample with a quenching temperature of 320 °C is therefore not predictable using the K-M equation. The phase fraction of M1 in sample QT320 as determined from dilatometry data is shown in Figure 4.1b instead.

In some specimens, bainite formation is detected during partitioning. Figure 4.2 shows the length change during partitioning. The maximum length change of 0.07% is seen in sample QT300. This can be correlated to a maximum bainite fraction of about 0.1. Samples with a QT higher than 240 °C show some length change, with the exception of sample QT340, which has a QT above Ms. Samples with a QT lower than 240 °C show very little length change. Taken together, this suggests that bainite formation is occurring due to martensite nuclei promoting the bainite reaction [57]. AT QT's lower

[1] See Appendix A for details on this calculation and a comparison of RA fractions determined by VSM and XRD.

than 240 °C, partitioning of carbon from martensite will enrich the retained austenite with carbon so no bainite formation can occur. Sample QT340 has a quenching temperature above Ms. No martensite nuclei will be present in sample QT340 to promote bainite formation, and hence bainite formation will be limited compared to samples with martensite nuclei.

Volume fractions of M2 (Martensite from second quench) were calculated by balancing the volume fractions of the microstructural constituents using $f_{M1} + f_{RA} + f_B + f_{M2} = 1$.

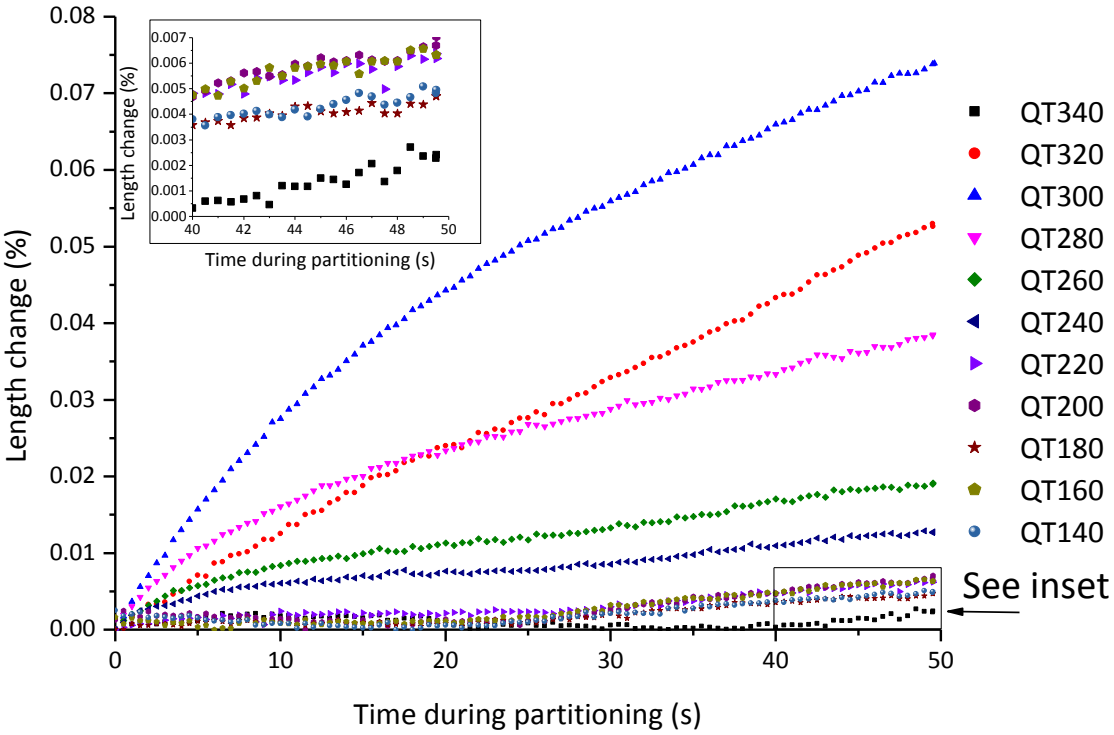

Figure 4.2: Length change (%) during partitioning. The inset is shown for more clarity, as some dilatometry curves are hard to visually separate.

4.1.2 Lattice parameter of retained austenite

The lattice parameter and carbon content of retained austenite as determined by XRD is shown in Figure 4.3a. The lattice parameter for sample QT340 could not be determined, because the retained austenite fraction is below the detection limit of XRD. The smallest lattice parameter is found in samples QT240 and QT260. Samples QT140-QT220 show a trend of increasing lattice parameter at decreasing quenching temperatures. This can be correlated with the fraction of M1 formed during the quench. More martensite formed means more carbon is available to partition into austenite, thereby increasing the lattice parameter.

Changing the quenching temperature between 280 °C and 320 °C seems to slightly increase the lattice parameter at increasing quenching temperatures. This is regarded as an effect of bainite formation during partitioning.

Figure 4.3b shows the carbon concentration in retained austenite plotted against the retained austenite fraction. The general trend is that decreasing amounts of retained austenite contain increased carbon concentrations.

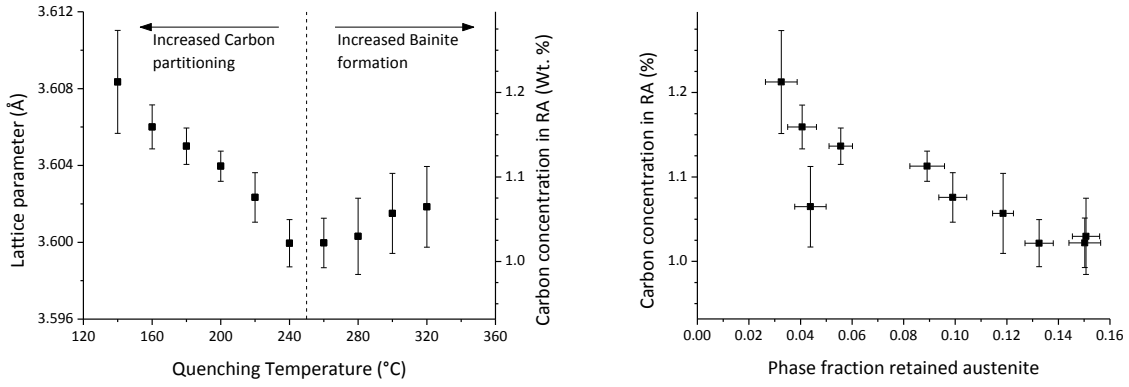

(a) *(b)*

Figure 4.3: (a) Lattice parameter of retained austenite and carbon content in retained austenite of Q&P specimens. (b) Carbon concentration in retained austenite plotted against the fraction of retained austenite.

4.1.3 Characterization of microstructure

The microstructures of samples QT160, QT260 and QT320 were characterized in further detail. This characterization was performed with SEM, OM, EBSD and XRD. Based on SEM micrographs, retained austenite fractions and lattice parameters, the microstructures of the selected samples are thought representative for the whole range of Q&P treatments made in this work. The basis of this selection is discussed in further detail in §4.2.1.

4.1.3.1 Analysis of sample QT160

According to the analysis in § 4.1.1, the microstructure of sample QT160 consists of about 4% RA and 96% M1. Figure 4.4a and Figure 4.4b show uncleaned and cleaned versions respectively of EBSD phase maps of sample QT160. Cleaning did not significantly affect the resulting retained austenite grain size and morphology. Approximately 1.5% RA is detected in the EBSD. The detected retained austenite grains are mostly retained austenite grains with a width > 100 nm and a maximum length of approximately 1 µm. Film-like retained austenite in Q&P steels has a film width of 20-100 nm [58]. This film width is in the same order of magnitude as the step size of 50 nm of the EBSD measurement. Film-like RA is therefore unlikely to be resolved reliably, due to insufficient band contrast. Some scattered single pixels of RA are seen, and these are most likely part of film-like retained austenite.

Figure 4.4c and Figure 4.4d show SEM micrographs of this sample, at 2000x and 10000x magnification respectively. Figure 4.4c shows an overview of the microstructure, which is consistent with tempered martensite. In Figure 4.4d, some carbides can be seen in the tempered martensite. Furthermore, some retained austenite grains with a width of approximately 100 to 200 nm and length of 1 µm are marked in Figure 4.4d. Film-like retained austenite grains are not detected in these figures. It is assumed that the morphology of the RA is about 50% film, and 50% RA grains with a width > 100 nm and a maximum length of approximately 1 µm.

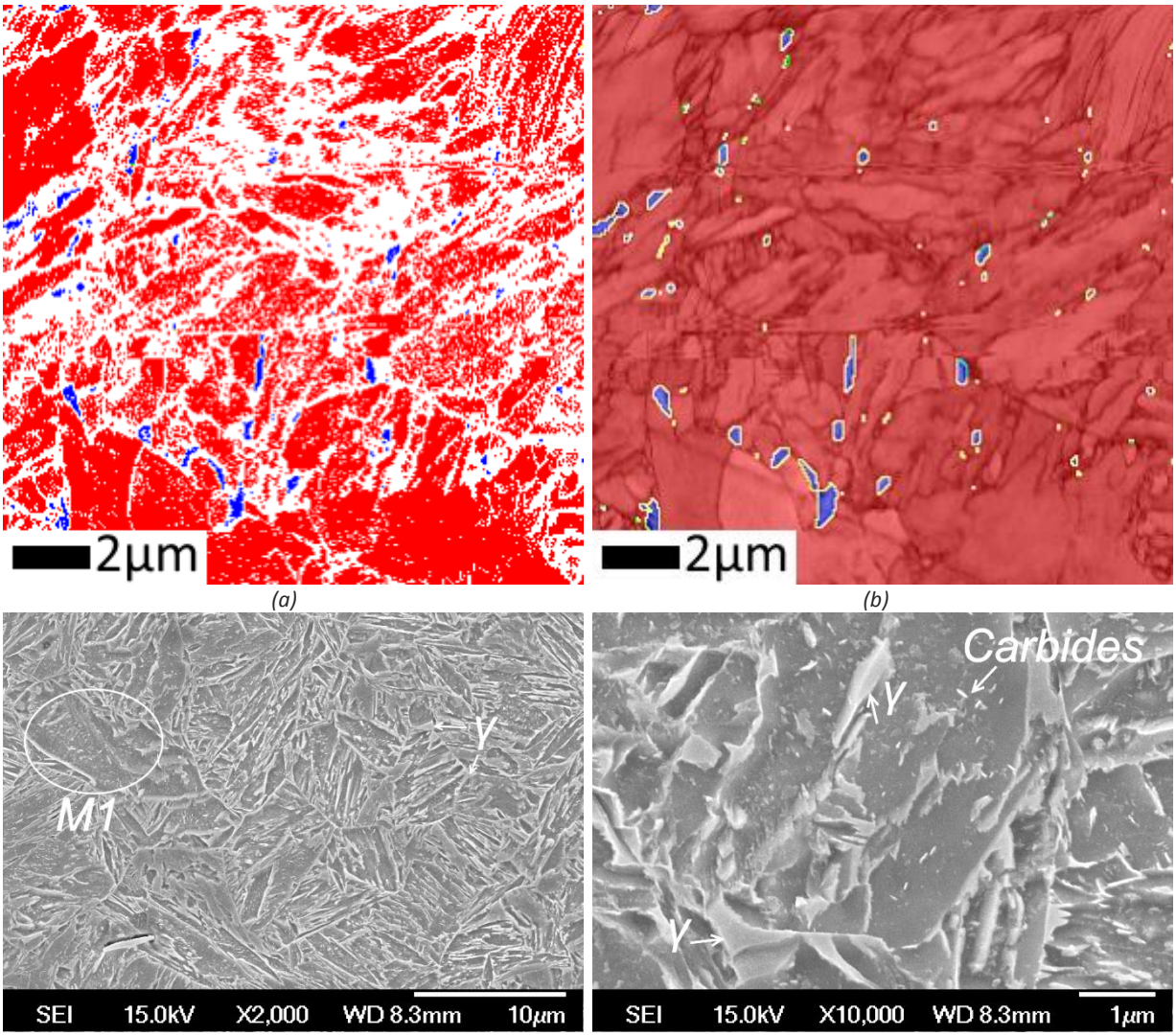

Figure 4.4: Microstructure of sample QT160. (a) Phase map before cleaning. BCC is shown in red, FCC in blue. (b) Combined EBSD band contrast and phase map. Cleaned version. (c) (d) SEM micrograph.

4.1.3.2 Analysis of sample QT260

According to the analysis in § 4.1.1, the microstructure of sample QT260 consists of about 15% RA, 70% M1, 3% bainite and 12% M2. Figure 4.5a and Figure 4.5b show SEM micrographs of this sample, at 2000x and 10000x magnification respectively. Figure 4.5a clearly shows well-etched and less-etched regions. The less-etched regions correspond to RA and M2 [27]. However, retained austenite etches much less than M2 while retained austenite remains featureless. This allows visual separation of RA and M2. The feature marked "γ (+M2)" in Figure 4.5b consists of M2 in its center and RA at its left and upper edges. This is consistent with a blocky type austenite grain in which the center was not sufficiently enriched with carbon to stabilize against the martensitic transformation. Features like this are also predicted with phase field models [59], and shown in more detail elsewhere in this work (*c.f.* Figure 4.18b).

Bainite is hard to distinguish from martensite in SEM images, and therefore no identification of the small bainite fraction was attempted.

A smaller fraction of carbides compared to sample QT160 can be seen in Figure 4.5b, consistent with a higher fraction of carbon in solid solution in retained austenite.

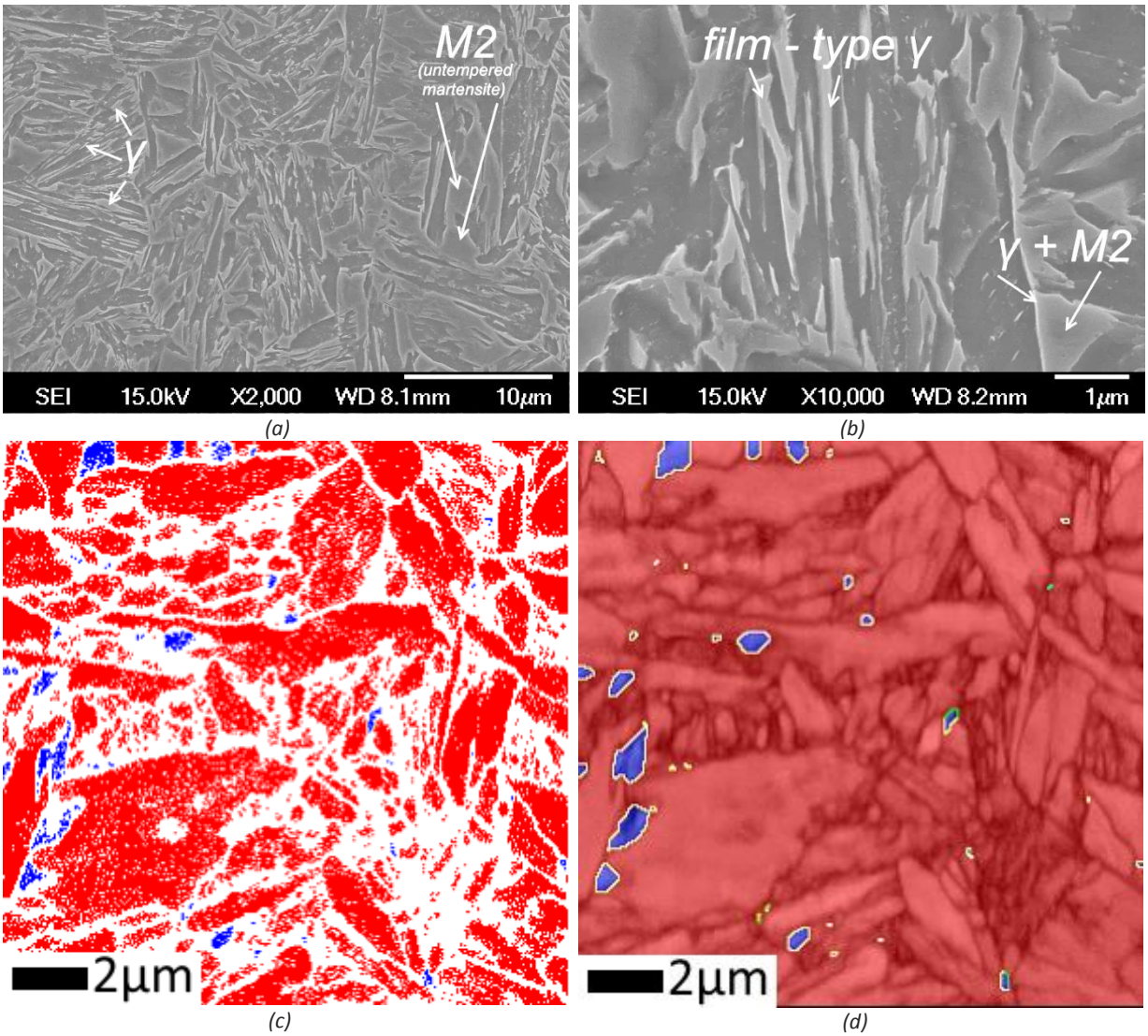

Figure 4.5: Microstructure of sample QT260. (a) (b) SEM micrograph (c) Phase map before cleaning. BCC is shown in red, FCC in blue. (d) Combined EBSD band contrast and phase map. Cleaned version of (c).

Figure 4.5c and Figure 4.5d show cleaned and uncleaned versions respectively of EBSD phase maps of sample QT260. Some RA grains are significantly inflated due to the cleaning process, as shown in Figure 3.16. About 2.5% of RA was detected with EBSD. This means a large fraction of RA was undetectable with EBSD, suggesting a small RA grain size and film-like morphology. A large number of regions with low band contrast exist in this EBSD measurement. These regions likely contain the film-like RA grains.

4.1.3.3 Analysis of sample QT320

According to the analysis in § 4.1.1, the microstructure of sample QT320 consists of about 15% M1 and bainite, approximately 4.5% RA and 80% M2. Figure 4.6a Figure 4.6b show EBSD phase maps of sample QT320. Cleaning did not significantly affect size and morphology of the detected RA grains. About 0.1% RA was detected with EBSD. This suggests that a large majority of the RA has a film-like morphology. SEM micrographs, shown in Figure 4.6c and Figure 4.6d, show some features that might be identified as film-like RA. Blocky type RA is not observed in any available SEM pictures of this sample.

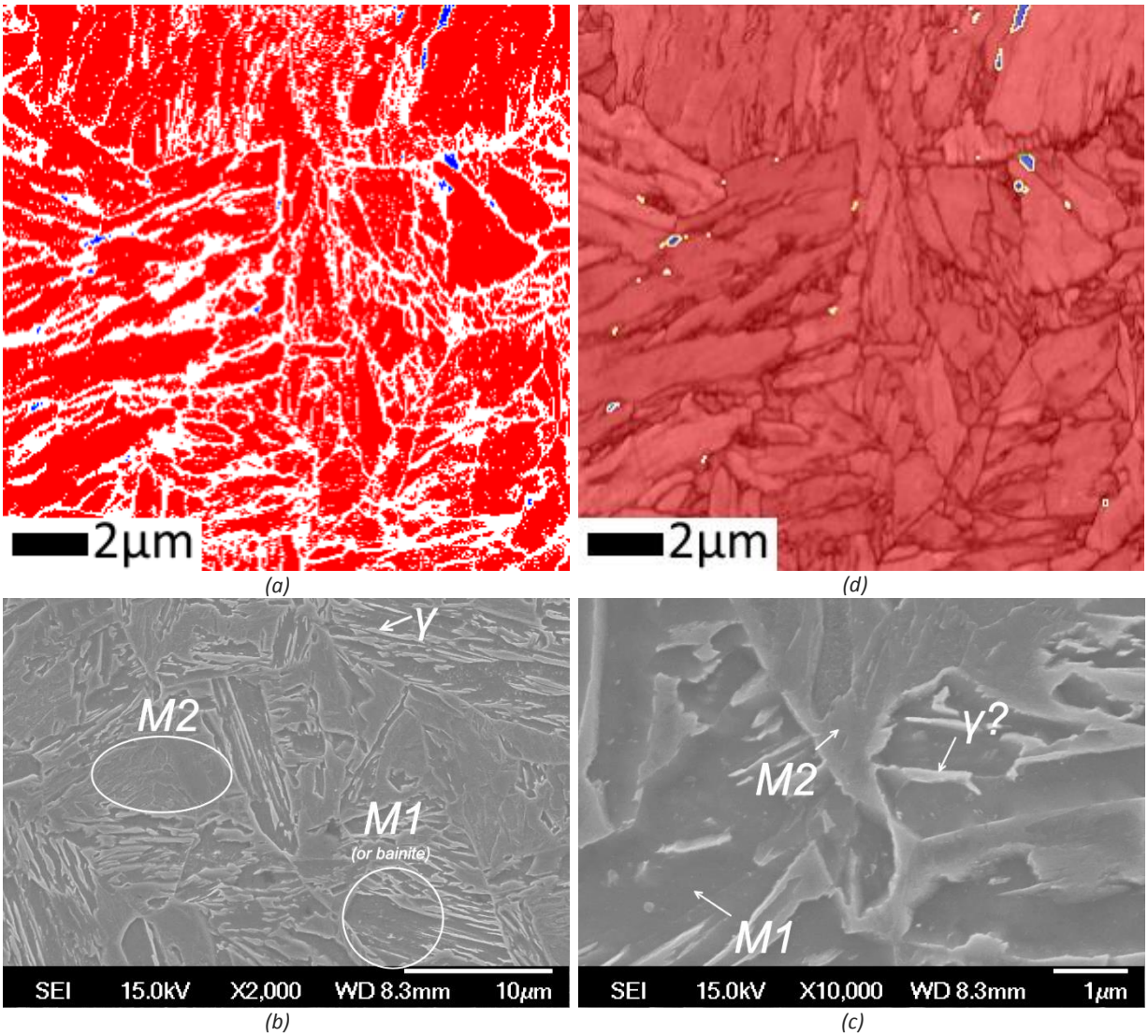

Figure 4.6: Microstructure of sample QT320. (a) Phase map before cleaning. BCC is shown in red, FCC in blue. (b) Combined EBSD band contrast and phase map. (c) (d) SEM micrograph

An overview of the microstructure at 2000x magnification is shown in Figure 4.6c. Regions of tempered martensite (M1) or bainite, and regions of untempered martensite M2 are visible. Carbides are only present in the tempered regions.

4.1.3.4 X-ray Diffraction results

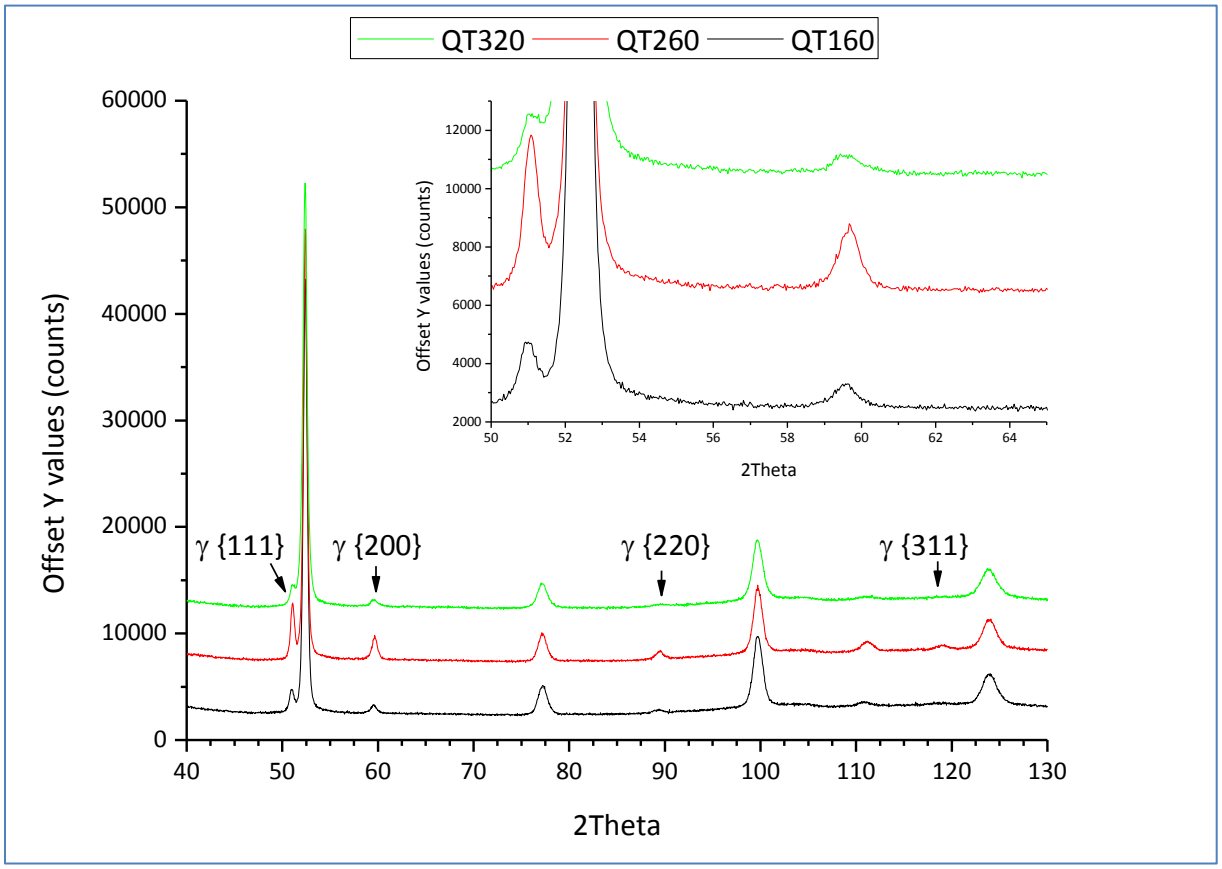

Figure 4.7: XRD spectrum of samples QT160, QT260 and QT320. The applied offset values are +4000 for sample QT260 and +8000 for sample QT320. The inset shows the {111} and {200} peaks of austenite in further detail.

Figure 4.7 shows the XRD spectrum of samples QT160, QT260 and QT320. The retained austenite peaks in sample QT260 are stronger relative to the other samples. This confirms that the largest fraction of RA is present in sample QT260.

Some texture might be present in all these materials. The {200} peak of austenite and the {110} peak of ferrite are stronger than expected. This could indicate the Pitsch orientation relationship: $\{010\}_\gamma // \{101\}_\alpha$ $<101>_\gamma // <111>_\alpha$ [60][61].

4.1.4 Summary: The microstructure of Q&P samples in this work

The microstructural constituents of samples with a QT of 160, 260 and 320 °C are summarized in Table 4.1.

Table 4.1: Summary of the microstructural constituents of samples analyzed in §4.1.3.

Sample	QT160	QT260	QT320
Volume fraction of retained austenite f_γ	0.04 ±0.006	0.15 ±0.006	0.045 ±0.006
Carbon content in retained austenite (wt. %)	1.15 ± 0.05	1.02 ± 0.05	1.07 ± 0.05
Morphology of retained austenite	50%/50% film-like RA and RA with width >100 nm, maximum length of 1 µm	Majority (>80%) of film-like RA, some larger grains >100 nm	Large majority (>95%) of film-like RA
Volume fraction of martensite from the first quench f_{M1}	0.96 ± 0.02	0.7 ± 0.03	0.07 ± 0.03
Volume fraction of bainite f_B	0	0.03 ± 0.01	0.08 ± 0.02
Volume fraction of martensite from the second quench f_{M2}	0	0.12 ± 0.04	0.8 ± 0.05
Carbides	Yes, located in tempered martensite M1	Yes, fewer than QT160, located in tempered martensite M1	Yes, fewer than QT160 located in M1, none in M2

4.2 Retained austenite decomposition: reheating with 5 °C s^{-1} to 700 °C

An initial analysis of the thermal stability of retained austenite was performed by heating Q&P treated samples to 700 °C as shown in Figure 3.2b. The reheating rate was 5 °C s^{-1}. Upon reaching 700 °C, the samples were directly quenched to room temperature. An analysis of the resulting microstructure was performed, and this analysis is discussed in §4.2.1 and §4.2.2. A comparison between the Q&P microstructures before reheating (as analyzed in §4.1) and after reheating to 700 °C will be made in §4.2.3.

4.2.1 Quantification of phases

Figure 4.8 shows the fraction of retained austenite as determined by magnetic methods and XRD[2]. Samples with a QT between 140 and 180 °C and between 320 and 340 °C show an increase in the fraction of retained austenite f_γ after reheating. Samples with a QT between 200 and 300 °C show a decrease in the fraction of retained austenite after reheating. Based on this observation, the samples were divided into three groups. Region I contains samples with a QT between 140 and 180 °C, region II contains samples with a QT between 200 and 300 °C and region III contains samples with a QT between 320 and 340 °C.

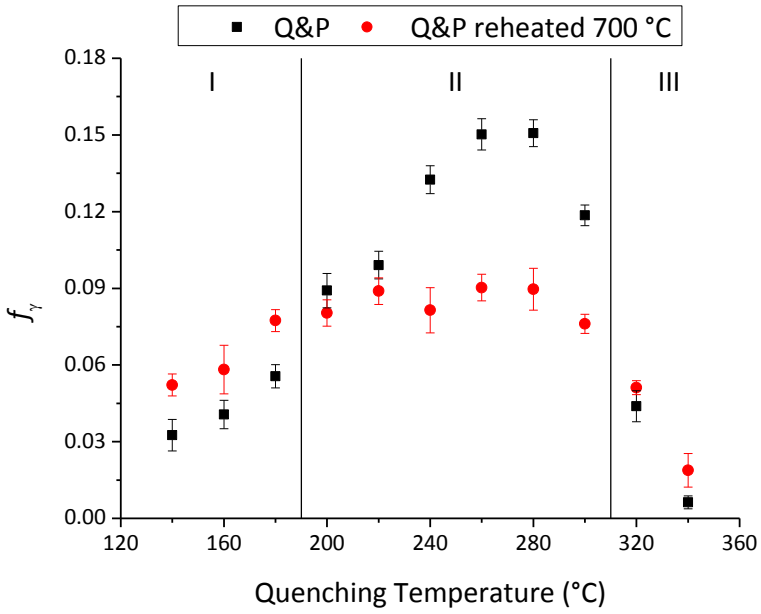

Figure 4.8: Fraction of RA as determined by VSM/XRD. For the samples in region I and III, a higher fraction of RA was detected after the reheating, while in region II a lower fraction of RA was observed.

The lattice parameter of retained austenite as determined by XRD is shown in red in Figure 4.9a. Shown in black as a comparison are the corresponding samples without reheating. A decrease in the lattice parameter after reheating is seen in samples with a QT between 140 and 220 °C. For samples with a QT between 240 and 320 °C, an increase in lattice parameter after reheating is observed.

The lattice parameter and carbon content of retained austenite as determined by XRD is shown in Figure 4.9a. The increase in f_γ in region I is coupled with a decrease in the lattice parameter. In contrast, in region III, the increase in f_γ in region III is coupled with an increase in the lattice parameter. The decrease in f_γ in region II does not show significant effects on the lattice parameter.

[2] See Appendix A for details on this calculation and a comparison of RA fractions determined by VSM and XRD.

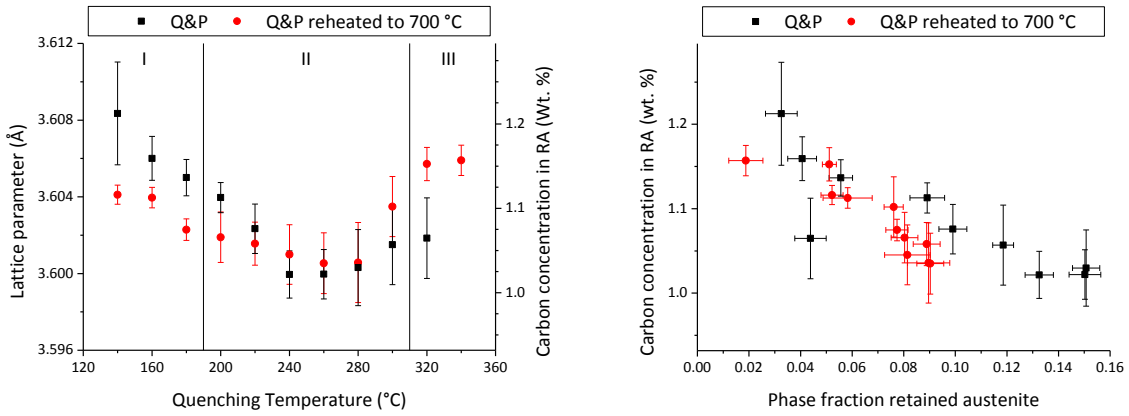

(a) *(b)*

Figure 4.9: (a) Lattice parameter of retained austenite and carbon content in retained austenite of Q&P specimens, before and after reheating. (b) Carbon concentration in retained austenite plotted against the fraction of retained austenite.

Figure 4.9b shows the carbon concentration of retained austenite plotted against the phase fraction of retained austenite. In contrast to the Q&P samples as discussed in §4.1.2, the reheated Q&P samples show no clear correlation between the phase fraction and the carbon concentration.

4.2.2 Characterization of microstructure after reheating to 700 °C

In §4.1.3, the microstructure of samples with a QT of 160, 260 and 320 °C was analyzed. A microstructural characterization of the same selection of samples after reheating to 700 °C will be discussed in this paragraph.

4.2.2.1 Analysis of sample QT160 H700

Figure 4.10a and Figure 4.10a show EBSD phase maps of sample QT160H700 after reheating. Almost no RA is observed, even though the fraction of retained austenite f_γ has increased compared to sample QT160 (*c.f.* Figure 4.4a). Approximately 50% of the pixels could be indexed. Even regions with seemingly high band contrast were not indexed. This suggests that the quality of the generated Kikuchi patterns was low, indicating a bad measurement. Due to practical limitations, this measurement was not redone.

Figure 4.10c and Figure 4.10d show SEM micrographs of sample QT160H700. Carbides and some film-type RA can be observed in Figure 4.10d. Compared to sample QT160, the carbides have coarsened (*c.f.* Figure 4.4). Furthermore, as later shown in Figure 4.14, some precipitation of carbides from martensite has occurred.

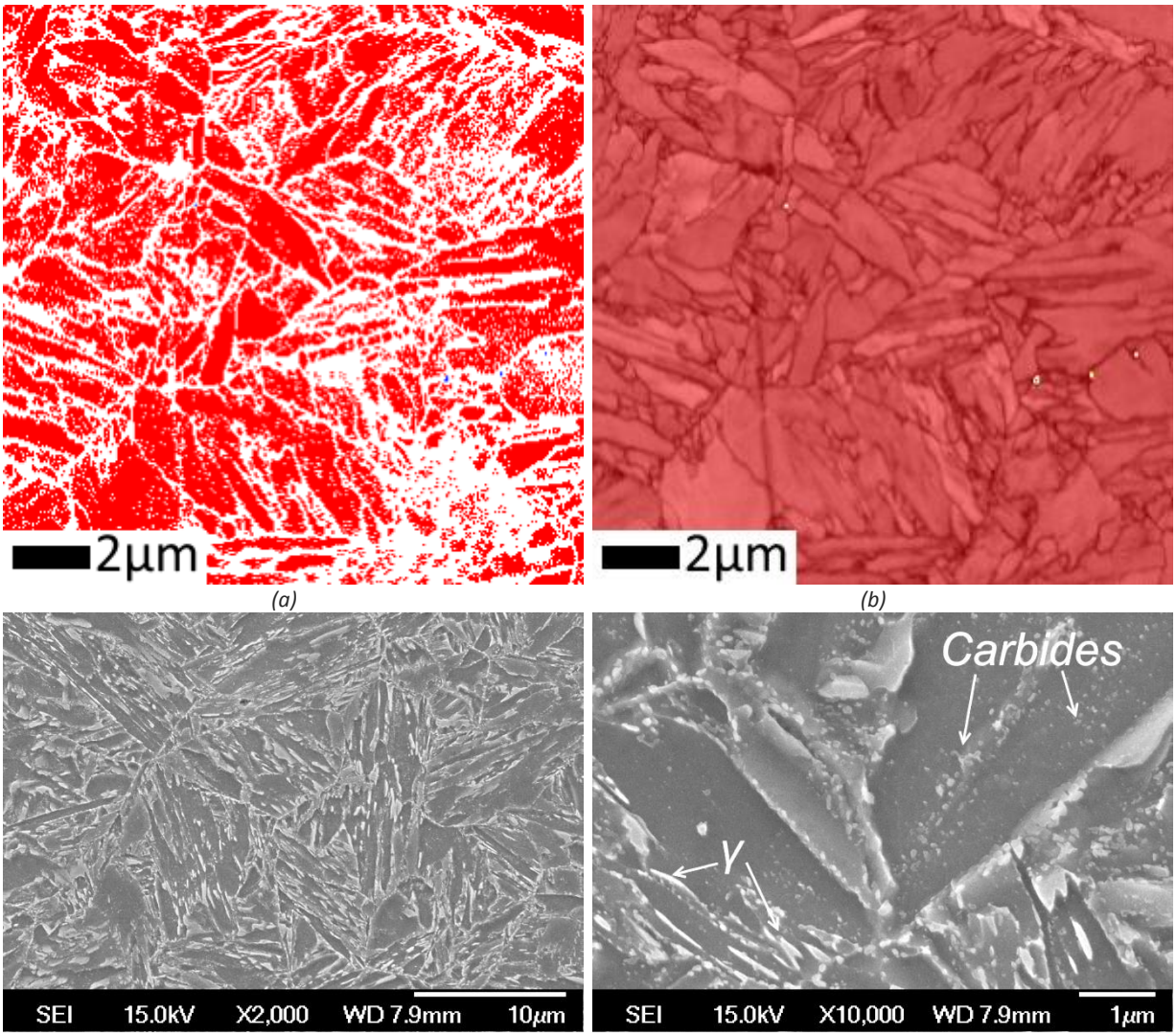

(a) *(b)* *(c)* *(d)*

Figure 4.10: Microstructure of sample QT160H700. (a) Phase map before cleaning. BCC is shown in red, FCC in blue. (b) Combined EBSD band contrast and phase map. Cleaned version. (c) (d) SEM micrograph.

4.2.2.2 Analysis of sample QT260H700

Figure 4.11a and Figure 4.11b show EBSD phase maps of sample QT260H700 after reheating. Similar to sample QT160H700 in Figure 4.10, almost no retained austenite (<0.1%) is observed. However, approximately 70% of the pixels could be indexed, indicating good Kikuchi patterns. According to the analysis in §4.2.1, this sample contains a phase fraction of retained of approximately 0.09. This suggests that the retained austenite exists in regions which could not be indexed. This could be due to either a small retained austenite grain size, or the effect of the reheating on the grain boundaries and surroundings of retained austenite. For example, some cementite could have precipitated in the grain boundaries of retained austenite, giving low band contrast.

Figure 4.11c and Figure 4.11d show SEM micrographs of sample QT260H700. Coarse carbides and some film-type RA can be observed in Figure 4.11d. The martensite from the second quench (M2) will be carbon depleted due to precipitation of carbides. Features which do not etch in nital are therefore either carbides or austenite. Large unetched features should be large retained austenite grains. However, due to lack of EBSD indexing, this cannot be said with complete certainty. The features indicated with γ? In Figure 4.11d could be large RA grains.

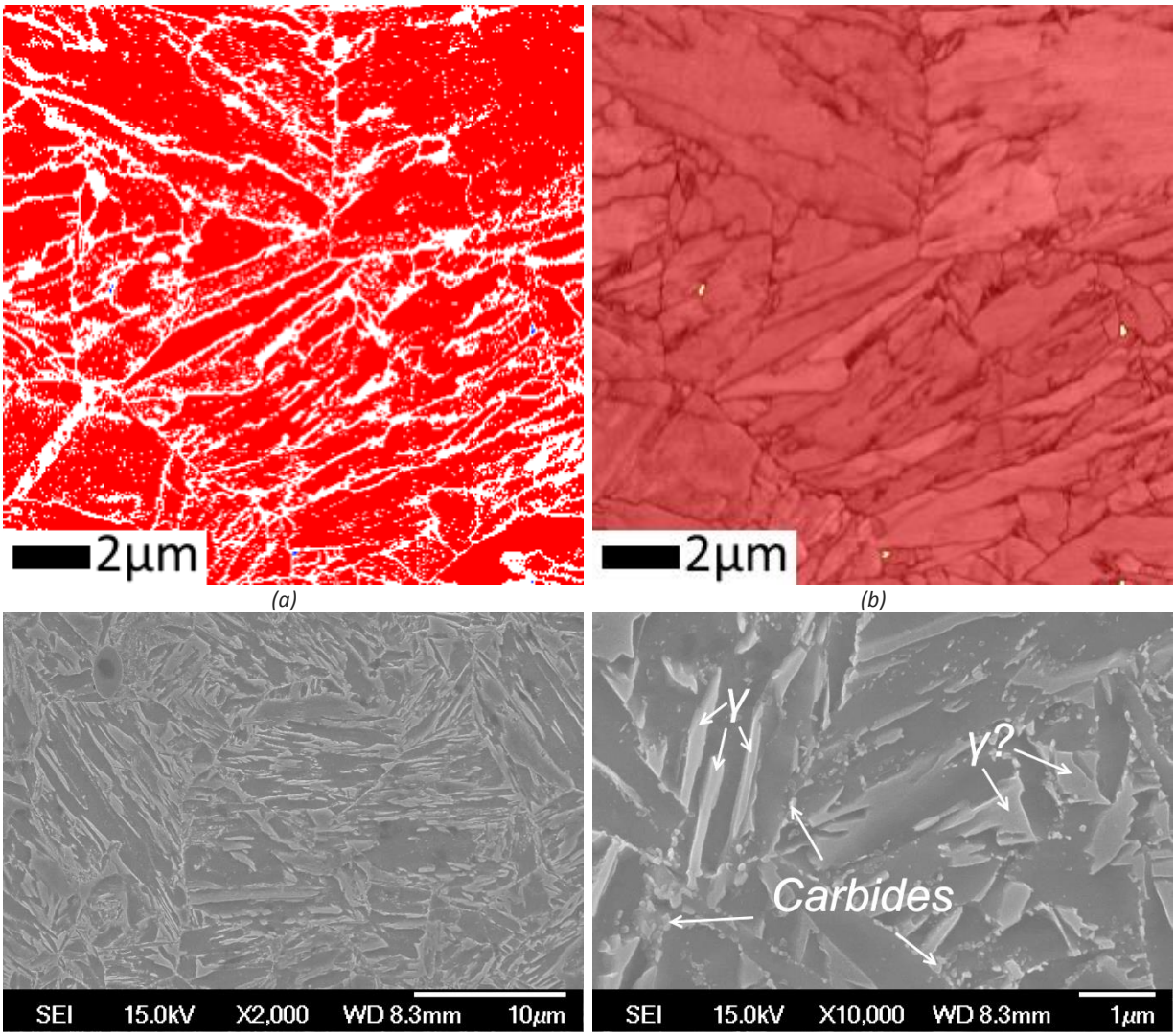

(a) *(b)*

(c) *(d)*

Figure 4.11: Microstructure of sample QT260H700. (a) Phase map before cleaning. BCC is shown in red, FCC in blue. (b) Combined EBSD band contrast and phase map. Cleaned version. (c) (d) SEM micrograph.

4.2.2.3 Analysis of sample QT320H700

Figure 4.12 a and Figure 4.12b show EBSD phase maps of sample QT320H700 after reheating. Similar to Figure 4.10a and Figure 4.11a, almost no RA is observed. Approximately 70% of the pixels could be indexed, again indicating good quality of the Kikuchi patterns.

Figure 4.12c and Figure 4.12d show typical SEM micrographs of sample QT320H700. Coarse carbides and some film-like RA can be seen.

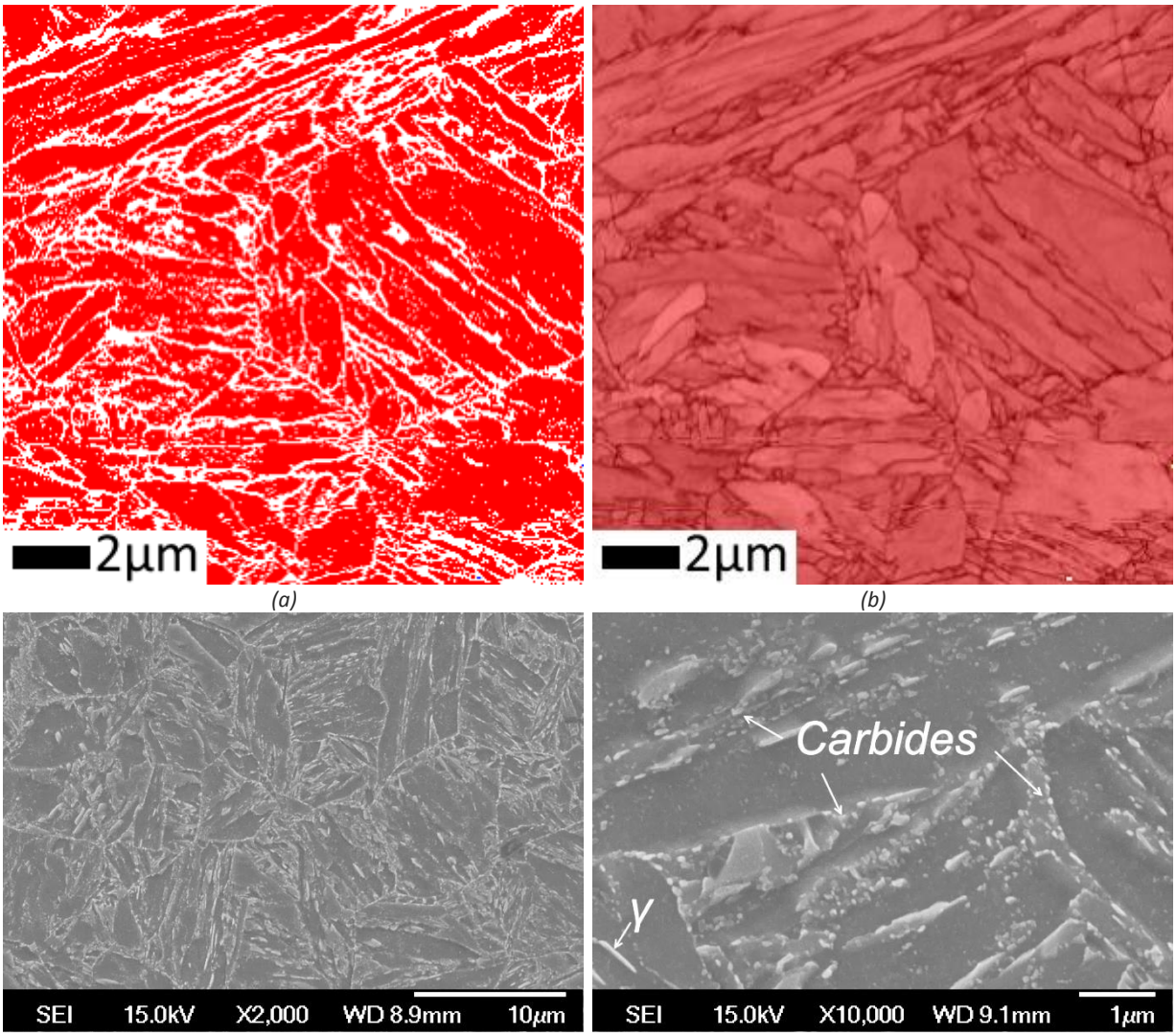

(a) *(b)*

(c) *(d)*

Figure 4.12: Microstructure of sample QT320H700. (a) Phase map before cleaning. BCC is shown in red, FCC in blue. (b) Combined EBSD band contrast and phase map. Cleaned version. (c) (d) SEM micrograph.

4.2.3 Short summary of quantification and identification of reheated samples

Table 4.2: Summary of properties of samples after reheating

Sample	QT160H700	QT260H700	QT320H700
Volume fraction of retained austenite f_γ	0.06 ± 0.01	0.09 ± 0.005	0.05 ± 0.005
Increase or decrease in f_γ after reheating	Increased by 0.02	Decreased by 0.06	Increased by 0.01
Carbon content in retained austenite (wt. %)	1.11 ± 0.05	1.035 ± 0.05	1.15 ± 0.05
Carbides	Yes, coarse carbides	Yes, coarse carbides	Yes, coarse carbides

Table 4.2 summarizes selected properties of the analyzed reheated samples. In the EBSD scans, no or very little A observed. As observed in SEM micrographs, retained austenite exists in large enough grain sizes to be retained austenite detectable by EBSD after reheating. It is speculated that the absence of retained austenite in EBSD scans is due to low band contrast due to the presence of carbides close to retained austenite.

Figure 4.13 shows the XRD spectrum of the selected samples reheated to 700°C. Compared with Figure 4.7, RA peaks have sharpened, and ferrite peaks are sharper as well. This is most likely due to reduction of stresses due to annealing of the samples. Furthermore, the distribution of carbon in the austenite will change, also causing some peak sharpening.

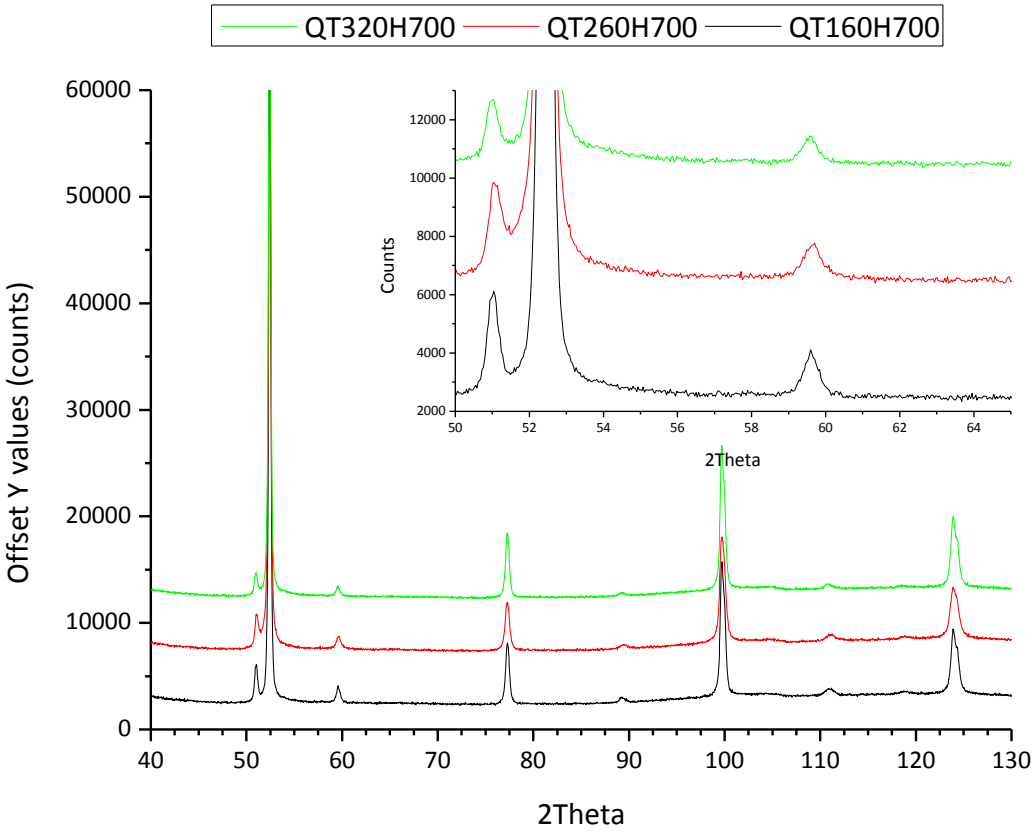

Figure 4.13: XRD spectrum of reheated samples. The applied offset values are +4000 for sample QT260H700 and +8000 for sample QT320H700. The inset shows the {111} and {200} peaks of austenite in further detail.

4.2.4 In which temperature region does retained austenite decompose during reheating with 5 °C s^{-1}?

Figure 4.14 shows the derivative of dilatometry curves of selected samples during reheating to 700 °C. Furthermore, a sample was quenched to room temperature with 200 °C s^{-1} after identical austenitization and reheated to 700 °C. It is shown as a comparison in Figure 4.14. A decrease in the derivative around 680 to 690°C means that growth of austenite is occurring in samples QT160H700 and QT320H700. Growth of austenite is possible at temperatures above A1, which in QP-G is around 625-650 °C. A decrease in the derivative is not observed in the quenched sample and sample QT260H700. Significant growth of austenite is therefore not occurring in these samples.

Around 500 °C, the quenched sample and samples QT320H700 and QT160H700 show a relative contraction, which can be related to precipitation of carbides from martensite. Sample QT260H700 however, does not show the same degree of contraction. Precipitation of carbides from martensite has an opposite effect on length change compared to austenite decomposition. It is hypothesized that around 500 °C, RA starts to decompose in sample QT260H700. The increase in length due to RA decomposition will then partially compensate the length decrease due to precipitation of carbides from martensite.

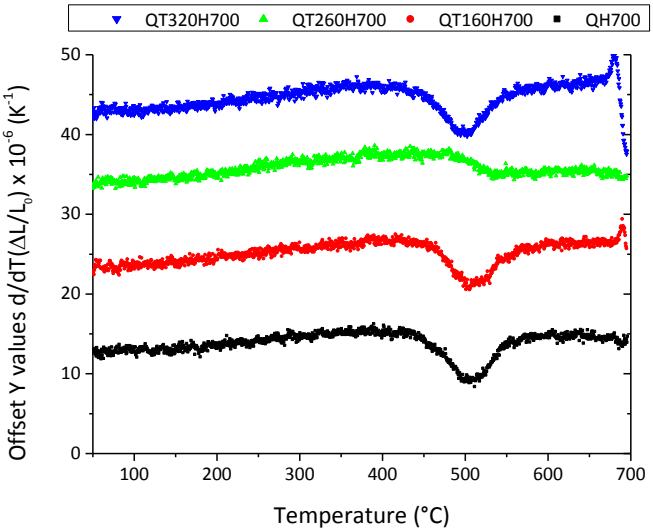

Figure 4.14: Derivative of dilatometry curves of selected samples during reheating. Also included is a quenched sample, reheated to 700 °C with a heating rate of 5 °C s^{-1} as well.

To test this hypothesis, samples with a QT of 260 °C and 160 °C were reheated to 300, 400, 500 and 600 °C with 5 °C s^{-1} and directly quenched to room temperature upon reaching these temperatures. Figure 4.15 shows f_γ as measured with the VSM of these samples, with the original samples shown as a comparison. Two trend lines are drawn to indicate the possible trends of f_γ versus temperature.

Figure 4.15 shows that only samples QT260H600 and QT260H700 show significant decomposition of RA. With a heating rate 5 °C s^{-1}, decomposition of RA in samples with a QT of 260 °C is therefore occurring above 500 °C, but not occurring between 25 and 500 °C. Samples with a QT of 160 °C show no significant decomposition up to 600 °C, indicating that RA is more stable in these samples. During reheating with 5 °C s^{-1}, decomposition of retained austenite therefore starts around 500 °C in samples with a QT of 260 °C, confirming the hypothesis.

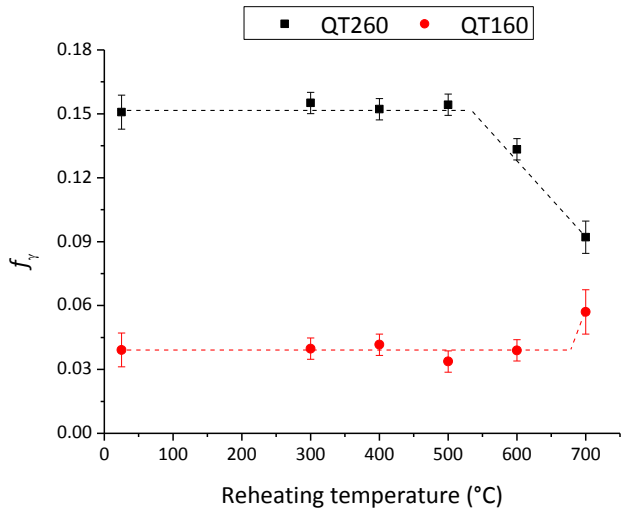

Figure 4.15: Phase fractions as measured with VSM of samples with QT160 and QT260 reheated to indicated temperatures with 5 °C s^{-1}.

4.3 Influence of carbon content in retained austenite on its decomposition

As discussed in §4.2, no retained austenite decomposition was detected in sample QT160 during reheating with 5 °C s^{-1} to 700 °C. However, significant retained austenite decomposition was detected in sample QT260. As discussed in §4.1, the carbon content of RA in sample QT160 was about 1.15 wt. % and the carbon content in sample QT260 was about 1.02% wt. It is hypothesized that the difference in carbon content could cause the different observed decomposition behavior.

To study the influence of carbon content, samples with quenching temperatures of 160 °, 260 °C and 320 °C were heated to 600 °C instead of 700 °C. This temperature was chosen to prevent the increase in retained austenite fraction observed in §4.2.4. The reheating rate was set at 5 °C min^{-1}, 10 °C min^{-1} and 15 °C min^{-1} in the dilatometer. These reheating rates were selected based on literature [11], [26], to establish activation energies of RA decomposition.

Furthermore, a sample with a QT of 260 °C was reheated to 600 °C with 5 °C min^{-1} in the VSM. This QT was selected based on its highest observed retained austenite fraction. The VSM was used to accurately determine the phase fraction retained austenite during heating. The resulting phase fraction was then correlated with the dilatometry curve of the corresponding reheated sample.

4.3.1 Dilatometric and magnetic measurements

In Figure 4.16, the retained austenite fraction of a sample with a QT of 260 °C as determined with VSM during reheating is shown in red. The thermal expansion coefficient measured with the dilatometer is shown in black. As indicated in Figure 4.16, four distinct regions of decomposition behavior are observed based on the VSM results:

A) No decomposition of RA (RT – 250 ° C): Negligible change in phase fraction of retained austenite.
B) Decomposition of RA (250 °C – 370 °C): The phase fraction of retained austenite decreases by 0.04 according to VSM. The relative length change due to decomposition of RA was determined to be 0.025% using Equation 3.12. A relative length change of 0.025% correlates to decomposition of a phase fraction of about 0.04 RA[3]. The decomposed RA phase fractions as determined with VSM and dilatometer are in agreement.
C) No decomposition of RA (370 °C – 500 °C): Negligible change in the phase fraction of retained austenite. In the dilatometry curve precipitation of carbides from martensite is observed.
D) Decomposition of RA (500 °C – 600 °C): The phase fraction of retained austenite decreases by 0.04 as determined with the VSM. No corresponding increase in volume could be determined. The expected length change due to decomposition of a fraction of 0.04 RA is 0.016%. It is likely that the volume decrease due to precipitation of carbides from martensite is partially compensating the volume increase due to RA decomposition. Furthermore, relief of stresses originating from the Q&P treatment could also occur. These explanations are explored in further detail in Appendix B.

[3] Calculated using methods described in §3.2.5 under the assumption that RA contains 1 wt. % C. The average length change of RA decomposition between 250 °C – 370 °C was used (c.f. Figure 3.7a).

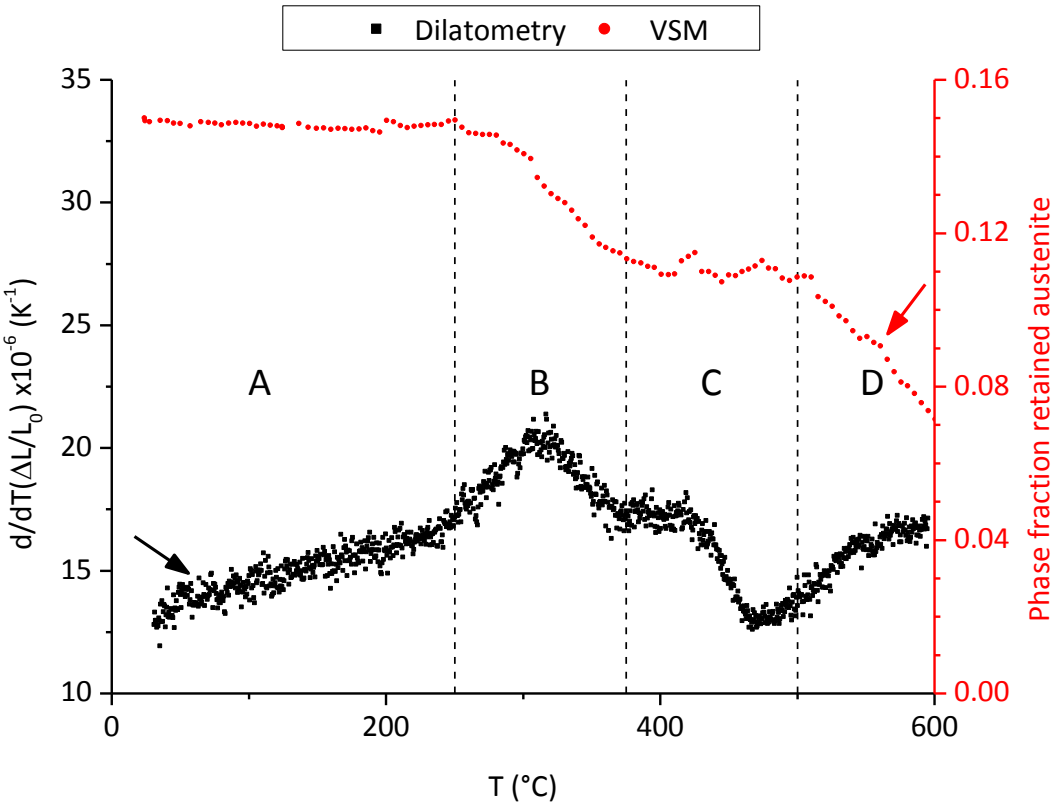

Figure 4.16: Thermal expansion as measured with dilatometer and phase fraction of RA measured with the VSM during reheating to 600 °C. The heating rate was 5 °C min^{-1} in both cases. Four distinct regions of RA decomposition behavior are indicated.

Based on these observations, it was concluded that the dilatometer does not allow observation of RA decomposition during precipitation of carbides from martensite. In this work, precipitation of carbides from martensite was found to start between 400 °C and 420 °C. The dilatometer allows observation of the length change from RA decomposition below that temperature. Keeping this in mind, the dilatometry curves of samples with QT160, QT260 and QT320 during reheating to 600 °C with varying heating rates were analyzed. The thermal expansion during reheating is shown in Figure 4.17a for QT260, Figure 4.17b for QT160 and Figure 4.17c for QT320.

For samples with a QT of 260 °C, the length changes due to RA decomposition are observed in Figure 4.17a. The relative length change observed, *i.e.* the peak area, decreases with increasing heating rate. The peak position shifts to higher temperatures, *i.e.* decomposition starts at higher temperatures with increasing heating rate. Based on this peak position shift, the activation energy for RA decomposition into ferrite and carbides in QT260 samples is determined[4] as 126 ± 15 kJ mol^{-1}, as shown in the Kissinger plot in Figure 4.17d. This value is comparable to values found in literature for retained austenite decomposition (132 kJ mol^{-1} in [26], 113-174 kJ mol^{-1} in [62]. These activation energies are typical for either carbon diffusion in austenite or pipe diffusion of iron in ferrite [26].

For samples with a QT of 160 °C, length changes due to RA decomposition are not observed in Figure 4.17b. Decomposition of RA is not occurring.

[4] Based on methods described in §3.2.6.

For samples with a QT of 320 °C, small length changes due to retained austenite decomposition are observed in Figure 4.17c. Decomposition of RA again starts at higher temperature with increasing heating rate. Based on the position of the peaks, the activation energy is determined to be 128 ± 15 kJ mol^{-1}, as shown in the Kissinger plot in Figure 4.17d. This activation energy is similar to the activation energy of retained austenite decomposition observed for QT260 samples.

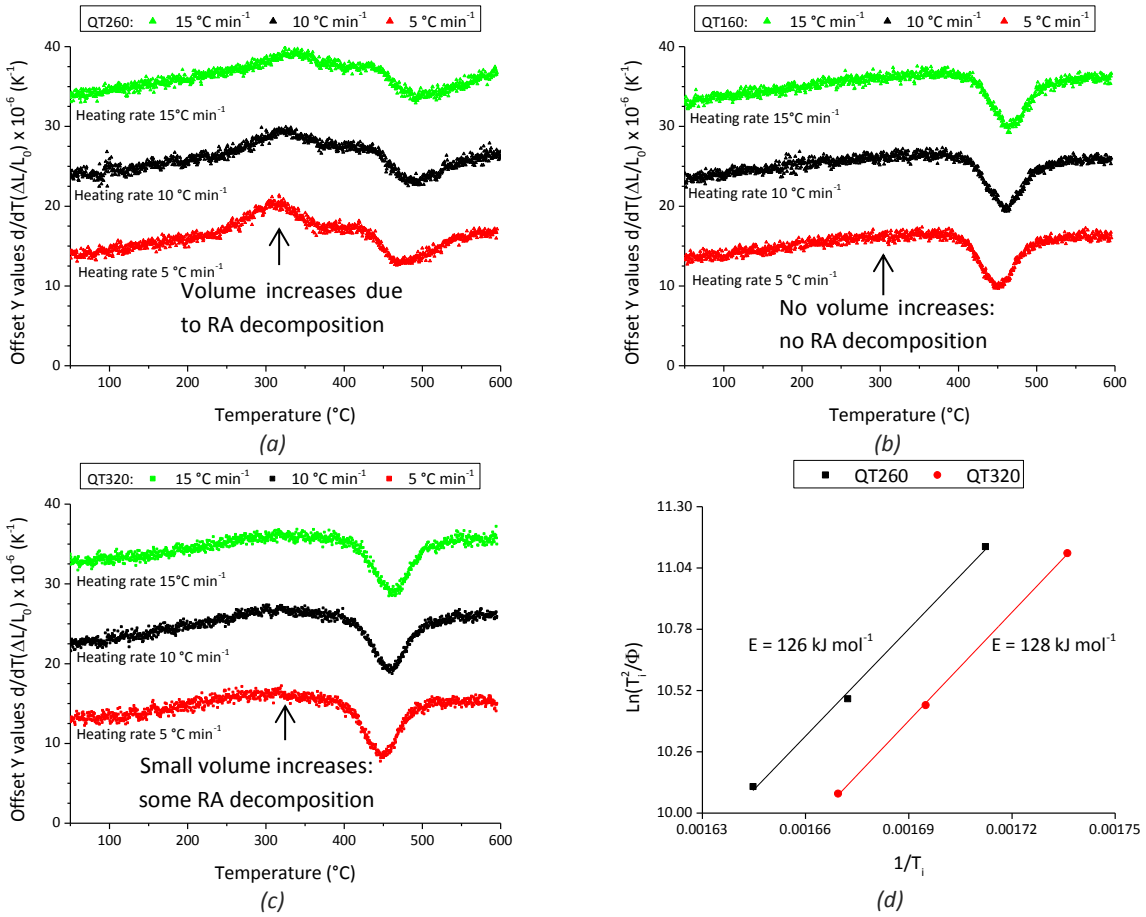

Figure 4.17: Derivative curves of samples with different heating rates. (a) Samples with QT260 (b) Samples with QT160 (c) samples with QT320 with different heating rates. The applied offset in all of these figures is +10x10^{-6} for a heating rate of 10 °C min^{-1} and +20x10^{-6} for a heating rate of 15 °C min^{-1}.(d) Kissinger plot for the determination of activation energies for the decomposition of retained austenite in samples with the indicated quenching temperatures.

In summary, retained austenite decomposition below 400 °C was absent in QT160 samples, while it was observed in QT260 and QT320 samples. The decomposition of RA is heating rate dependent, and its activation energy in QP-G is approximately 127 kJ mol^{-1}. Carbon diffusion in austenite or pipe diffusion of iron in ferrite are possible rate controlling factors for the decomposition of retained austenite.

The main difference between QT160, QT260 and QT320 samples is the carbon concentration in the RA. In QT160 the carbon content in RA is 1.15 wt. % C, in QT260 it is 1.02 wt. % C and in QT320 it is 1.07 wt.% C. This is an indication that higher carbon content in RA could stabilize retained austenite against decomposition below 400 °C.

4.3.2 Characterization of decomposition products of RA

If higher carbon content stabilizes the retained austenite against decomposition, the retained austenite that decomposes earliest should have relatively low carbon content. As found in §4.3.1, a

phase fraction retained austenite of 0.04 decomposed up to 500 °C during 5 °C min^{-1} reheating of a QT260 sample. This decomposed phase fraction is hypothesized to have lower carbon concentration compared to the non-decomposed phase fraction.

To characterize the decomposed phase fraction, a sample with a QT of 260 °C was reheated to 425°C at 5 °C min^{-1}. A phase fraction of 0.04 is assumed to decompose during the annealing. As observed in Figure 4.16, 425 °C is a temperature slightly below the start of precipitation of carbides from martensite. The martensitic microstructure will therefore not be strongly tempered. This will limit the fraction of carbides precipitated from martensite and their growth. Microstructures containing carbides formed during the decomposition of RA will therefore be more easily detectable [19].

After annealing to 425 °C and quenching, the phase fraction of RA was found to be 0.11. The decomposition of a phase fraction of 0.04 has occurred, in line with expectations. Figure 4.18a shows an EBSD phase map and of the microstructure of this sample (QT260H425). Note that the EBSD scan in Figure 4.18a has been performed with a smaller step size of 30 nm and smaller area compared to previously shown EBSD scans. An identification rate of 80% was achieved using EBSD, and RA grains were not significantly affected due to the cleaning. The morphology of the RA has a clear distribution of grain sizes, ranging from just detectable at 30 nm to approximately 500 nm wide grains.

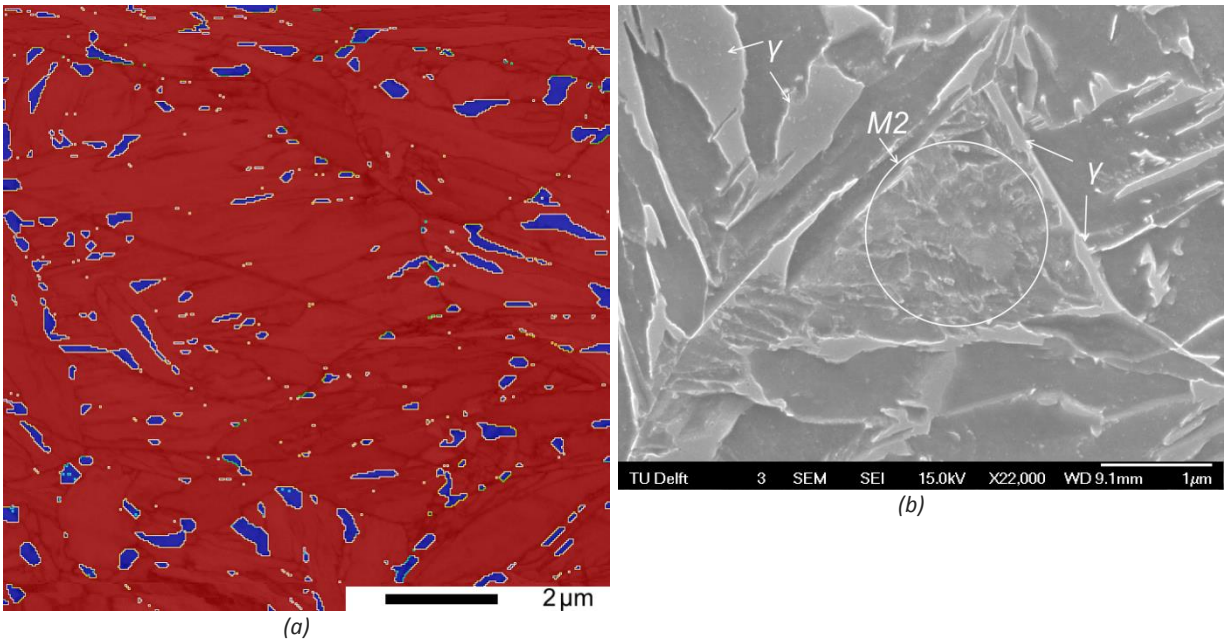

(a) *(b)*

Figure 4.18: (a) EBSD Phase map of sample QT260H425. BCC is shown in red, FCC in blue. The black scale bar represents 2 µm. (b) Tempered M2 encircled in white.

Figure 4.18b is a SEM micrograph of sample QT260H425. The micrograph shows retained austenite films approximately 100 nm wide and a few µm long. Figure 4.18b shows larger RA grains of 0.5 µm thick as well. Furthermore, Figure 4.18b shows a large tempered M2 grain, with retained austenite at its edges.

A search for indications of decomposition of retained austenite using all available SEM micrographs of sample QT260 and sample QT260H425 yielded no clear results. Although regions of M2 were clearly tempered, no regions were found which could only be the results of retained austenite decomposition. In the author's opinion, other methods than SEM and EBSD are needed for characterization of retained austenite decomposition products in this sample.

4.3.3 Study at longer annealing times

Four different temperature regions of decomposition behavior were observed in §4.3.1. In temperature regions B, C and D the following was observed:

B) 250 – 370 °C: decomposition of retained austenite
C) 370 – 500 °C: stagnant stage
D) 500 – 600 °C: decomposition of retained austenite

However, the mechanisms of decomposition in these regions are unknown. To study the mechanisms of decomposition in each of these temperature regions 30 minutes of isothermal annealing was performed in a dilatometer. Samples with a QT of 260 °C were used. The selected isothermal annealing temperatures were 350 °C for region B, 450 °C for region C and 550 °C for region D.

The heating rate to the isothermal holding temperature was 5 °C s^{-1}. Due to the relatively high heating rate, a thermal gradient will exist in the sample, with the center being warmer than the edges. Upon reaching the holding temperature, this thermal gradient will gradually decrease, causing an increase in length in the sample. The length change due to reduction of the thermal gradient is determined as approximately +0.01% to +0.015%, and is unchanging after approximately 250 s of holding.

The normalized length change during the annealing is shown in Figure 4.19a. The same figure also shows the retained austenite fraction as determined with magnetic methods after quenching to room temperature. Figure 4.19b shows the normalized length change during the quench after annealing.

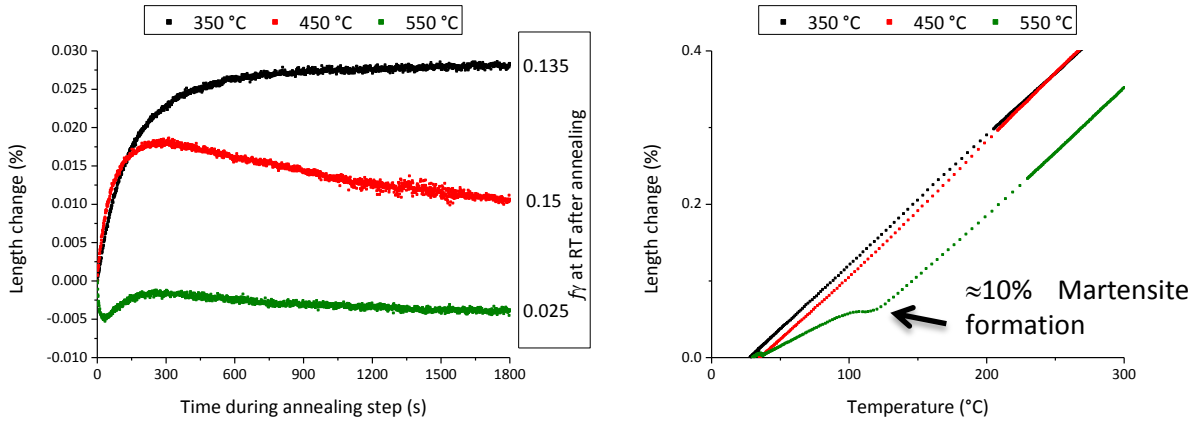

Figure 4.19: (a) Length change during 1800s isothermal holding at the indicated temperatures for samples with a QT of 260 °C. The phase fraction of RA after quenching to room temperature is indicated. (b) Length change during the quench after isothermal holding. The arrow indicates martensite formation during the quench from an isothermal holding temperature of 550 °C. The Ms is approximately 125 °C, indicating a carbon content of around 0.74% in the transforming austenite using equations by van Bohemen [28].

For an annealing and holding temperature of 350 °C, a length change of 0.025% is observed. After subtraction of the determined length change due to the reduction in thermal gradient, a net length change of approximately 0.010% is determined. This length change can be correlated to decomposition of an austenite fraction of approximately 0.015. No significant amount of carbides is thought to have precipitated from martensite. After quenching to RT, the phase fraction of retained austenite f_γ is measured by VSM as 0.135. Since f_γ in Q&P samples with a QT of 260 °C was 0.15, the

decomposed fraction as measured by VSM after quenching and the decomposed fraction of f_γ measured by dilatometry match.

The length change curve of isothermal holding at 350 °C gives some indications on the kinetics of decomposition. The rate of length increase is seen to gradually slow during the annealing. This suggests initial fast decomposition of retained austenite upon reaching 350 °C, followed by a gradual slowing down of decomposition.

For an isothermal holding temperature of 450 °C, a net length change of -0.005% is determined during holding. This net reduction of the length is due to precipitation of carbides from martensite. No significant increase in length can be detected. This means that no significant decomposition of retained austenite is occurring during the isothermal holding. Another possibility is that the negative length change of precipitation of carbides from martensite is compensating the positive length change of decomposition of retained austenite. After quenching to RT, f_γ was measured as 0.15, which is the same fraction as the untreated sample QT260. This confirms that no detectable decomposition has occurred.

For an isothermal holding temperature of 550 °C, a net length change of -0.02% is determined during holding. This net length decrease most likely consists of two parts:

- Length decrease due to stress relief, as explored in further detail in Appendix B.
- Length decrease due to precipitation of carbides from martensite. This is most likely less significant than length decrease due to stress relief. Figure 4.14 shows that the process of carbide precipitation has almost finished at 550 °C.

No length increases due to decomposition of RA are observed during the holding. However, during the quench to room temperature from 550 °C after isothermal holding, formation of martensite is occurring. A martensitic phase fraction of ≈0.1 is formed, with an Ms of ≈125 °C. The carbon content in the transforming austenite was determined as 0.74 wt. % C, using equations by van Bohemen [28]. Samples with a QT of 260 °C without annealing have an average carbon concentration in RA of 1.02 wt. % C. This means that the carbon concentration in RA reduces by approximately 0.3 wt. % C in 30 minutes. This carbon is most likely precipitated into cementite or alloy carbides, but this was not investigated in further detail. Podder *et al.* [19] encountered this phenomenon as well at lower isothermal holding temperatures of 450 °C. They observed minute quantities of cementite precipitating around austenite. The local reduction in carbon concentration destabilized the retained austenite against the martensitic transformation upon quenching.

4.4 Effect of partitioning time on thermal stability of retained austenite

The effect of partitioning time on the thermal stability of retained austenite was studied by varying the partitioning time of Q&P samples with a QT of 260 °C. This QT was selected based on its highest observed retained austenite fraction. The partitioning time was increased from 50 seconds to 300 and 600 seconds, while the rest of the Q&P treatment was unchanged. A sample with a partitioning time t_p of 300 s was reheated to 600 °C with a heating rate of 5 °C min^{-1} in the VSM. The dilatometer was used to reheat the sample with a t_p of 600 s to 600 °C with a heating rate of 5 °C min^{-1}.

Figure 4.20 shows the fraction of retained austenite as determined using the VSM. A slight increase of f_γ with increasing partitioning time up to 600 s was measured.

Figure 4.20b shows the thermal expansion coefficient during reheating to 600 °C in the dilatometer. The standard sample with a t_p of 50 s is treated in further detail in §4.3. The absence of a clear peak in the sample with a t_p of 600 s means that no detectable retained austenite decomposition is occurring in the temperature range 250 °C to 370 °C. The longer partitioning time has stabilized the retained austenite.

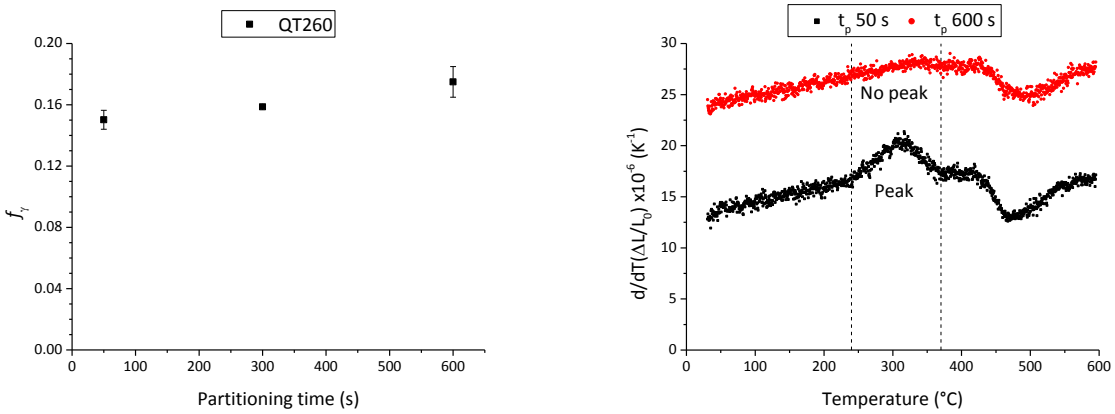

Figure 4.20: (a) Fraction of RA as a function of partitioning time in samples with a QT of 260 °C. (b) Thermal expansion coefficient during reheating to 600 °C in the dilatometer. The offset applied is +10^{-5} for the sample with a t_p of 600 s.

Confirmation of the absence of retained austenite decomposition is found by thermomagnetic methods. The retained austenite fraction during reheating to 600 °C as measured in the VSM is plotted in Figure 4.21. The standard sample with a t_p of 50 s is treated in further detail in §4.3.

The sample with a t_p of 300 s shows an approximately constant fraction of retained austenite up to 500 °C. A slight decrease (0.003) in the phase fraction can be seen in the temperature range from 400 °C to 500°C. In the temperature range of 500 °C to 600 °C, the phase fraction shows a stronger decrease of about 0.04.

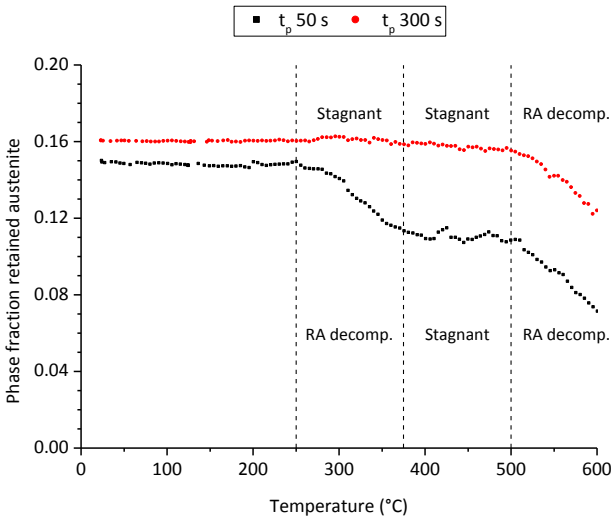

Figure 4.21: Phase fraction of retained austenite during reheating to 600 °C in the VSM.

As shown in Figure 4.20 and Figure 4.21, in samples with increased partitioning times of 300 to 600 s, retained austenite is more stable against decomposition into ferrites and carbides. This statement is especially true in the temperature region below 400 °C. A theory based on carbon homogenization during partitioning will now be proposed to explain this increase in stability.

4.4.1 Carbon homogenization during partitioning

Mecozzi *et al*. [59] simulated the carbon concentration in residual austenite during partitioning. A phase field model was used to model a (0.25C-3Mn-1.5Si) steel alloy. Figure 4.22 shows the carbon concentration in retained austenite at partitioning times of 50 s (Figure 4.22a) and 300 s (Figure 4.22b). Figure 4.22c shows a phase map, with ferrite yellow, and austenite all other colors. These figures are intermediate results of that paper, courtesy of Pina Mecozzi.

As shown in Figure 4.22a, after a partitioning time of 50 s the carbon is mostly concentrated at the edges of residual austenite grains. In contrast, after a partitioning time of 300 s the carbon has diffused into these grains. This has led to a homogenization of the carbon concentration gradient. Figure 4.22d shows a carbon profile along the line A-B of the selected grain for different partitioning times, illustrating the effect of homogenization. A partitioning time of 300s decreases the carbon concentration at the α/γ interface, while the carbon concentration in the grain is somewhat higher.

Schematic profiles of the carbon concentration in a retained austenite grain are shown in Figure 4.23. The carbon profile after a Pt of 50 s is shown in Figure 4.23a, while Figure 4.23b shows the carbon profile after a Pt of 300 s. The carbon content necessary to prevent martensitic transformation during quenching is indicated with Ms. As discussed in §4.3, retained austenite with relatively low carbon content decomposes during annealing up to 400 °C. Retained austenite with relatively high carbon content does not decompose. Indicated with C_{bf} is the hypothesized carbon content necessary to prevent retained austenite decomposition during annealing up to 400 °C.

As shown in Figure 4.23a, after 50 s partitioning part of the retained austenite will have a carbon concentration below C_{bf}. Part of the RA is able to decompose during annealing. A partitioning time of 300 s however, homogenizes the entire grain to a carbon concentration above C_{bf}. No retained austenite will therefore be able to decompose during annealing.

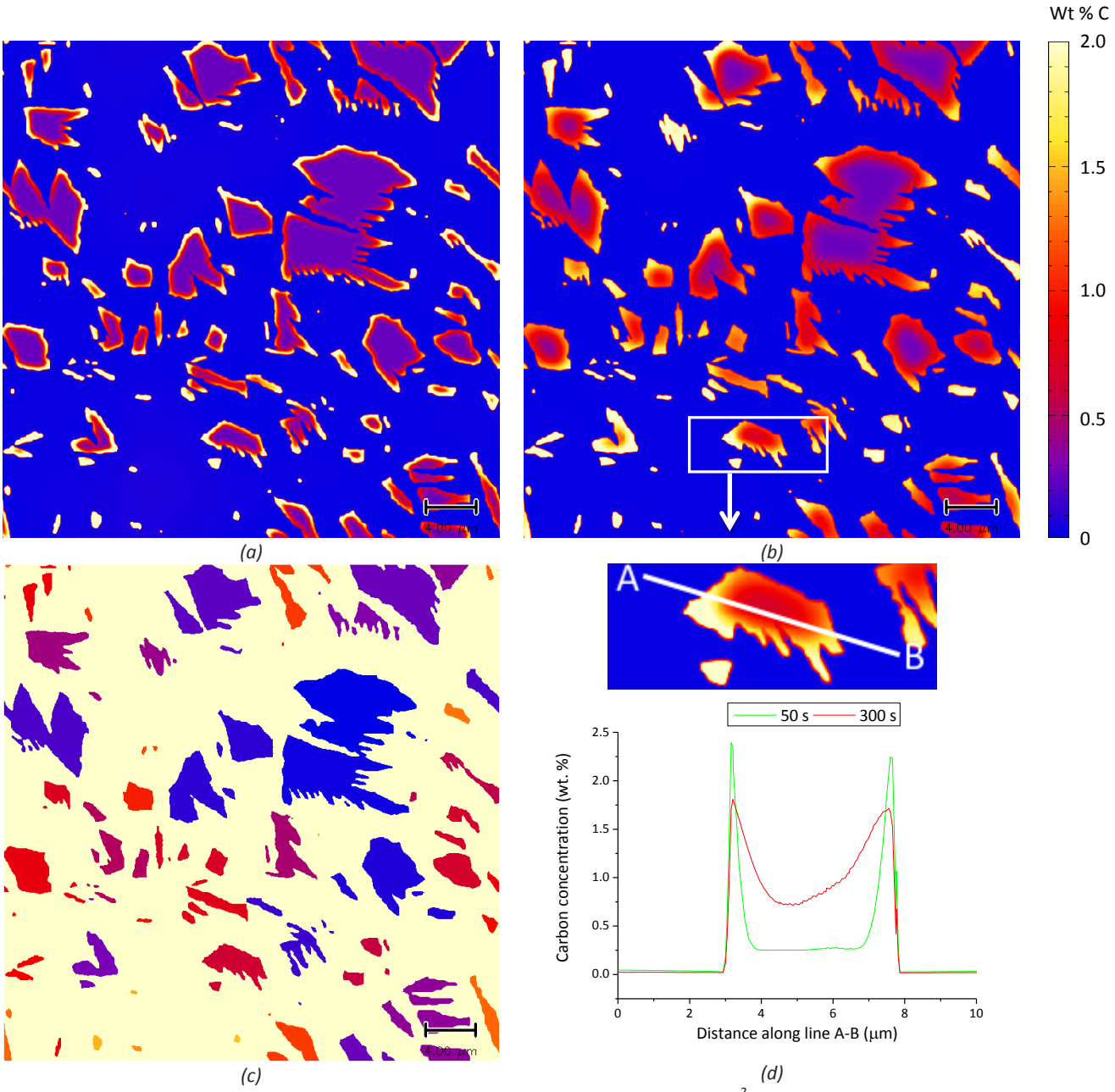

Figure 4.22: (a) Carbon concentration in RA grains, Pt = 50s, QT = 243 °C, size 40x40 µm^2. (b) Carbon concentration in RA grains, Pt = 300s, QT = 243 °C, size 40x40 µm^2. (c) Phase map. Ferrite shown in light yellow. (d) Carbon profile along the line A-B of the selected grain with different partitioning times. All the data in these figures are courtesy of Pina Mecozzi

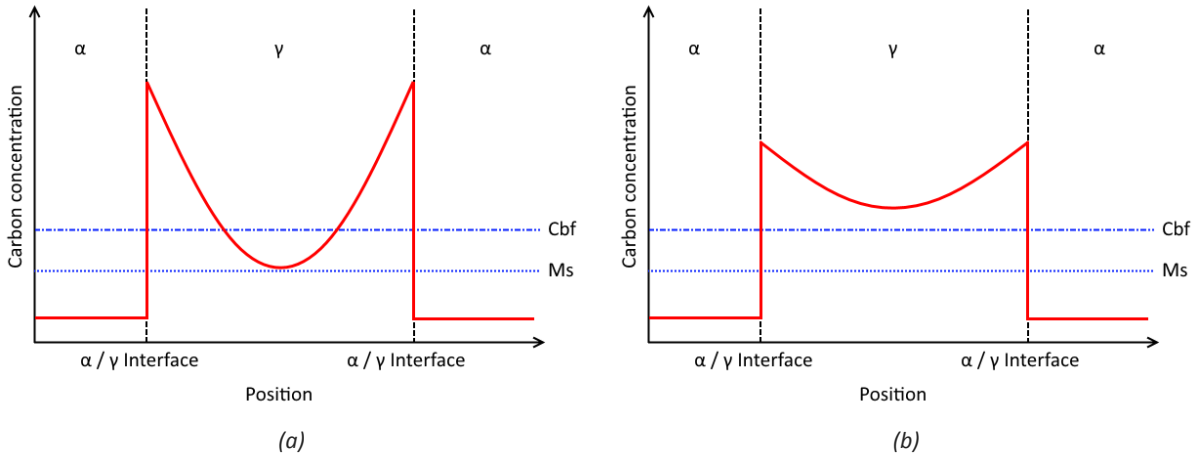

Figure 4.23: Schematic carbon profile in a retained austenite grain after different partitioning times. (a) t_p 50 s. (b) t_p 300 s.

During reheating with 5 °C min^{-1} to temperatures above 500 °C, no effect of homogenization on the kinetics of RA decomposition is detected as seen in Figure 4.21. However, increasing the partitioning time up to 600 s still stabilizes the RA below 500 °C, leading to a higher RA fraction at this temperature during reheating.

It is possible that carbon diffusion during reheating has homogenized the carbon profile in the sample with 50 s partitioning time as well. This homogenization could nullify any effects of longer partitioning time on RA decomposition. A simple model has been applied to calculate the total diffusion distance of carbon during reheating at 5 °C min^{-1}. Its results are shown in Figure 4.24.

The model consists of numerical integration of the equation $x = \sqrt{Dt}$, with x the diffusion distance, D the diffusion coefficient and t the time. The total diffusion distance is then $\sum x_i$, where x_i is the diffusion distance at temperature i. The temperature step was 1 °C. For a heating with 5 °C s^{-1}, x was calculated by setting $t = 12$ s and using $D = D_0 exp^{(-\frac{Q_d}{RT})}$. For austenite, $D_0 = 1.5 * 10^{-5}$ m^2 s^{-1} and $Q_d = 142.1$ kJ mol^{-1} were used [59]. For ferrite, $D_0 = 1.1 * 10^{-6}$ m^2 s^{-1} and $Q_d = 87.4$ kJ mol^{-1} were used [45].

Indicated in Figure 4.24 is the extra diffusion distance achieved in 250 s longer partitioning time, calculated with the same model. The carbon diffusion distance up to 500 °C during reheating is significantly larger than that achieved during partitioning.

Homogenization of carbon during reheating with 5 °C min^{-1} is therefore unlikely to affect the kinetics of RA decomposition at temperatures higher than 500 °C. Furthermore, homogenization of carbon during reheating with 5 °C min^{-1} is hypothesized to play no significant role during reheating up to 300 °C. Homogenization during reheating would stabilize the low carbon RA against bainitic decomposition, but is not experimentally seen. This is because the diffusion distance is thought too low for carbon to diffuse from high concentration RA to low concentration RA during reheating.

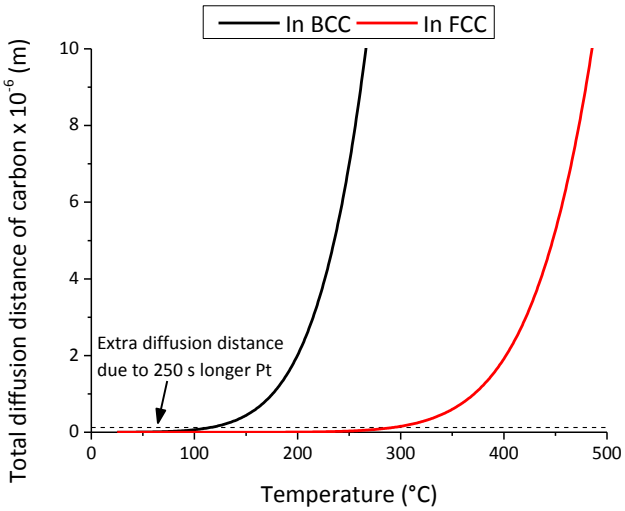

Figure 4.24: Calculated total diffusion distance of carbon in FCC and BCC during reheating with 5 °C min^{-1}.

4.5 Discussion and theory of observed RA decomposition mechanisms

A summary of the observed decomposition behavior of RA is given. These observations are then linked to known theory about austenite decomposition.

The following has been observed:

There are 4 different temperature regions of decomposition behavior in QP-G. Each of these regions shows different decomposition behavior:

A) 25 °C – 250 ° C: No decomposition of retained austenite
B) 250 °C – 370 °C: Decomposition of retained austenite is possible, depending on carbon content in RA. The mechanism via which the RA decomposes could not be experimentally observed. Low carbon RA decomposes first. After low carbon RA has decomposed, no decomposition of high carbon RA is observed.
C) 370 °C – 500 °C: No significant decomposition of retained austenite observed.
D) 500 °C – 600 °C: Decomposition, excess carbon likely precipitates into carbides from RA. The local reduction in carbon concentration destabilizes the RA, which will transform into martensite upon quenching.

These regions will be treated one by one in the following sections.

Region A: 25 °C – 250 °C

No decomposition of RA has been observed in this region. The reason for this is straightforward: in this temperature range, in essence no diffusion of atoms in austenite is occurring. Displacive decompositions mechanisms are therefore the only kinetically possible transformation mechanisms in this temperature range. Since the austenite is already retained, *i.e.* stable against the martensitic transformation, stability against displacive decomposition mechanisms is implied. Therefore, no decomposition of RA will occur in practically important timescales.

Region B: 250 °C – 370 °C

In this region, low-carbon RA will decompose. High-carbon RA was not found to decompose in the investigated timescales. The exact mechanism of decomposition of low-carbon RA has not been observed. Thermomagnetic measurements (*e.g.* Figure 4.21) show a decrease in f_γ only explainable by formation of BCC iron. Therefore, the decomposition products of low-carbon RA are assumed as γ → α + θ (or other carbides). However, the formation of cementite or other carbides resulting from the decomposition of RA has not been experimentally observed in this work. The lack of any clear carbide formation due to RA decomposition could also be a result of segregation of carbon to dislocations, grain boundaries or other defects.

In a classic paper by Thomas [63], he argues that "There is a serious lack of experimental evidence to document how the transformation of retained austenite is influenced by alloying – whether it transforms to fresh martensite, or bainite ferrite + M_3C or normal ferrite + M_3C". Fresh martensite, bainitic ferrite and normal ferrite are suggested as decomposition products. In this work, the formation of fresh martensite is excluded on the basis that RA is already stable against the martensitic mechanism. This leaves normal ferrite and bainitic ferrite as possible decomposition products. Based on the temperature region of 250 °C – 370 °C in which the decomposition of low-

carbon RA takes place, bainitic ferrite is the most likely decomposition product. This is suggested as well by Honeycombe and Bhadeshia [64, p. 186], who state that "The little available evidence suggests that in the range 230-300°C, retained austenite decomposes to bainitic ferrite and cementite". Bhadeshia [65, p. 12] argues that the formation of bainite consists of formation of supersaturated bainitic ferrite, followed by the precipitation of cementite from the supersaturated ferrite.

A thermodynamic reasoning based on Bhadeshia's arguments helps explain the difference in decomposition behavior between high-carbon and low-carbon RA. Carbon is a strong austenite stabilizer. If decomposition of RA takes place via (bainitic) ferrite formation, high-carbon RA will have a higher thermal stability against decomposition into ferrite. Conversely, high-carbon RA should have lower stability against decomposition into cementite or other carbides, since the driving force for cementite precipitation will be higher.

The driving force for precipitation from RA under paraequilibrium conditions of both ferrite (Figure 4.25a) and cementite (Figure 4.25b) has been modelled using ThermoCalc in QP-G using varying carbon concentrations. Figure 4.25a clearly shows that an increase in carbon content decreases the driving force for the FCC to BCC transformation. Figure 4.25b shows that an increase in carbon content increases the driving force for the FCC to cementite transformation.

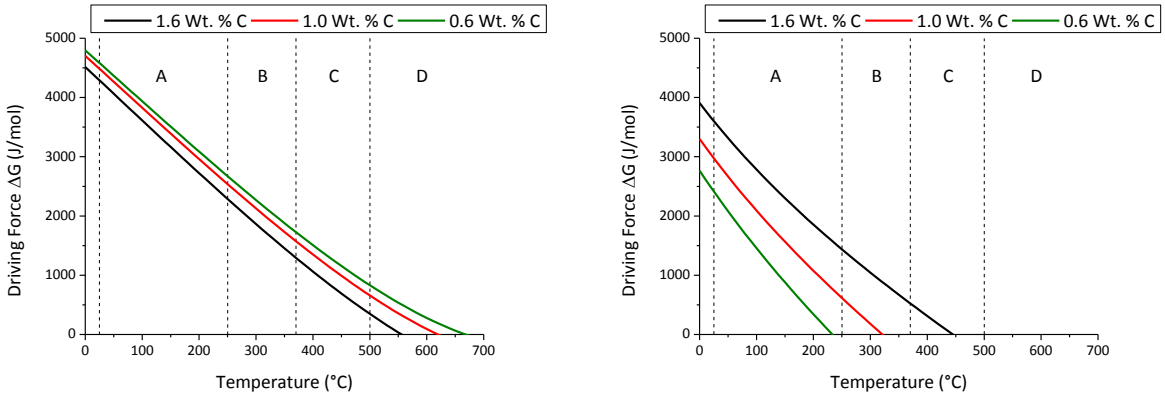

Figure 4.25: (a) Driving force for the FCC to BCC transformation under paraequilibrium conditions for QP-G with varying carbon contents in the RA. A positive driving force means that the transformation is favorable. (b) Chemical driving force for cementite precipitation under paraequilibrium conditions from austenite with varying carbon content. A positive driving force means that precipitation is favorable.

The driving forces as shown in Figure 4.25 suggest that the driving force for formation of BCC from FCC is larger than the driving force for cementite precipitation from FCC. This implies that decomposition into ferrite is favored in this temperature region.

As is observed in this work, high-carbon RA does not decompose, while low-carbon RA does decompose into ferrite in this temperature region. This suggests that a critical carbon concentration C_{bf} in RA exists allowing decomposition into bainitic ferrite. In RA grains that have a carbon concentration below C_{bf}, decomposition of RA into bainitic ferrite is thermodynamically and kinetically possible. In RA grains that have a carbon concentration above C_{bf}, decomposition of RA into bainitic ferrite is thermodynamically and kinetically less favorable. These grains will therefore not decompose into bainitic ferrite, at least not in the timescales investigated (≈1 hour). Partly, this is due to the presence of Mn, Mo and Si in QP-G. These elements slow bainite formation [66]–[69].

At longer timescales however, high-carbon RA is not expected to be completely stable. The driving force for cementite precipitation from RA grains is increased when the carbon concentration increases. In a RA grain which has a carbon concentration above C_{bf}, bainitic ferrite will not form. However, it is known that eventually cementite precipitation will take place from metastable RA at elevated temperatures [15]. This will lead to eventual decomposition of high-carbon RA.

Figure 4.26 shows a schematic extrapolation of the solubility lines of ferrite and cementite in Fe-C austenite.

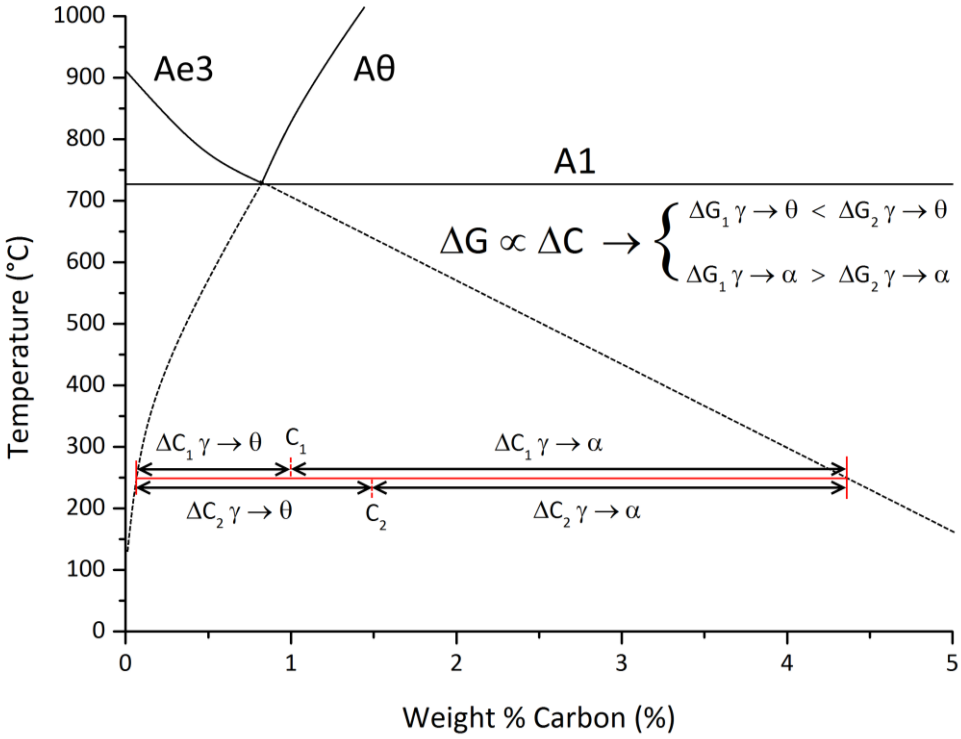

Figure 4.26: Schematic extrapolated solubility lines for ferrite and cementite in Fe-C austenite. Adapted from [70]*. The concentration of carbon in a hypothetical low carbon RA grain is denoted with C1, while the concentration of carbon in high carbon RA is denoted with C2. At equal temperatures, the difference in carbon content ΔC between the extrapolated solubility lines and C1 and C2 is proportional to the driving force for transformation as indicated.*

Region C: 370 °C – 500 °C

In this region, decomposition of RA was not observed in the timescales investigated. At these temperatures, the driving force for displacive transformations is not high enough for the RA to transform via displacive mechanisms. Furthermore, diffusion at these temperatures is limited, and no significant diffusion of iron and substitutional elements will occur. Diffusional transformation products will therefore show very low growth rates. The decomposition of RA will therefore be slow because of a combination of (too) low undercooling for displacive mechanisms and low growth rates for diffusional mechanisms.

Region D: 500 °C – 600 °C

In this region, decomposition of RA was observed. The mechanism was local precipitation of cementite, which destabilizes RA. Upon quenching from annealing in this region, martensite formation was detected.

Decomposition of RA via this mechanism is comparable to formation of pearlite from hypereutectoid austenite, and this mechanism will therefore be called the pearlitic mechanism. In pearlite formation from a hypereutectoid austenite, cementite is the leading phase. Cementite will be formed until the eutectoid composition is reached. When the eutectoid composition is reached, pearlite formation will commence.

However, due to the relatively high concentration of Mn in this alloy, pearlite formation is slowed considerably. Partitioning of Mn can control growth of cementite at these temperatures [71].

This region is expected to extend above 600 °C until an equilibrium is reached, for example in the α+γ region.

TTT diagram applicability

Based on the observed decomposition behavior, separate kinetics of decomposition exists for high-carbon and low-carbon RA. The kinetic decomposition behavior of austenite can be summarized in a Time-Temperature-Transformation (TTT) diagram. Sarikaya *et al.* [72] concluded that "… separate kinetics must be considered for the retained austenite from that of the bulk alloy", and proposed superimposed TTT diagrams containing the bulk alloy and an imaginary alloy corresponding to the RA, with an appropriate C concentration.

In the author's opinion, the results in this work validate a TTT-like diagram approach for an understanding of the decomposition behavior. In essence RA behaves as austenite which is simply higher in carbon content compared to the bulk alloy. However, the morphology of retained austenite and its microstructural environment are different compared to bulk austenite with the same carbon content. The morphology and microstructural environment of retained austenite might influence its decomposition behavior. Figure 4.27 shows a schematic TTT-like diagram drawn for QP-G, with one of the performed heat treatments indicated.

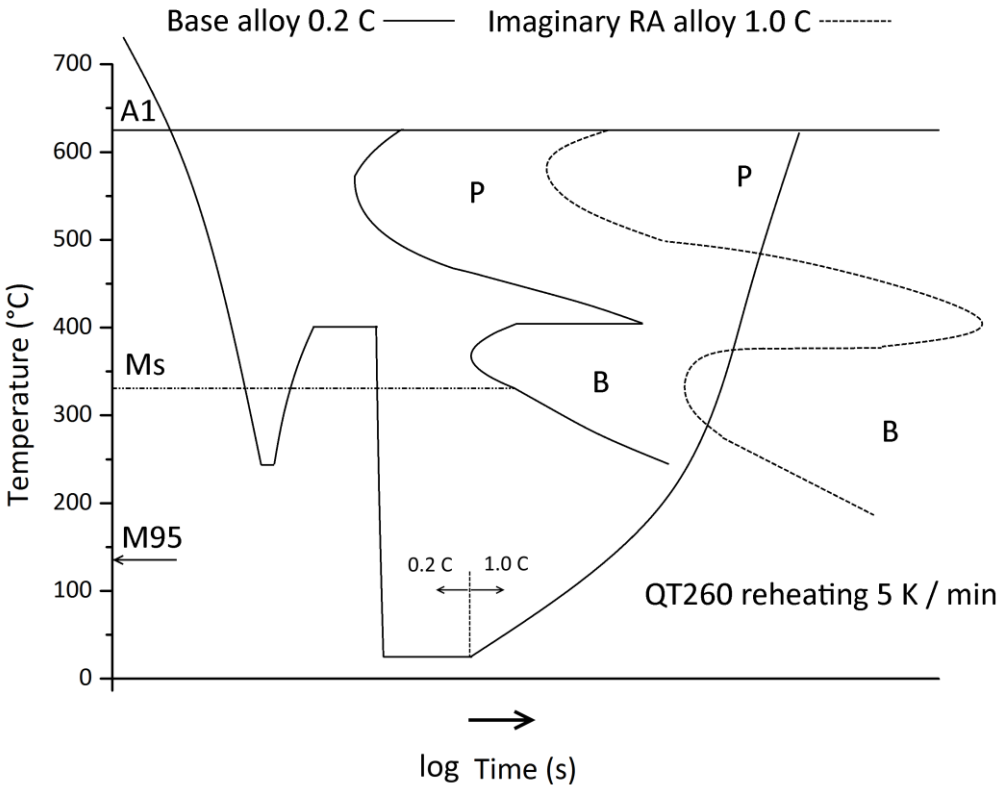

Figure 4.27: Schematical and Hypothetical TTT-like diagram of QP-G. A very schematic Q&P heat treatment with applied reheating is shown. Schematical Pearlite and Bainite start lines of the base alloy and on the imaginary RA alloy are shown. The superimposed reheating curve is shown only to give a rough indication of the behavior of decomposition, since strictly speaking it should be plotted on a continuous reheating diagrams.

Figure 4.28 summarizes the decomposition mechanisms of retained austenite.

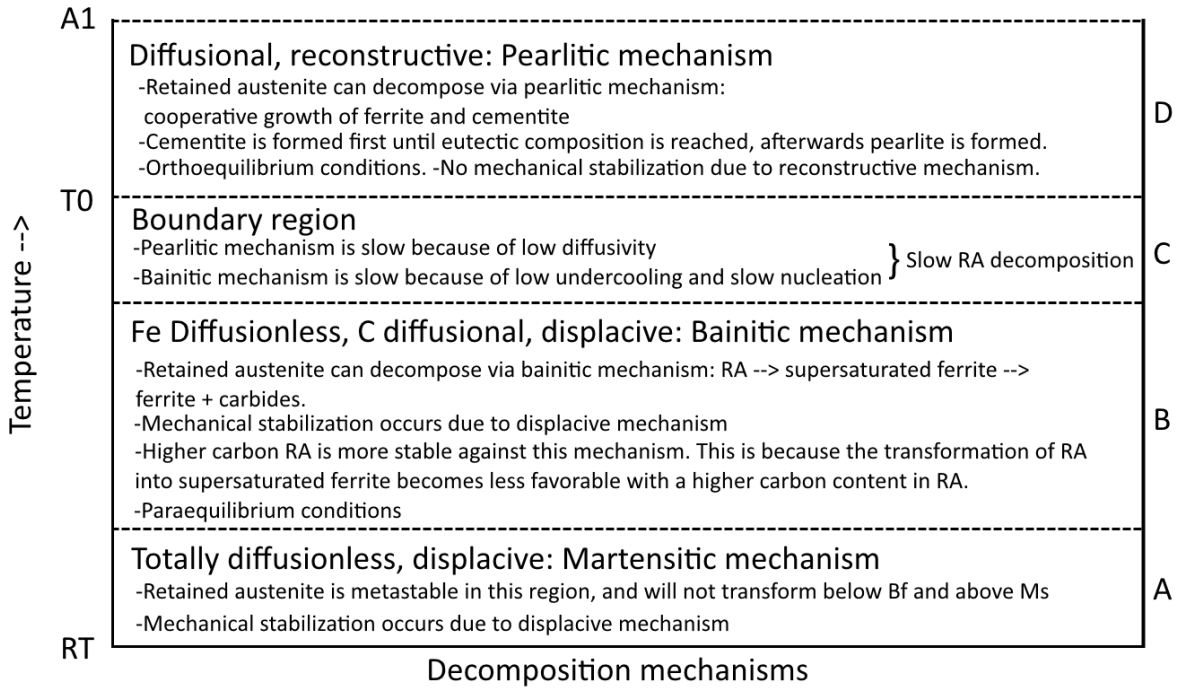

Figure 4.28: Mechanisms of RA decomposition

Chapter 5 Conclusions

5.1 Retained austenite decomposition in Quenching & Partitioning steel

In this work, the thermal stability of retained austenite has been studied in a wide range of temperatures. A coherent theory of retained austenite decomposition could be formulated. The thermal stability of retained austenite is dependent on the quenching temperature.

The results suggest that during reheating with 5 °C min^{-1}, 4 stages of retained austenite decomposition exist in the Quenching & Partitioning alloy used in this work:

A) 25 °C to 250 ° C: No decomposition of retained austenite.
B) 250 °C to 370 °C: Decomposition of retained austenite is possible, depending on carbon content in retained austenite. Low carbon retained austenite decomposes first, and is hypothesized to decompose into bainitic ferrite and carbides. After low carbon retained austenite has decomposed, no decomposition of high carbon retained austenite is observed.
C) 370 °C to 500 °C: No significant decomposition of retained austenite observed, because of (too) low undercooling for displacive decomposition mechanisms and low growth rates for diffusional decomposition mechanisms.
D) 500 °C to 600 °C: Decomposition of retained austenite. Excess carbon likely precipitates into carbides from retained austenite. The local reduction in carbon concentration destabilizes the retained austenite, which will transform into martensite upon quenching. This mechanism is similar to formation of pearlite from hypereutectoid austenite, which will form cementite until the eutectoid composition is reached. This mechanism is expected to extend above 600 °C until an equilibrium is reached in the α+ γ region.

The mechanisms of decomposition of retained austenite have been successfully mapped to a TTT diagram. Carbon-enriched retained austenite shows the same decompositions products as austenite, and in essence behaves as austenite which is higher in carbon content compared to the bulk alloy. However, the morphology of retained austenite and its microstructural environment are different compared to bulk austenite with the same carbon content. The morphology and microstructural environment of retained austenite might therefore influence its decomposition behavior. However, carbon content and distribution in retained austenite remain the main factors determining the thermal stability of retained austenite and its decomposition behavior in Quenching & Partitioning steels.

Low-carbon retained austenite is less stable than high-carbon retained austenite against decomposition into ferrite, because carbon stabilizes austenite against the ferrite transformation in in steel. Conversely, high-carbon retained austenite is less stable than low-carbon retained austenite against precipitation of cementite from retained austenite. As observed in this work, decomposition of retained austenite with carbides as the leading phase is a slower process compared to decomposition with ferrite as the leading phase. During annealing processes, high-carbon retained austenite will therefore remain stable for longer periods of time compared to low-carbon retained austenite.

Homogenization of the carbon gradient in retained austenite grains when increasing partitioning time up to 600 s gives rise to an increase in thermal stability of retained austenite grains. The absence of low-carbon austenite due to homogenization leads to net slower decomposition.

5.2 About experimental techniques

The dilatometer is a useful instrument for tracking the phase fraction of retained austenite before precipitation of carbides from martensite starts in Quenching & Partitioning steel. When precipitation starts however, length changes due to retained austenite decomposition are partially compensated by length changes due to precipitation of carbides from martensite. Furthermore, a relative decrease in the relative volume change of retained austenite decomposition occurs due to thermal expansion effects. The combination of these effects leads to limited usefulness of the dilatometer in tracking the phase fraction of retained austenite at temperatures above 400 °C during isochronal or isothermal annealing. However, the mechanisms of decomposition of retained austenite were successfully derived by analysis of dilatometry data.

Thermomagnetic methods have been successfully used to accurately determine the phase fraction of retained austenite during annealing up to 600 °C. The mechanisms of decomposition of retained austenite could not be derived by analysis of thermomagnetic data.

The combination of dilatometry and thermomagnetic methods is therefore a powerful instrument to study the behavior of retained austenite during annealing.

5.3 About Quenching & Partitioning steel

When the quenching temperature is low enough that no martensite from the second quench is formed, lattice parameters of retained austenite increase with decreasing quench temperature. This is because more carbon is available from martensite to partition into ever decreasing fractions of residual austenite.

Chapter 6 Recommendations

- The mechanical properties after annealing of Q&P steels have not been investigated. A study on the effect of the decomposition of retained austenite on these properties would be interesting. In conventional martensitic steels, temper embrittlement occurs due to the formation of very fine cementite needles due to the decomposition of film-like retained austenite. This work does not address temper embrittlement, and further study on this topic is advised.
- Film-like retained austenite has lower carbon content in Q&P steels compared to larger grains. Film-like retained austenite is more stable under stress than larger retained austenite, and responsible for the enhanced ductility at strain levels exceeding 5%. The retained austenite which decomposes first during annealing has lower carbon content according to this work. Hot-TEM studies could be performed to check whether film-like retained austenite is indeed decomposing first.
- In a heat treatment not treated in further detail in this work, QP-G samples with a QT of 160 and 260 °C were reheated with 100 °C s^{-1} to 700 °C, held there for 20 minutes and quenched. Retained austenite fractions of 0.2 for QT260 and 0.25 for QT160 were achieved. These are very high retained austenite fractions, and it would be interesting to see what the mechanical properties of these samples are.
- Heat treatments typical for welding, pre-heating for welding, galvanizing, paint baking and application of other corrosion resistant coatings should be applied on promising Q&P steels to check whether they retain their promising mechanical properties after these treatments.
- The decomposition behavior at lower temperatures and/or longer timescales has not been studied.
- DTA/DSC studies applying the same isochronal heat treatments as performed in this work should be performed. A comparison between DTA/DSC and the techniques applied in this thesis will allow a very complete picture of both retained austenite decomposition, and of the strengths and weaknesses of the respective techniques in studying retained austenite decomposition.
- Thermomagnetic methods allow accurate observations of the phase fraction of retained austenite during annealing. In the author's opinion, it is worthwhile to create a VSM allowing the application of heat treatments. Current VSM systems have limited heating rates (*e.g.* a maximum of 3 °C s^{-1}) and do not allow for quenching or rapid cooling. The ability to perform magnetic measurements during heat treatments will allow direct and accurate identification of austenite fractions below the Curie temperature.
- In the dilatometer, derivative curves (dL/dT [$\Delta L/L_0$]) allow better visual identification of metallurgical processes during isochronal reheating than purely looking at length change curves ($\Delta L/L_0$). It is therefore recommended that more use should be made of derivative dilatometry curves during isochronal heating.

Chapter 7 References

[1] S. Keeler and M. Kimchi, "AHSS Application Guidelines," 2014, WorldAutoSteel.

[2] G. F. V. Voort, Ed., *ASM Handbook volume 9, Metallography and Microstructures*. 2004.

[3] D. P. Koistinen and R. E. Marburger, "A general equation prescribing the extent of the austenite-martensite transformation in pure iron-carbon alloys and plain carbon steels," *Acta Metall.*, vol. 7, no. 1, pp. 59–60, 1959.

[4] S. Morito, X. Huang, T. Furuhara, T. Maki, and N. Hansen, "The morphology and crystallography of lath martensite in alloy steels," *Acta Mater.*, vol. 54, no. 19, pp. 5323–5331, 2006.

[5] S. van der Zwaag, L. Zhao, S. O. Kruijver, and J. Sietsma, "Thermal and Mechanical Stability of Retained Austenite in Aluminum-containing Multiphase TRIP Steels.," *ISIJ Int.*, vol. 42, no. 12, pp. 1565–1570, 2002.

[6] H. K. D. H. Bhadeshia and D. V. Edmonds, "Bainite in silicon steels: new composition–property approach Part 2," *Met. Sci.*, vol. 17, no. 9, pp. 420–425, 1983.

[7] X. C. Xiong, B. Chen, M. X. Huang, J. F. Wang, and L. Wang, "The effect of morphology on the stability of retained austenite in a quenched and partitioned steel," *Scr. Mater.*, vol. 68, no. 5, pp. 321–324, Mar. 2013.

[8] K. S. Choi, Z. Zhu, X. Sun, E. De Moor, M. D. Taylor, J. G. Speer, and D. K. Matlock, "Determination of carbon distributions in quenched and partitioned microstructures using nanoscale secondary ion mass spectroscopy," *Scr. Mater.*, vol. 104, pp. 79–82, 2015.

[9] J. G. Speer, F. C. Rizzo, D. K. Matlock, and D. V Edmonds, "The ' Quenching and Partitioning ' Process : Background and Recent Progress," vol. 8, no. 4, pp. 417–423, 2005.

[10] J. Speer, D. K. Matlock, B. C. De Cooman, and J. G. Schroth, "Carbon partitioning into austenite after martensite transformation," *Acta Mater.*, vol. 51, no. 9, pp. 2611–2622, 2003.

[11] E. De Moor, S. Lacroix, L. Samek, J. Penning, and J. Speer, "Dilatometric Study of the Quench and Partitioning Process," *3rd Int. Conf. Adv. Struct. Steels*, pp. 1–6, 2006.

[12] T. D. Bigg, D. K. Matlock, J. G. Speer, and D. V. Edmonds, "Dynamics of the Quenching and Partitioning (Q&P) Process," *Solid State Phenom.*, vol. 172–174, pp. 827–832, 2011.

[13] T. D. Bigg, D. V. Edmonds, and E. S. Eardley, "Real-time structural analysis of quenching and partitioning (Q&P) in an experimental martensitic steel," *J. Alloys Compd.*, vol. 577, no. SUPPL. 1, pp. S695–S698, 2013.

[14] F. Tariq, "Microstructural evolution during tempering of Quenched and Partitioned Medium Carbon Low Alloy Steel," presented at the Third International Conference on Aerospace Science and Engineering, Pakistan, 2013

[15] H. J. Jun, S. H. Park, S. D. Choi, and C. G. Park, “Decomposition of retained austenite during coiling process of hot rolled TRIP-aided steels,” *Mater. Sci. Eng. A*, vol. 379, no. 1–2, pp. 204–209, Aug. 2004.

[16] W. Shi, L. Li, B. De Cooman, P. Wollants, and C.-X. Yang, “Thermal stability of retained austenite in TRIP steel after different treatments,” *J. Iron Steel …*, vol. 15, no. 1, pp. 61–64, 2008.

[17] M. Amirthalingam, M. J. M. Hermans, L. Zhao, and I. M. Richardson, “Quantitative analysis of microstructural constituents in welded transformation-induced-plasticity steels,” *Metall. Mater. Trans. A Phys. Metall. Mater. Sci.*, vol. 41, no. February, pp. 431–439, 2010.

[18] N. Luzginova, L. Zhao, and J. Sietsma, “Evolution and thermal stability of retained austenite in SAE 52100 bainitic steel,” *Mater. Sci. Eng. A*, vol. 448, no. 1–2, pp. 104–110, 2007.

[19] A. Saha Podder and H. K. D. H. Bhadeshia, “Thermal stability of austenite retained in bainitic steels,” *Mater. Sci. Eng. A*, vol. 527, no. 7–8, pp. 2121–2128, 2010.

[20] J. A. Cameron, *J. Iron Steel Inst.*, vol. 194, pp. 260–267, 1956.

[21] A. S. Podder, I. Lonardelli, A. Molinari, and H. K. D. H. Bhadeshia, “Thermal stability of retained austenite in bainitic steel: an in situ study,” *Proc. R. Soc. A Math. Phys. Eng. Sci.*, vol. 467, no. 2135, pp. 3141–3156, 2011.

[22] P. V. Morra, A. J. Böttger, and E. J. Mittemeijer, “Decomposition of iron-based martensite: A kinetic analysis by means of differential scanning calorimetry and dilatometry,” *J. Therm. Anal. Calorim.*, vol. 64, no. 3, pp. 905–914, 2001.

[23] T. Waterschoot, K. Verbeken, and B. C. De Cooman, “Tempering Kinetics of the Martensitic Phase in DP Steel,” *ISIJ Int.*, vol. 46, no. 1, pp. 138–146, 2006.

[24] S. Primig and H. Leitner, “Separation of overlapping retained austenite decomposition and cementite precipitation reactions during tempering of martensitic steel by means of thermal analysis,” *Thermochim. Acta*, vol. 526, no. 1–2, pp. 111–117, Nov. 2011.

[25] E. Kozeschnik and H. K. D. H. Bhadeshia, “Influence of silicon on cementite precipitation in steels,” *Mater. Sci. Technol.*, vol. 24, no. 3, pp. 343–347, 2008.

[26] L. Cheng, C. M. Brakman, B. M. Korevaar, and E. J. Mittemeijer, “The Tempering of Iron-Carbon Martensite ; Dilatometric and Calorimetric Analysis,” *Metall. Trans. A*, vol. 19, no. 10, pp. 2415–2426, 1988.

[27] M. J. Santofimia, L. Zhao, R. Petrov, C. Kwakernaak, W. G. Sloof, and J. Sietsma, “Microstructural development during the quenching and partitioning process in a newly designed low-carbon steel,” *Acta Mater.*, vol. 59, no. 15, pp. 6059–6068, Sep. 2011.

[28] S. M. C. van Bohemen, “Bainite and martensite start temperature calculated with exponential carbon dependence,” *Mater. Sci. Technol.*, vol. 28, no. 4, pp. 487–495, Apr. 2012.

[29] T. A. Kop, “A dilatometric study of the austenite/ferrite interface mobility,” Ph.D. dissertation, Delft University of Technology, The Netherlands, 2000.

[30] S. Arajs, “Ferromagnetic Curie Temperatures of Iron Solid Solutions with Germanium, Silicon, Molybdenum, and Manganese,” *Phys. status solidi*, vol. 11, p. 121, 1965.

[31] S. M. C. van Bohemen, “The nonlinear lattice expansion of iron alloys in the range 100–1600K,” *Scr. Mater.*, vol. 69, no. 4, pp. 315–318, Aug. 2013.

[32] S. M. C. van Bohemen, “Austenite in multiphase microstructures quantified by analysis of thermal expansion,” *Scr. Mater.*, vol. 75, pp. 22–25, Mar. 2014.

[33] H. E. Kissinger, “Reaction kinetics in differential thermal analysis,” *Anal. Chem.*, vol. 29, no. 1956, pp. 1702–1706, 1957.

[34] E. J. Mittemeijer, L. Cheng, P. J. Schaaf, C. M. Brakman, and B. M. Korevaar, “Analysis of nonisothermal transformation kinetics; tempering of iron-carbon and iron-nitrogen martensites,” *Metall. Trans. A*, vol. 19, no. 4, pp. 925–932, 1988.

[35] E. De Moor, C. Föjer, J. Penning, A. J. Clarke, and J. G. Speer, “Calorimetric study of carbon partitioning from martensite into austenite steel,” *Phys. Rev. B - Condens. Matter Mater. Phys.*, vol. 82, pp. 1–5, 2010.

[36] E. J. Mittemeijer, A. Van Gent, and P. J. Van Der Schaaf, “Analysis of Transformation Kinetics by Nonisothermal Dilatometry,” *Metall. Trans. A*, vol. 17A, no. August, pp. 1441–1445, 1986.

[37] B. Rivolta and R. Gerosa, “On the non-isothermal precipitation of copper-rich phase in 17-4 PH stainless steel using dilatometric techniques,” *J. Therm. Anal. Calorim.*, vol. 102, no. 3, pp. 857–862, 2010.

[38] S. Foner, “Versatile and Sensitive Vibration-Sample Magnetometer,” *Rev. Sci. Instrum.*, vol. 30, no. 7, pp. 550–557, 1959.

[39] S. Foner, “The vibrating sample magnetometer: Experiences of a volunteer (invited),” *J. Appl. Phys.*, vol. 79, no. 8, p. 4740, 1996.

[40] “Detection setup in a VSM.” [Online]. Available: http://commons.wikimedia.org/wiki/File:VSM_en.svg. [Accessed: 12-May-2015].

[41] P. Stamenov and J. M. D. Coey, “Sample size, position, and structure effects on magnetization measurements using second-order gradiometer pickup coils,” *Rev. Sci. Instrum.*, vol. 77, no. 1, p. 015106, 2006.

[42] A. Zięba, “Image and sample geometry effects in SQUID magnetometers,” *Rev. Sci. Instrum.*, vol. 64, no. 12, p. 3357, 1993.

[43] A. Zieba and S. Foner, “Detection coil, sensitivity function, and sample geometry effects for vibrating sample magnetometers,” *Rev. Sci. Instrum.*, vol. 53, no. 9, p. 1344, 1982.

[44] D. Jiles, *Introduction to Magnetism and Magnetic Materials*, 2nd ed. Chapman & Hall/CRC, 1998.

[45] W. D. Callister, *Materials Science and Engineering: An Introduction*, 6th ed. John Wiley & Sons, 2003.

[46] L. Zhao, N. H. Van Dijk, E. Brück, J. Sietsma, and S. van der Zwaag, “Magnetic and X-ray diffraction measurements for the determination of retained austenite in TRIP steels,” vol. 313, pp. 145–152, 2001.

[47] L. Zhao, N. H. Van Dijk, A. J. E. Lefering, and J. Sietsma, “Magnetic detection of small fractions of ferromagnetic martensite within the paramagnetic austenite matrix of TWIP steel,” *J. Mater. Sci.*, vol. 48, no. 4, pp. 1474–1479, 2013.

[48] A. S. Arrott and B. Heinrich, “Application of magnetization measurements in iron to high temperature thermometry,” *J. Appl. Phys.*, vol. 52, no. 3, pp. 2113–2115, 1981.

[49] A. Bojack, L. Zhao, P. F. Morris, and J. Sietsma, “In-situ determination of austenite and martensite formation in 13Cr6Ni2Mo supermartensitic stainless steel,” *Mater. Charact.*, vol. 71, pp. 77–86, 2012.

[50] C. F. Jatczak, J. A. Larson, and S. W. Shin, “Retained Austenite and Its Measurements by X-Ray Diffraction,” Warrendale, PA, 1980.

[51] R. Delhez, “The volume fraction Austenite in a two-phase steel from XRD measurements and the standard deviation caused by the counting statistical errors.” TU Delft internal report, 2012.

[52] R. Hendrikx, “Simple improvements in the determination of Austenite content in steel, with X-ray diffraction.” TU Delft internal report, 2012.

[53] A. J. Schwartz, M. Kumar, B. L. Adams, and D. P. Field, *Electron Backscatter Diffraction in Materials Science*, 2nd ed. Springer Science + Business Media, 2009.

[54] “Electron Backscatter Pattern - FCC steel.” [Online]. Available: http://www.ebsd.com/images/articles/44/figure_4a-10kv_3nA.jpg. [Accessed: 15-Jun-2015].

[55] D. De Knijf, R. Petrov, C. Föjer, and L. a I. Kestens, “Effect of fresh martensite on the stability of retained austenite in quenching and partitioning steel,” *Mater. Sci. Eng. A*, vol. 615, pp. 107–115, 2014.

[56] M. J. Santofimia, R. H. Petrov, L. Zhao, and J. Sietsma, “Microstructural analysis of martensite constituents in quenching and partitioning steels,” *Mater. Charact.*, vol. 92, pp. 91–95, Jun. 2014.

[57] H. Kawata, K. Hayashi, N. Sugiura, N. Yoshinaga, and M. Takahashi, “Effect of Martensite in Initial Structure on Bainite Transformation,” *Mater. Sci. Forum*, vol. 638–642, pp. 3307–3312, 2010.

[58] D. De Knijf, E. P. Da Silva, C. Föjer, and R. Petrov, “Study of heat treatment parameters and kinetics of quenching and partitioning cycles,” *Mater. Sci. Technol.*, vol. 31, no. 7, pp. 817–828, 2015.

[59] M. G. Mecozzi, J. Eiken, M. J. Santofimia, and J. Sietsma, “Phase field modelling of microstructural evolution during the quenching and partitioning treatment in low-alloy steels.” To be submitted.

[60] W. Pitsch, “Der Orientierungszusammenhang zwischen Zementit und Ferrit im Perlit,” *Acta Metall.*, vol. 10, no. 1, pp. 79–80, 1962.

[61] K. Verbeken, L. Barbé, and D. Raabe, “Evaluation of the Crystallographic Orientation Relationships between FCC and BCC Phases in TRIP Steels,” *ISIJ Int.*, vol. 49, no. 10, pp. 1601–1609, 2009.

[62] W. Owen, “The Effect of Silicon on the Kinetics of Tempering,” *Trans. Am. Soc. Met.*, vol. 46, pp. 812–829, 1954.

[63] G. Thomas, “Retained austenite and tempered martensite embrittlement,” *Metall. Trans. A*, vol. 9, no. March, 1978.

[64] R. Honeycombe and H. K. D. H. Bhadeshia, *Steels: Microstructure and properties*. Butterworth-Heinemann, 2006.

[65] H. Bhadeshia, *Bainite in steels*, 2nd ed. Institute of Materials, 2001.

[66] F. G. Caballero, H. K. D. H. Bhadeshia, K. J. a. Mawella, D. G. Jones, and P. Brown, “Design of novel high strength bainitic steels: Part 1,” *Mater. Sci. Technol.*, vol. 17, no. 5, pp. 512–516, 2001.

[67] F. G. Caballero, H. K. D. H. Bhadeshia, K. J. a. Mawella, D. G. Jones, and P. Brown, “Design of novel high strength bainitic steels: Part 2,” *Mater. Sci. Technol.*, vol. 17, no. 5, pp. 517–522, 2001.

[68] M. J. Santofimia, F. G. Caballero, C. Capdevila, C. García-Mateo, and C. G. De Andrés, “New Model for the Overall Transformation Kinetics of Bainite. Part 1: the Model,” *Mater. Trans.*, vol. 47, no. 10, pp. 2465–2472, 2006.

[69] D. Quidort and Y. J. M. Brechet, “Isothermal growth kinetics of bainite in 0.5% C steels,” *Acta Mater.*, vol. 49, no. 20, pp. 4161–4170, 2001.

[70] A. Stormvinter, “Low Temperature Austenite Decomposition in Carbon Steels,” Ph.D. dissertation, KTH Royal Institute of Technology, Sweden, 2012.

[71] R. T. Van Tol, “Microstructural evolution in deformed austenitic TWinning Induced Plasticity steels,” Ph.D. dissertation, Delft University of Technology, The Netherlands, 2014.

[72] M. Sarikaya, A. K. Jhingan, and G. Thomas, “Retained Austenite and Tempered Martensite Embrittlement in Medium Carbon Steels,” vol. 14, no. June, 1983.

[73] P. J. Jacques, S. Allain, O. Bouaziz, A. De, A.-F. Gourgues, B. M. Hance, Y. Houbaert, J. Huang, A. Iza-Mendia, S. E. Kruger, M. Radu, L. Samek, J. Speer, L. Zhao, and S. van der Zwaag, “On measurement of retained austenite in multiphase TRIP steels — results of blind round robin test involving six different techniques,” *Mater. Sci. Technol.*, vol. 25, no. 5, pp. 567–574, May 2009.

Appendices

Appendix A Comparison between retained austenite fractions as determined by VSM and XRD

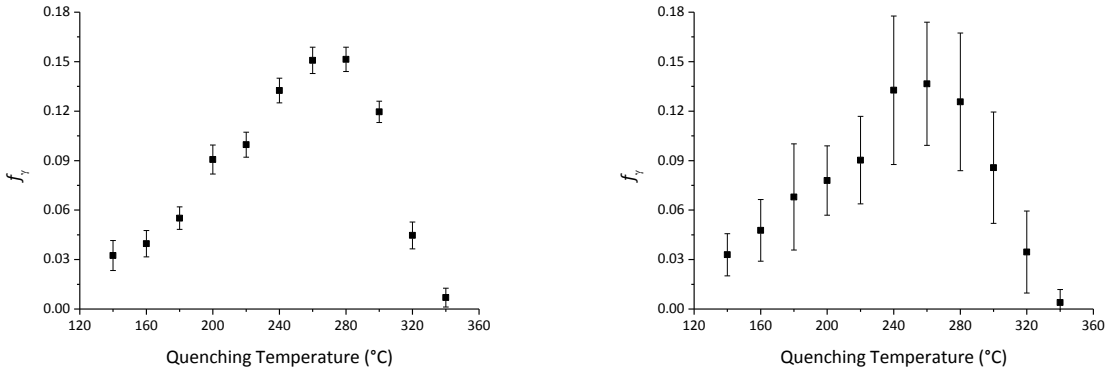

Figure A-1: Retained austenite fractions of the Q&P specimens as determined by different methods. (a) VSM. (b) XRD.

Figure A-1 shows the retained austenite fractions of Q&P specimens as determined by different methods. Figure A-1b shows that the standard deviation of the retained austenite fraction is significantly higher when obtained by XRD compared to magnetic methods in Figure A-1a. However, the absolute fractions do not differ significantly when comparing both fractions.

Since these methods measure the same quantity, it is possible to average the fractions obtained by the different methods. The averaging was performed by a weighted average f_a of the fraction of retained austenite, with the weight being the standard deviation:

$$f_a = \frac{f_1/\sigma_1^2 + f_2/\sigma_2^2}{1/\sigma_1^2 + 1/\sigma_2^2}$$

$$\sigma_a = \sqrt{\frac{1}{\left(1/\sigma_1^2 + 1/\sigma_2^2\right)}}$$

where f_1 and f_2 are the retained austenite fractions as measured by the different techniques, σ_1 and σ_2 the respective standard deviations of the measurements, and σ_a the standard deviation of the average. The net result is that the fraction and standard deviation are slightly more accurately measured, as shown for example in Figure 4.1.

However, this method does not take into account any systematic errors between the XRD and VSM measurements known to exist [73]. Since the differences is measured fraction are small however, this averaging was judged allowed for specimens that were measured both in the VSM and XRD.

Appendix B Stress relief during annealing in a dilatometer

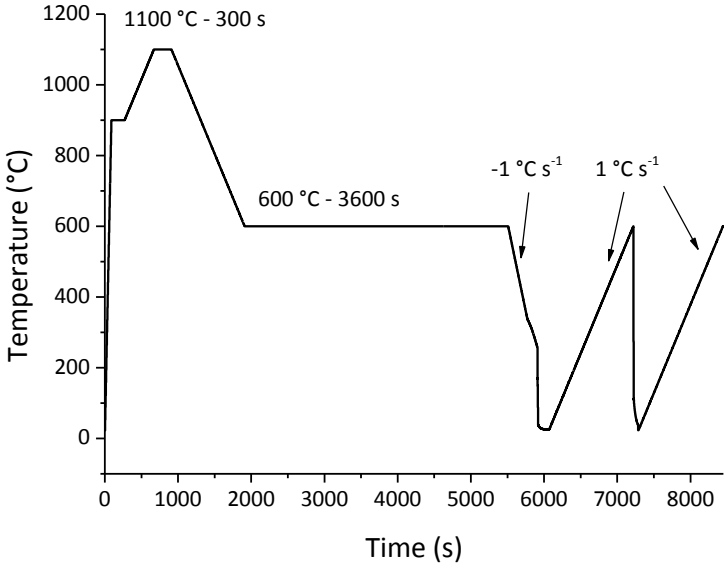

Figure B-1: Heat treatment applied to determine thermal expansion coefficients.

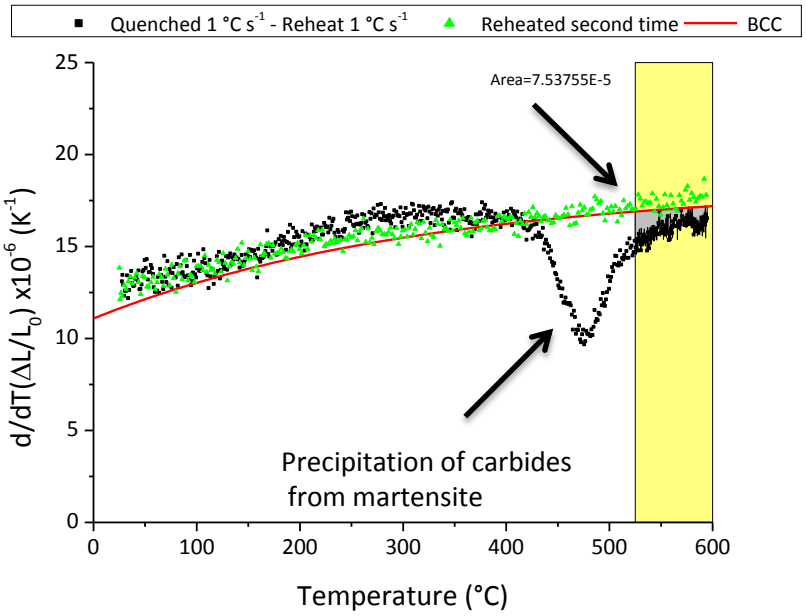

Figure B-2: The thermal expansion of the sample from Figure B-1 during reheating to 600 °C two consecutive times. The theoretical expansion of BCC iron is plotted as well. Only 1 out of every 5 data points is shown for the two reheatings, for visual clarity of the fit.

In an attempt to measure the thermal expansion behavior of QP-G, the heat treatment in Figure B-1 was applied. However, eventually the resulting data was used to investigate the difference in thermal expansion behavior of quenched specimens in this work and the expected theoretical expansion behavior.

The goal of the heat treatment in Figure B-1 was to measure the thermal expansion behavior of austenite above 900 °C, to let the formed austenite decompose at 600 °C, and thereafter measure the expansion behavior of ferrite. No decomposition was detected at 600 °C however, and

martensite was formed during the cooling to RT. After in-situ analysis of the generated data, the sample which was still in place was then reheated multiple times in an attempt to measure the thermal expansion behavior of ferrite/martensite.

Figure B-2 shows the thermal expansion of this specimen during reheating to 600 °C with 1 °C s^{-1}. Furthermore, the calculated thermal expansion (see §3.2.3) of pure BCC iron is plotted. During the first reheating, the thermal expansion deviates significantly from the ideal thermal expansion. Some retained austenite decomposition is observed around 300 °C. The negative peak around 450 °C indicates precipitation of carbides from martensite is occurring. This precipitation stops around 525 °C in other quenched samples in this work, but the thermal expansion above 525 °C still deviates significantly from the calculated thermal expansion indicating further metallurgical processes are occurring. In the second reheating however, the calculated thermal expansion and the experimental thermal expansion are nearly identical, indicating no further metallurgical processes are occurring.

The metallurgical processes occurring during the first reheating above 525 °C could be precipitation of alloy carbides and stress relief, or a combination of both. Precipitation of alloy carbides is certainly possible in QP-G, since Mn and Mo are present. However, the long soak at 600 °C would have conceivably formed alloy carbides. This would decrease the likelihood of alloy carbide formation during subsequent reheating. Therefore, it is hypothesized that stress relief is the main factor causing the "missing" thermal expansion.

Based on personal conversations with Jilt Sietsma and Peter van Liempt, temperatures above 500 °C are certainly high enough for dislocation movement and therefore stress relief. Some retained austenite decomposition is occurring, decreasing the "missing" thermal expansion. The "missing" thermal expansion is about 7.5 x 10^{-5} as numerically calculated with Origin and indicated in Figure B-2. The Young's modulus of iron between 525 and 600 °C is around 160 GPa. Using Hooke's law, the stress relief due to annealing in these particular specimens is $\sigma = E\epsilon = 160 \times 10^9 \times 7.5 \times 10^{-5} \approx 12\ \mathrm{MPa}$. While the sample theoretically should be in complete equilibrium with regards to stress, in the author's opinion, this is an approximation of reality. A low stress on the order of 10 MPa could conceivably have arisen due to martensite formation and the resulting defect and imperfections in the material.